ABSTRACT

Title of dissertation: Many-Body Dephasing in a Trapped Ion Quantum Simulator with a Cryogenic Apparatus

Harvey B. Kaplan
Doctor of Philosophy, 2019

Dissertation directed by: Professor Christopher Monroe
Joint Quantum Institute,
University of Maryland Department of Physics and
National Institute of Standards and Technology

While realizing a fully functional quantum computer presents a long term technical goal, in the present, there are small to mid-sized quantum simulators (up to $\sim$ 100 qubits), that are capable of approaching specialized problems. The quantum simulator discussed here uses trapped ions to act as qubits and is housed in a cryogenically cooled vacuum chamber in order to reduce the background pressure, thereby increasing ion chain length and life-time. The details of performance and characterization of this cryogenic apparatus are discussed, and this system is used to study many-body dephasing in a finite-sized quantum spin system.

How a closed quantum many-body system relaxes and dephases as a function of time is important to understand when dealing with many-body spin systems. In this work, the first experimental observation of persistent temporal fluctuations after a quantum quench is presented with a tunable long-range interacting transverse-field Ising Hamiltonian. The fluctu-

ations in the average magnetization of a finite-size system of spin-1/2 particles are measured presenting a direct measurement of relaxation dynamics in a non-integrable system. This experiment is in the regime where the properties of the system are closely related to the integrable Hamiltonian with global coupling. The system size is varied in order to investigate the dependence on finite-size scaling, and the system size scaling exponent extracted from the measured fluctuations is consistent with theoretical prediction.

Many-Body Dephasing in a Cryogenic Trapped Ion Quantum Simulator

by

Harvey B. Kaplan

Dissertation submitted to the Faculty of the Graduate School of the
University of Maryland, College Park in partial fulfillment
of the requirements for the degree of
Doctor of Philosophy
2019

Advisory Committee:
Professor Christopher Monroe, Chair/Advisor
Professor James Williams
Professor Norbert Linke
Professor Trey Porto
Professor Christopher Jarzynski (Dean's Representative)

Dedication

To my parents

Acknowledgments

During my undergraduate physics career as a physics major at Purdue university, I decided that I wanted to continue my study of physics with the experimental exploration of quantum mechanics in graduate school. I received an attractive offer to the University of Maryland and ultimately accepted. I contacted Chris Monroe and asked if I could work on his experiment of simulation of quantum magnetism. He said yes, and I started in the summer before my first semester. Over the years, Chris has been kind and understanding and I appreciate the opportunity to work under him in one of his world-class ion trapping labs. Now at the end of the PhD program and looking at the opportunities available, I see the high value of a PhD in physics. When I started graduate school, though not my main experiment, I started working on the quantum simulation (QSim) experiment because the experiment I mainly worked on was not yet established. The students and researchers in that lab welcomed me and were very patient to answer my questions. There, I worked with Brian Neyenhuis, Phil Richerme, Crystal Senko, Aaron Lee, and Jake Smith. At this point, I had not worked in an AMO lab before and they helped me climb up the learning curve. Some months after I started, Paul Hess joined the group and under his guidance, work started on the Cryo QSim lab. We started off based in "sketchy lab" in the CSS (Atlantic) building, and eventually moved into the new lab space in the PSC building. Paul proved to be a good teacher and was interested in the totality of the individual. Though it can be difficult to build a lab from scratch and persevere through the slow progress, I recognize the value in this experience and see it as an asset. It took two years for us to trap our first ion, another year to perform coherent entangling operations, and another year before experiments got started. In the last three years of my PhD, I worked with Wen Lin Tan, Arinjoy De, Eric Birckelbaw, Micah Hernandez, Daniel McVicker, Abhishek Menon, Albert Chu, Antonis Kyprianidis, Patrick Becker, Kate Collins, Jessie Hankes, Jiehang Zhang, Lei Feng, and Guido Pagano.

I feel very fortunate to have parents who raised me to have a mindset for success. They never pushed me, and taught me to look at matters in a holistic way. They taught me that failing does not make the individual a failure, how to be realistic with using resources, and most importantly, that being smart or accomplished is worn best when lined with humility.

When I came to Maryland, friends of my family, Debby and Ray took care of me. I consider them to be my "biggest fans" and I have enjoyed a relationship with them throughout my time at Maryland.

I came to UMD with professional aspirations and academic interest, but while here, I received so much more than I ever could have imagined at the outset. I found a community of people who exemplify humility and radiate kindness; a community of people I now call my own. In no particular order, I list the following individuals and families who have been friends and examples to me.

I am thankful for and in great debt to: Rabbi Teitelbaum, Rabbi Backman who jumped into hard situations with me to help me out, Rabbi Goldstein who showed me the same love he shows his children, Ezra Mond for learning Torah with me as if I were a brother, Rabbi Blate who saw in me things I did not see in myself, Rabbi Schwartz who showed me what it looks like to be humble, modest, and to be an eved Hashem, Dr. Zach Epstein, Josh Cahn, Seth Rabinovitz, Herschel Wohl, Mrs. Spolter, Shimon Deutsch, Dr. Ari Mizel

for being a great example and helping me to make some important career related decisions, Cortell family, Manes family, Shininger family, Friedman family, Mittelman family, Mervis family, Keller family and particularly Jacob for learning with me, Mond family, Eizenstat family, Deutsch family, Azran family, Chinn family, Koretzky family, Rabbi Kreiser, Wolf family, Strum family, Traub family, Werner family, Rabbi Frank, Rabbi Reingold, Rav Aaron Lopiansky, Rabbi Sigler, Mrs. Shames, Mrs. Goodman, Lemberg family, Zenwirth family, (Rav) Matt and Shelly LeVee, Yehuda Ratafia, Zvi Speigel, Lowenbraun family, Rabbi Hauer and family, Rabbi Gelbtuch, Rabbi Rosenbaum

I hope that the aforementioned people know that the little things they have done for me have not gone unnoticed and have influenced me in an immensely positive way.

Contents

List of Figures

Part I

Introduction

The pursuit of quantum information can be considered to have the following long-term and short-term goals. The long range goal involves making a fault tolerant quantum computer that can reliably perform quantum algorithms that are out of the reach of classical computers. These machines require many qubits (maybe upward of 1,000,000) and single and multiple qubit operations with high fidelity. In the short term, there are efforts to move toward using smaller scale quantum devices to perform a small aspect of an algorithm which will be interfaced with a classical computer. A classical computer can run a classical outer loop optimization algorithm, for instance, or be interfaced in another way with a quantum processor. Here, a small-intermediate scale quantum simulator acts as a stand alone quantum device; though it could be interfaced with a classical computer. The quantum simulator here allows for the simulation of continuous time evolution of a number of Hamiltonians based on the long range interaction of spin systems. One can simulate many-body interacting quantum systems with control over many of the system parameters.

The Monroe-lab quantum simulation effort started in $\sim$2009 with a room temperature experiment that is still active today. In this thesis, this original experiment will be referred to as the warm experiment. This experiment started out with doing experiments on a few ions and demonstrated the basics of spin frustration (73) in both ferromagnetic and antiferromagnetic systems. Now, the warm system routinely performs experiments with many ions. The biggest asset for this experiment is the capability to perform individual ion/spin addressing. Without

this feature, all operations are performed globally, that is, on all the ions uniformly. This feature allows the warm experiment to prepare the spin chain in an arbitrary product state, and allows for individual control of spins during the course of an experiment.

The warm experiment is in a room temperature vacuum chamber. The lifetime of the ion chain is determined by the probability for background gas particles to destructively collide with the ion chain. In the warm experiment, a chain of 30 ions will last for about 5 minutes. As the complexity of experiments grows, it is desirable to conduct experiments with a greater number of ions and to hold them for a longer period of time. The effort to improve this experiment is where the second version of this experiment steps in. This second version of the Monroe quantum simulation experiment employs a cryogenic vacuum chamber to reduce the pressure in the vacuum chamber and will therefore be referred to as the cryo experiment. The cryogenic feature allows for experiments to be performed on longer ion chains that stay trapped and crystallized for a longer duration than its warm counterpart. Using the cryo experimental apparatus, a number of experiments were performed, including: QAOA (quantum approximate optimization algorithm), confinement of low energy quasi-particles, and the many-body dephasing experiment which is described here. This thesis is the culmination of the process of setting up a lab starting from an empty room, and bringing the experimental apparatus to the point of taking data for a quantum simulation experiment.

Part II

Trapology and realizing spin spin interactions

1 Linear Paul trap

The ideal Paul trap is described by the potential

$$V(y,z,t) = \frac{V_0}{2}\left(1 + \frac{y^2 - z^2}{R^2}\right)\cos(\Omega t) \tag{1}$$

where R is the distance from the axis of the trap to the nearest electrode surface (assuming a symmetrical trap geometry), and V_0 is the amplitude of the AC voltage drive (15) (16) (17). This requires electrodes with a hyperbolic profile that are infinitely long along the $\hat{x}$ axis; the axis of the trap. To create this potential, two of the electrodes that are diagonal from each other are connected to ground and the other pair are driven with an oscillating potential $V_0\cos(\omega_{rf}t)$ at the RF frequency, ω_{rf}. Since the goal is to create a confining potential in the center of the trap, static potentials alone are insufficient. Rather the oscillating potential is needed to create a time-averaged potential which will trap the ions (28).

In order to make a practical ion trap, the length is defined and static voltage end-caps are used to confine the trapped ions axially (along $\hat{x}$). Additionally, the shape of the blades are changed from the ideal hyperbola shape to, in this case, thin blades. Changing the shape of the blades allows for more optical/laser access to the ions but distorts the trapping potential.

Just considering the end-caps held at potential U_0 (15), the potential at the site of the

trapped ions is

$$U(x,y,z) = \frac{\kappa U_0}{X_0^2}\left[x^2 - \frac{1}{2}\left(y^2+z^2\right)\right]. \tag{2}$$

where κ is a geometrical factor, U_0 is the static potential of the endcaps, and X_0 is the length from the center to the end of the trapping rods.

Putting both of these potentials together, the resultant electric field (at the ions) is

$$E(x,y,z,t) = -V_0\left(\frac{y\hat{y}-z\hat{z}}{R^2}\right)\cos\left(\omega_{rf}t\right) - \frac{\kappa U_0}{X_0^2}\left[2x\hat{x}-y\hat{y}-z\hat{z}\right]. \tag{3}$$

When considering a trapped particle with mass m and charge Q, the equation of motion is described by the Mathieu equation as follows,

$$\ddot{u_i} + [a_i + 2q_i\cos\omega_{rf}t]u_i = 0, \tag{4}$$

where $a_y = a_z = \frac{-1}{2}a_x = \frac{-4Q\kappa U_0}{mX_0^2\omega_{rf}^2}$ and $q_y = -q_z = \frac{2QV_0}{mR^2\omega_{rf}^2}$, $q_x = 0$, and $u = u_z\hat{x} + u_y\hat{y} + u_z\hat{z}$,

In the limit of small $|a_i|$ and small $|q_i|$, the first order solutions to the equations of motion are

$$u_i(t) \approx u_{1i}\cos\left(\omega_{sec}t + \phi_{Si}\right)\left[1 + \frac{q_i}{2}\cos\omega_{rf}t\right], \tag{5}$$

where $\omega_{sec} \approx \frac{\omega_{rf}}{2}\sqrt{a_i + \frac{1}{2}q_i^2}$ is the secular frequency, and $q \sim 0.35$ in the transverse trapping directions $(\hat{y},\hat{z})$[1]. The slower frequency, ω_i is the secular motion of the ion in the effective, time-averaged, trapping potential, and the other frequency, ω_{rf}, is the RF drive frequency. Equation 5 shows that the RF drive directly influences the ion's motion and is called micromotion.

[1]This value of q corresponds to the full value of the RF voltage.

The micromotion that an ion experiences is influenced by the construction of the trap and by the position of the ion in the trap (15) (29) (30), and will be explained in more depth later in this thesis. When considering the RF effective harmonic potential, if the ion chain sits along the RF null, then classically, there should be no micromotion. Due to stray electric fields, the ions may not be at this null. The trap blades can be biased to shift the ion chain to the RF null. While at the RF null, the ion will still experience micromotion. The effective trap is a harmonic potential, so the trapped ion, even in the motional ground state, will have a wavefuntion that extends out from the RF null. Therefore, the ion will always have micromotion sidebands that can be measured.

2 Loading ions into the trap

$^{171}Yb^{+}$ ions are loaded into the ion trap in the following way. An oven consisting of a small metal tube with an enriched Yb foil[2] inside is held in vacuum with its opening facing the ion trap (more oven details are later in the thesis). The oven is heated up and neutral ^{171}Yb atoms exit the opening and travel across the vacuum. Some of the ^{171}Yb atoms travel across the trapping region between the trap blades. At this point, ionization lasers are focused at the trapping region in order to ionize the neutral ^{171}Yb atoms through a two-photon ionization process. A 399nm laser beam promotes the ^{171}Yb atoms from the S to the P state, and a 355nm pulsed laser is used to excite from the P state to the continuum. The 355 laser is mainly used for coherent state manipulation, but works well for this application. The 369nm cooling laser can also be used for the second ionization step.

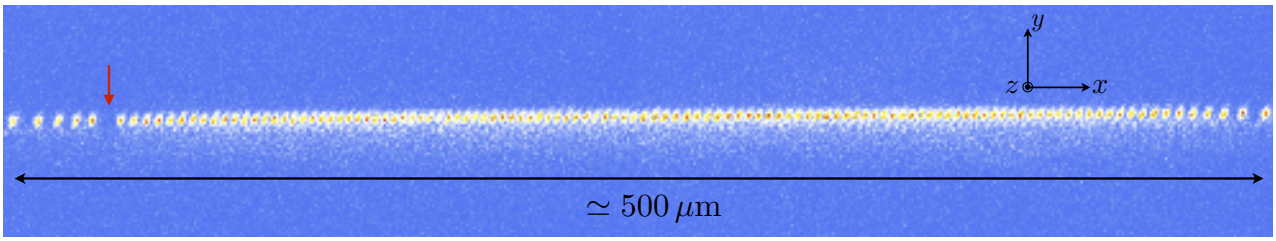

Figure 1: **121 ion chain**: 121 ion chain was trapped and held for hours. The red arrow points to the site of a dark Yb ion. This could be a different isotope that was loaded, YbH, or an ion in the F state.

As explained in the introduction, this apparatus is designed to perform quantum simulation experiments with longer chains than the warm apparatus. The longest chain trapped was a 121 ion chain, Fig. 1, which was trapped and remained crystallized for hours [3]. The red arrow points to the site of a dark Yb ion. This could be a different isotope that was loaded, YbH

[2]The Yb sample is enriched so the sample consists mostly of ^{171}Yb atoms.
[3]Lets round the chain lifetime up to infinity!

that was formed upon collision with a H_2 molecule from the vacuum (42), or the ion could have undergone a collision from an excited state and ended up in the D state which has a lifetime of ~ 10 years. During the lifetime of this 121 ion chain, the dark ion did not reorder with the other ions, which indicates that the chain was relatively stable. So far, experiments have been performed with up to 41 ions, but the 121 ion chain provides encouragement to perform experiments with longer chains.

3 Laser cooling the trapped ions

Once trapped, the ions are initially cooled by means of Doppler cooling, which is discussed in detail in many sources, (18) (31). Doppler cooling requires a cycling transition. For $^{171}Yb^{+}$, two cycling transitions are used (Fig. 2), the transition between the $^{2}S_{1/2}$ F=0 state with the $^{2}P_{1/2}$ F=1 states, and the transition between the $^{2}S_{1/2}$ F=1 states and the $^{2}P_{1/2}$ F=0 state. These cycling transitions are driven with 369nm light that is red detuned from resonance by 10 MHz to 20 MHz. These transitions are not completely closed, as 0.05% of spontaneous decays will leave the ion in the $^{2}D_{3/2}$ manifold of states. Doppler cooling will typically leave the ions with around 2-5 phonons of motion. Further cooling is performed with side-band cooling which will be discussed later. The Doppler cooling light must have all polarization components (σ^{+}, σ^{-}, π) in roughly equal proportion in order to properly work.

The $^{2}D_{3/2}$ state is re-pumped back to the cycling transitions using 935nm light. The 935 light stimulates the electron in the $^{2}D_{3/2}$ state to the $^{3}[3/2]_{1/2}$ state which then spontaneously decays to the $^{2}S_{1/2}$ manifold of states. It is important that the polarization of the 935nm light is stable. This light is sent through a polarization maintaining fiber and the output passes through a $\lambda/2$ waveplate before falling incident on the ions. The polarization is experimentally adjusted so that it effectively repumps the atoms out of the $^{2}D_{3/2}$ state. If the polarization is not properly aligned, there can be problems with measuring full detection contrast.

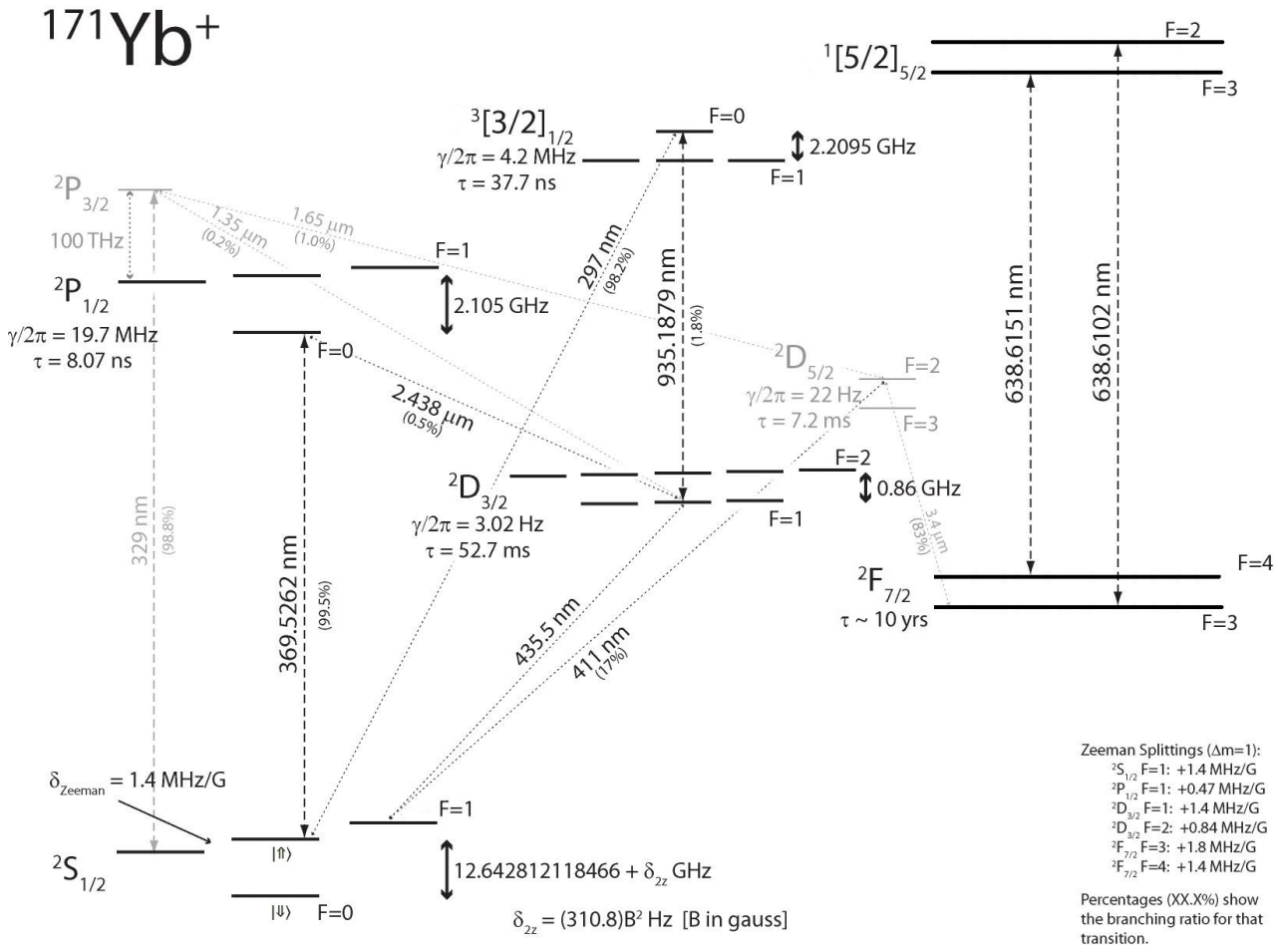

Figure 2: **^{171}Yb$^+$ energy level diagram**: The ^{171}Yb$^+$ ions are cooled on the ^{2}S$_{1/2}$ to ^{2}P$_{1/2}$ transition and a 935nm repump laser pumps population out of the ^{2}D$_{3/2}$ state.

4 State preparation and detection

4.1 Optical pumping

Once the ions are cooled, the all down state, $|\downarrow\downarrow ... \downarrow\rangle_z$ is prepared using optical pumping. Figure 3 shows that 369nm light resonant with the $^2S_{1/2}$ F=1 to $^2P_{1/2}$ F=1 transition is excited. Once in the $^2P_{1/2}$ F=1 manifold, the ion can spontaneously decay to any of the $^2S_{1/2}$ states. Once in the $|\downarrow\rangle = {}^2P_{1/2}$, F=0 state, the ion is ~ 10 GHz off resonant from the nearest transition. The total decay probability of the ion from the $^2P_{1/2}$ F=1 state to $|\downarrow\rangle$ is 1/3 (18). The optical pumping beam must have all polarization components as shown in the energy diagram.

4.2 State detection

Preparing the ion/spin chain in $|\downarrow\downarrow ... \downarrow\rangle_z$ is the first step in any experiment. Next, the experiment is conducted and finally measured. The measurement operator is $\hat{\sigma}_z$, making the possible outcomes the $|\uparrow\rangle_z$ or $|\downarrow\rangle_z$ states for each ion.

The state of the ion is measured by shining 369nm light onto the ion chain that is resonant with the $^2S_{1/2}$ F=1 to $^2P_{1/2}$ F=0 transition, Fig. 4. This is termed detection light. Only the $|\uparrow\rangle_z$ state is resonant with the detection light. The ion can spontaneously decay to any of the $^2S_{1/2}$ F=1 levels. Since many absorption/emission events are desired, the beam contains all polarization components so that the detection process can continue until enough photons are collected for ion/spin state detection (detection light is usually on for 1 ms and corresponds to $\sim 20,000$ absorption/emission cycles). The ion fluoresces isotropically from the detection

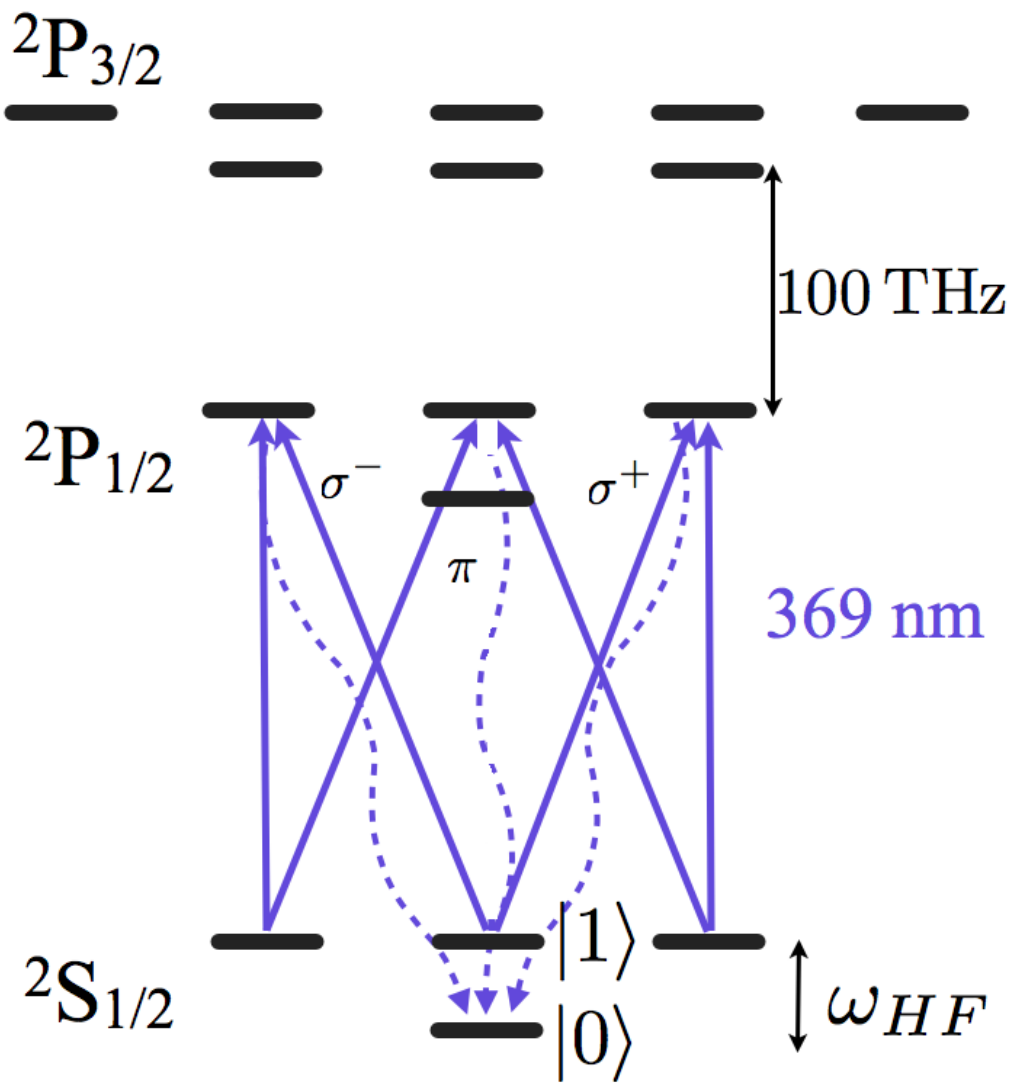

Figure 3: **Optical pumping scheme**: All polarization components (σ^+, σ^-, π) are needed as the electron can start from and decay to any of the $^2S_{1/2}$ states.

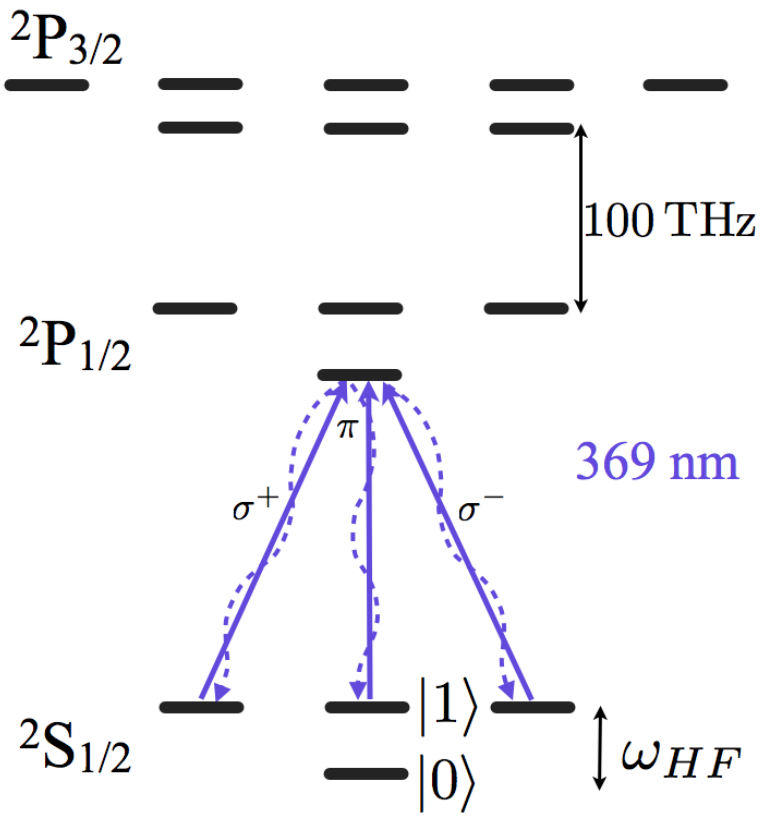

Figure 4: **Detection scheme**: The detection light is not resonant with the $|\downarrow\rangle$ state but is resonant with the $|\uparrow\rangle$ state. All polarization components are needed as shown.

light and a fraction of that light is collected by imaging optics and focused onto an ICCD camera for spin-state readout, as explained later. With a small probability, the detection light can off-resonantly excite either spin state to the $^2P_{1/2}$ F=1 manifold where the ion can then decay into the other spin state and produce detection errors (4).

Each of the processes of Doppler cooling, optical pumping, and detection, involve spontaneous decay to the $^2S_{1/2}$ F=1 manifold of states. Therefore, if the Zeeman states are degenerate, the ion can be pumped into a dark state through the process of coherent population trapping (22) (41). Therefore, a B-field is applied to the ions to break this degeneracy and prevent coherent population trapping. The B-field at the site of the ions is $\sim$ 2.9 G and the

Zeeman line separation is ~ 4.0 MHz from the $|\uparrow\rangle$ state.

5 Collective ion chain vibration

5.1 Motional sidebands

With a single ion in an ion trap, Raman spectroscopy of the motional sidebands will yield three motional sidebands on the red and blue side of the spectrum[4]. Each peak is from each of the principle axes of ion motion in the trap. There are two transverse modes and one axial mode, that is, transverse or radial to the axis of the chain. The convention for this experiment is that the transverse mode farthest from the carrier is the $\hat{y}$ direction and the other transverse mode is along the $\hat{z}$ direction. The axial trap direction is defined as $\hat{x}$.

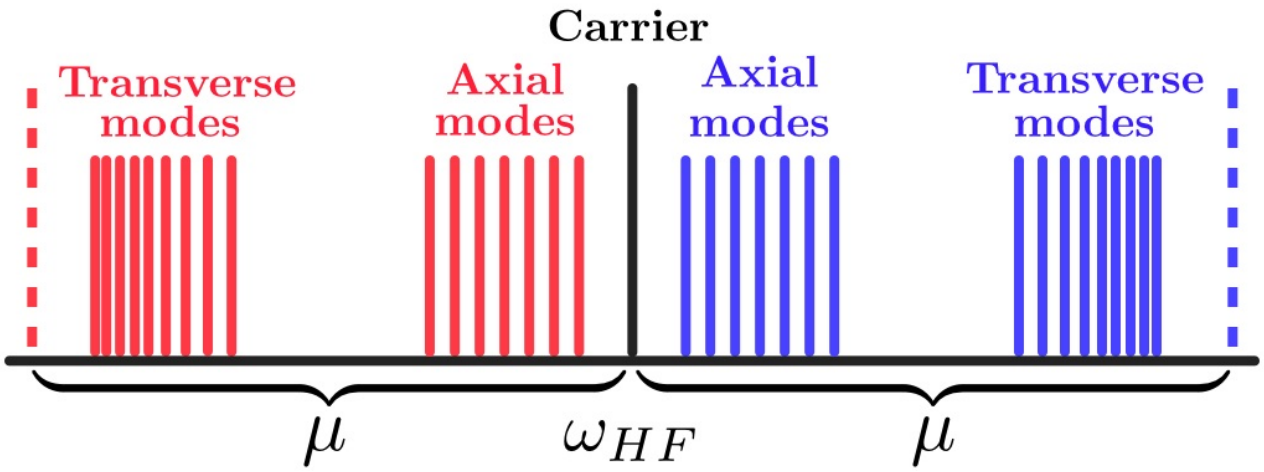

Figure 5: **One set of transverse motional modes**: Cartoon depiction of one set of transverse collective motional modes. The transverse and axial modes are depicted. The dashed red and blue lines represent the location of Raman beat-notes when performing the Molmer-Sorensen scheme to create entanglement (explained later).

With a chain of N ions, each principle axis has N vibrational modes. Figure 5 shows a cartoon depiction of the corresponding motional modes from a chain of ions. Only one set of transverse modes are shown. The center-of-mass (CM) transverse mode is farthest from

[4]the motional sidebands are resolved when in the Lamb-Dicke regime to be explained later.

the carrier. The axial modes organize more similarly to a classical masses-coupled -by-springs system with the CM mode closest to the carrier. The transverse modes are used to create the spin-spin interactions and will be the subject of the rest of the discussion when collective motional modes are mentioned.

5.2 Coupling to transverse vibrational modes

The ion trap blades can be biased in order to 'twist' the principle trap axes. Therefore, the trap axes are twisted so that both sets of transverse modes are driven by the Raman beams (to be explained later) (5). In other experiments [5], only one set of transverse modes are driven. This is done by making the transverse trapping frequencies degenerate so that the transverse axis is defined by the axis of the Raman laser beams. In this experiment, the ion chain is not stable in such a trapping configuration, so the transverse modes are kept non-degenerate.

As more ions are added to the chain, the CM mode stays at the same frequency (same distance from the carrier), but the other modes become closer to the carrier. If the highest-order transverse mode touches the carrier frequency (the vibrational mode is at zero frequency) then the chain is at the threshold of going into the zig-zag configuration (Fig. 55).

Intuitively, one can think about this by considering the fixed potential of the ion trap and adding in more and more ions. At some point, the trapping potential will not be able to hold the ions in a linear chain and they will become zig-zag.

[5] In the Monroe labs

5.3 Higher order sidebands

Here is an interesting experimental study that was performed with one ion. Sidebands were measured on the blue side of the carrier at a frequency around twice that of the trap frequency (9MHz), and four peaks were measured for a given frequency scan. This is shown in Figure 6. The frequency range was scanned for different twist values[6], where each color represents a different twist setting. Though the peak heights are not symmetrical, the peak locations are (excluding peak A). The interpretation of this is that the B peaks are from two $\hat{z}$ transverse modes being excited, the C peaks are from one $\hat{y}$ and one $\hat{z}$ mode being excited together, and the D peaks are from two $\hat{z}$ modes being excited simultaneously. The C peaks are well overlapped on each other which indicates that changing the twist shifts the $\hat{y}$ and $\hat{z}$ modes symmetrically in either direction. The A feature is yet unknown, but is in the same place for different twist values, so that should help to determine what it is.

5.4 Sideband cooling

After a chain of ions is cooled with Doppler cooling, Raman sideband cooling is used to further reduce the number of phonons per vibrational mode. With one ion, the transverse modes of motion have been measured to have 0.022(18) phonons along the $\hat{y}$ directions and 0.080(45) phonons along the $\hat{y}$ direction after sideband cooling. Sideband cooling is aptly discussed in other references (10) so will be treated in a basic way here. In principle, with a chain of N ions, N sideband cooling frequencies are needed, one for each mode. With two sets of transverse modes, $2N$ frequencies are needed. Only the transverse modes need to be sideband cooled

[6]By biasing the trap blades, the transverse principle trap axes can get 'twisted' or rotated. When twisted, the relative strength of the $\hat{y}$ and $\hat{z}$ transverse trapping frequencies changes.

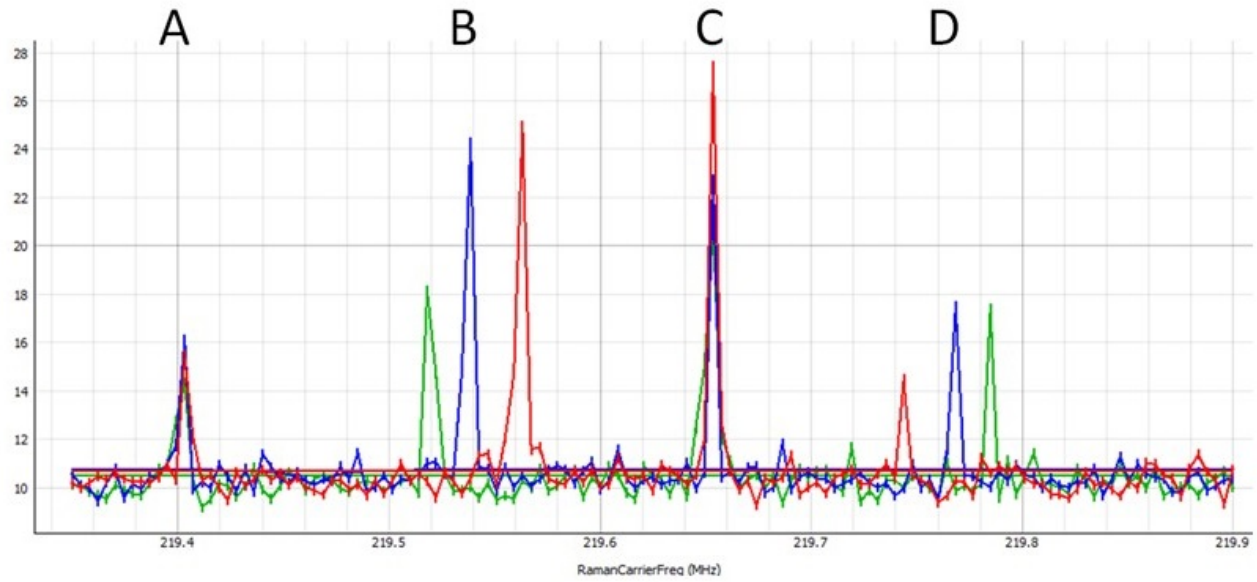

Figure 6: **2^{nd} order sidebands**: With one ion, the frequency range centered at twice the trap frequency, $\sim$ 9MHz, was scanned for different twist values. The peaks B, C, and D are double excitations of transverse motional sidebands. The $\hat{x}$ axis is in units of MHz.

since the axial modes do not participate in the spin-spin interactions. Instead of cooling each mode, only the modes that are the most prone to heating up with phonons are cooled such as the CM modes and those nearby. This is explained in more detail in the calibration section of this thesis.

6 Coherent spin manipulation

The next section will walk through the coherent operations that are performed on the ions using the Raman beams. Since this topic has been covered thoroughly in many places, highlights and important results will be related here (32) (16). The result of the Raman scheme is that the two Yb hyperfine levels, namely the $|^2S_{1/2}, F = 0, m_F = 0\rangle$ state and the $|^2P_{1/2}, F = 1, m_F = 0\rangle$ state become an effective 2-level (spin1/2) system. The details of the Raman process are discussed in the appendix.

6.1 Spin and phonon interactions with laser fields

The overall Hamiltonian can be separated into three parts

$$\hat{H} = \hat{H}^m + \hat{H}^e + \hat{H}^I, \tag{6}$$

Where $\hat{H}^m$ considers the collective motion of the ion chain, $\hat{H}^e$ considers the effective two electronic states, and $\hat{H}^I$ characterizes the interaction between the applied laser fields and the motional and electronic degrees of freedom. The motional Hamiltonian is given by

$$\hat{H}^m = \frac{\hat{p}^2}{2m} + \frac{m}{2}\left(\frac{\omega_{rf}}{4}[a_y + 2q_y \cos(\omega_{rf} t)]\right)\hat{y}^2, \tag{7}$$

the effective 2-level electronic Hamiltonian is given by

$$\hat{H}^e = \frac{\omega_{hf}}{2}\sigma_z, \tag{8}$$

and the interaction Hamiltonian is given by

$$\hat{H}^I = \frac{\Omega}{2}[\sigma_- + \sigma_+] \times [e^{\mathrm{i}(\vec{k}\hat{x}-\omega t+\phi)} + e^{-\mathrm{i}(\vec{k}\hat{x}-\omega t+\phi)}], \tag{9}$$

where m is the mass of a single $^{171}\mathrm{Yb}^+$ ion, ω_{rf} is the RF trap drive, ω_{hf} is the hyperfine splitting, $\vec{k}$ is the difference $\vec{k}_1 - \vec{k}_2$ of the counter-propagating Raman beams, and ω is the Raman beam frequency difference $\omega_1 - \omega_2$, and $\hbar = 1$. This discussion will focus on coupling only to the $\hat{y}$ direction of transverse modes.

Using $\hat{H}_0 = \hat{H}^m + \hat{H}^e$, $\hat{H}^I$ can be transformed into the interaction picture of

$$\hat{H}^I_{int} = \hat{U}_0^\dagger \hat{H}^I \hat{U}_0, \tag{10}$$

where $\hat{U}_0 = exp\left[-\mathrm{i}\hat{H}_0 t\right]$.

In the interaction picture, the rotating wave approximation can be performed which states that the terms containing the expressions $e^{+/-\mathrm{i}(\omega+\omega_{hf})t}$ can be neglected. Physically, this can be interpreted as having terms that are acting on a time-scale that is much shorter than the measurement time scale. Thus, only the average effect of those terms are realized and the term can be neglected.

Using the relations of $\hat{x} = \sqrt{\frac{1}{2m\nu}}\left(\hat{a}u^*(t) + \hat{a}^\dagger u(t)\right)$ and the Lamb-Dicke parameter $\eta = kx_0$ where $x_0 = \sqrt{1/(2m\nu)}$ and ν is the trap frequency, the Hamiltonian can be transformed into

$$\hat{H}_{int} = \frac{\Omega}{2}\hat{\sigma}_+ e^{\mathrm{i}\left[\phi+\eta\left(\hat{a}u^*(t)+\hat{a}^\dagger u(t)\right)-\delta t\right]} + h.c., \tag{11}$$

where $\delta = \omega - \omega_{hf}$. Since $u(t) \approx e^{\mathrm{i}\nu t}$ for small q, equation 11 can be written at

$$\hat{H}_{int} = \frac{\Omega}{2}\hat{\sigma}_+ e^{\mathrm{i}\left[\phi+\eta\left(\hat{a}e^{-\mathrm{i}\nu t}+\hat{a}^\dagger e^{\mathrm{i}\nu t}\right)-\delta t\right]} + h.c.. \tag{12}$$

6.2 Lamb-Dicke regime

These experiments are in the Lamb-Dicke regime which means that $\eta \ll 1$. Physically, this means that the spatial extent of the ground state vibrational (motional) wavefunction is much smaller than the wavelength of the counterpropagating Raman beams. In terms of manipulating the ion chain, it means that an increase or decrease of only one phonon of energy can accompany an electronic transition.

When in the Lab-Dicke regime, the Hamiltonian (Eq.12) can be expanded in η to yield

$$\hat{H}_{int} = \frac{\Omega_0}{2}\hat{\sigma}_+ \left[1 + \mathrm{i}\eta\left(\hat{a}e^{-\mathrm{i}\nu t} + \hat{a}^\dagger e^{\mathrm{i}\nu t}\right)\right] e^{\mathrm{i}(\phi-\delta t)} + h.c., \tag{13}$$

where $\Omega_0 = \Omega/(1+q_x/2)$, m is the mass of one $^{171}\mathrm{Yb}^+$ ion, and ν is the secular trap frequency. As mentioned before, $\delta = \omega - \omega_{hf}$, so when the frequency $\omega = 0$, the carrier is stimulated and when $\omega = +/-\nu$ the blue/red motional sideband is stimulated. In short, in Eq. 13, the terms that have time dependence are neglected. These values make sense for the typical parameters this our experiment. Typical values might be $\Omega/2 = 400$ kHz and $\nu = 4.5$ MHz. In this case, where one is measuring Rabi flopping on the carrier or on a sideband at $\Omega/2$ or at $\eta\Omega/2$ (which is on the order of 500 Hz), the ν frequency will be averaged out.

6.3 The Molmer-Sorenson scheme and the Ising Hamiltonian

The Molmer-Sorenson (MS) scheme is used to create spin-spin interactions among the simulated spins in the quantum simulator. The MS scheme is conducted by illuminating the ion chain with a Raman beat-note tone that is detuned red of the red motional sidebands, while simultaneously applying a tone that is detuned blue of the blue sidebands. When the red and blue beat-note tones are detuned far enough away from the motional sidebands, the effective Hamiltonian only has a spin-spin coupling and negligable coupling to motion. This far-detuned MS regime is the quantum simulation regime used and will be outlined below.

The derivation of the MS scheme has been documented thoroughly in past papers and theses. The quick treatment here will follow the derivation from the Islam thesis (10). Here, all of the vibrational modes will be treated. When the red and blue detuned sidebands are applied to the ion chain, the Hamiltonian becomes

$$\hat{H}_{eff} = \hat{H}_{red} + \hat{H}_{blue} \tag{14}$$

$$= \sum_{i=1}^{N}\sum_{m=1}^{N} \frac{\eta_{i,m}\Omega_i}{2}\left[a_m e^{\mathrm{i}\delta_m t}e^{\mathrm{i}\phi_M} + a_m^\dagger e^{-\mathrm{i}\delta_m t}e^{-\mathrm{i}\phi_M}\right]\sigma_{\phi_s}^i \tag{15}$$

$$= -\mathrm{i}\sum_{i=1}^{N}\sum_{m=1}^{N} \frac{\eta_{i,m}\Omega_i}{2}\left[a_m e^{\mathrm{i}\delta_m t} - a_m^\dagger e^{-\mathrm{i}\delta_m t}\right]\sigma_x^i \tag{16}$$

where the phase $\phi_M = (\phi_b - \phi_r)/2$ and $\phi_s = \pi/2 + (\phi_b + \phi_r)/2$, $\sigma_{\phi_s}^i = \cos(\phi_s)\sigma_x^i + \sin(\phi_s)\sigma_y^i$, and where ϕ_r and ϕ_b are the phases on the individual red and blue sidebands from Eq. 13. The indices i and m count over the ions in the chain and the collective motional modes respectively. The last expression results when $\phi_r = 0$ and $\phi_b = \pi$, which makes $\phi_M = \pi/2$, $\phi_s = \pi$, and

$\sigma^i_{\phi_s} = \sigma^i_x$. To clarify, these directions refer to the Bloch sphere and not to the physical lab coordinates.

The time evolution of $\hat{H}_{eff}$ is taken and the Magnus Expansion (3) is used to deal with the fact that $\hat{H}_{eff}$ is time dependant. The resulting Hamiltonian is an effective Ising Hamiltonian

$$\hat{H}_{Ising} = J_{i,j}\sigma^i_x\sigma^i_x \tag{17}$$

where

$$J_{i,j} = \Omega_i\Omega_j R\sum_m \frac{b_{i,m}b_{j,m}}{\mu^2 - \omega_m^2}. \tag{18}$$

In this expression, $\eta_{i,m} = \sqrt{\frac{k}{2m\omega_m}}b_{i,m}$, where $b_{i,m}$ is the eigenvector for the i^{th} ion participating in the m^{th} normal mode of motion. $R = \frac{k^2}{2m}$[7] is the recoil frequency and μ is the frequency of the detuned sideband. This result is in the limit of large detuning, specifically where the detuning $\mu - \omega_{CM} \geq 3\eta\Omega$.

Though the native spin-spin interaction is antiferromagnetic (AFM), a ferromagnetic (FM) interaction can be simulated by changing the sign of the transverse B-field as explained in the supplemental material in reference (35). In this experiment the sign convention of the Hamiltonian results with FM interactions for +B and AFM interactions for -B.

6.4 Microwave rotations

Just like Raman rotations, microwaves can be used to perform single spin rotations. Microwaves on resonance with the hyperfine splitting can directly drive spin rotations between

[7]This expression is normally multiplied by $\hbar$, but in this case $\hbar = 1$.

$|\uparrow\rangle_z$ and $|\downarrow\rangle_z$. The transition is insensitive to magnetic fields to first order and the second order sensitivity to magnetic fields is $\delta \sim 310.8$ Hz/B^2 in Gauss (18).

Unlike Raman rotations, the microwave can not be used to drive a sideband of motion (using the methods in this experiment). When comparing the Lamb-Dicke parameter ($\eta = kx_0$) between the Raman beams ($\lambda = 355$nm) and the resonant microwaves ($\lambda = 0.0238$m), $\eta_{microwave}$ is about 5 orders of magnitude smaller than that for the Raman beams. Therefore, η for the microwaves is so small that no motion can be driven.

6.5 The dark F state

When an ion chain is trapped, occasionally, some of the ions in the chain will become dark. When this happens, they will not fluoresce under cooling light, but will hold their spot in the ion chain. There are two possibilities for what is causing this. The first is that the $^{171}Yb^+$ ion can react with a H_2 molecule and create YbH (42). The other option is for a Yb ion to make a transition to the F state which has a lifetime of ~ 10 years. The ion will transition to this state through a collision, likely with H_2, from the D state. The ion can get repumped out from the F state with 638nm light. As shown in Figure 2, there are two 638nm lines that can be applied (a laser can be swept across these resonances) to pump out of the F state. The ion decays back to the D state and is repumped with 935nm light back to the S level. Alternatively, the high power 355 pulsed laser can "blast" the ions out of the F state. Though it is uncertain as to exactly which energy level this process uses. It works very well in terms of how quickly it takes to get the ions back fluorescing. The above two mechanisms are for when an ion that was initially bright becomes dark.

Part III

Cryogenic ion trap design, fabrication, and operation

7 Cryogenic vacuum

As with most ion trapping and AMO experiments, these experiments are performed under vacuum, usually UHV and below. Typically, vacuum is achieved by initially pumping with a scroll/turbo pump to a pressure between 10^{-6} to 10^{-8} Torr, and then an ion pump is used to decrease and to maintain a low vacuum pressure $\sim 10^{-11}$ Torr. In this experiment, the cryopump is turned on once a pressure of $\sim 10^{-6}$ Torr is reached. Then the cold surfaces serve to pump and maintain a lower vacuum pressure at $\sim 10^{-12}$ Torr. The pressure in the vacuum is determined by the amount of background gas particles that persist in the vacuum.

At room temperature, these background gas particles can include water that was adhered to the inner surfaces of the vacuum chamber and hydrocarbons that out-gas from materials in the vacuum. At cryogenic temperatures, all gasses are frozen to the cryogenic surfaces except for H_2 and He. Figure 7 (33) shows the saturation of various gasses as a function of temperature.

Using the cryostat, lower pressures can be achieved and maintained than a room temperature apparatus. This puts the experiment in the regime where typical vacuum pressure

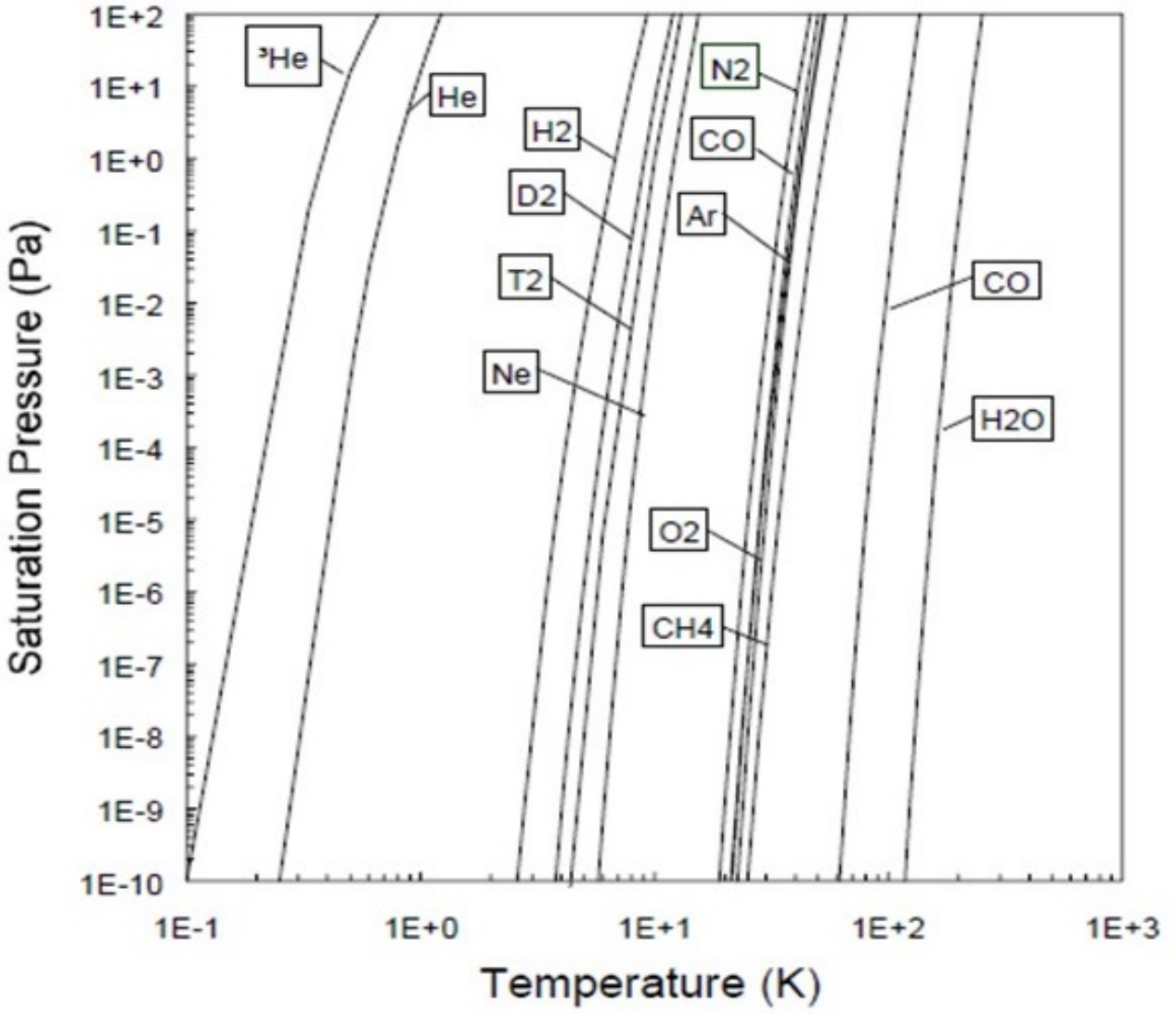

Figure 7: **Saturation pressure as a function of temperature:** Here, the saturation pressure of gasses in vacuum are plotted at cryogenic temperatures.

gauges can not read. The radiation shields[8] at 4K and 40K provide differential cryo-pumping, Figure 8. Practically speaking, this prevents properly measuring the pressure of the inner-most chamber where the ions reside. This necessitates a different method for measuring the pressure. Particularly, the ion chain can be used to measure the vacuum pressure. (Using the ion chain as a pressure gauge is discussed in the appendix.)

8 Cryostat apparatus

The cryogenic vacuum chamber is pictured in Fig.8. The main features are the Cold Head at the top of the cryostat and the vacuum chamber at the bottom (a). The cold-head (Sumitomo, RDK-415D2) is a two-stage Gifford-McMahon cryopump. The vacuum chamber below has a top that is highest on the sides with the center recessed about 16 inches below the height of the sides. This allows for the cold-head to protrude into the structure of the vacuum chamber. The cold-head vibrates as it is driven by a piston inside. The cold-head and the vacuum chamber are situated so they are not in direct physical contact with each other.

In order to conduct heat away from the vacuum chamber, the intervening space between the vacuum and the cold-head is filled with He gas; purple color in (a). This space is called the exchange gas region. The bottom part of this region is rated to cool down to 3.5K to 4.2K and the middle part to 25K to 45K (Sumitomo Technical manual p.5). These sections will be referred to as the 4K and 40K stages respectively. Due to operational details which will be discussed later, the coldest bottom region sits at 7.5K and the middle section sits at 52K.

The helium is contained in the exchange gas region by rubber bellows sealing off the space

[8]Described in more detail later in this thesis.

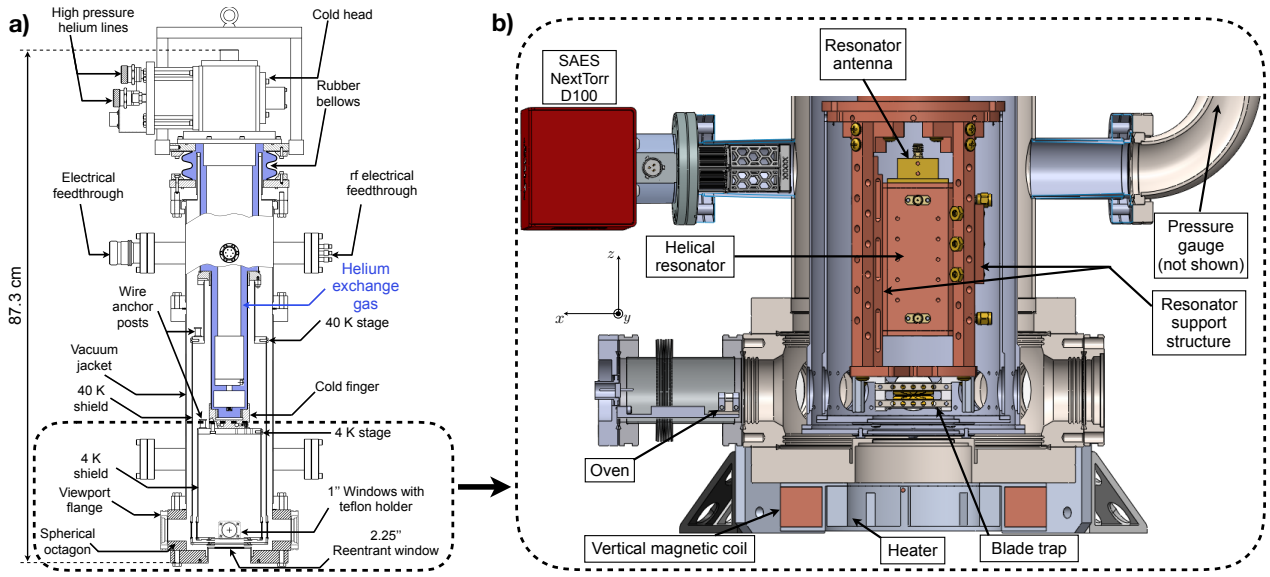

Figure 8: **Cryogenic vacuum apparatus. a)** Side view section of the cryostat (courtesy of Janis Inc). **b)** Cross section view of the lower section, 90° rotated with respect to a). The vertical magnetic coil is mounted on the bottom of the reentrant window flange. An aluminium fixture with heaters held in it is designed to rest in the coil's inner diameter in order to prevent water from condensing on the outside face of the recessed (reentrant) window, when the apparatus is cold.

between the cold-head and the vacuum chamber. To further mitigate vibration transfer, the cold-head is mounted to the cloud. The cloud refers to the equipment support structure above the optics table that is mounted to the ceiling. Inside the vacuum there are two nested radiation shields. One is in direct contact with the 4K stage and the other with the 40K stage. These radiation shields allow for differential cryo-pumping that results in the lowest pressure vacuum in the center where the ions are. The bottom portion of the vacuum chamber is a spherical octagon which allows for plenty of optical access. The nested radiation shields have the same octagon pattern of windows to enable optical access to the trapped ions. The main features inside the vacuum are the helical resonator (expounded upon in the appendix) and the ion trap. The helical resonator effectively acts as a voltage step-up transformer that takes the RF voltage from the standard SMA wires and increases the voltage to ~ 500 volts which

is the operational voltage of the RF ion trap blades.

9 Vibration isolation system and measurements

It is important to measure the timescale and the amplitude of the residual acoustic vibrations at the trap. Indeed, anticipated quantum simulation experiments can last up to 10 ms, creating spin-spin interactions (43) through stimulated two-photon Raman processes driven by a pulsed laser at $\lambda = 355$ nm. Therefore, any ion chain displacement of the order of λ during the laser interaction time would result in an unwanted phase shift experienced by the ions.

The mechanical stability of the whole apparatus is characterized by interferometric measurements. The trap was removed and three mirrors were placed on the trap mount, along the three principal axes: the Raman direction y, the trap axis x and the vertical imaging direction z (see Fig. 9). In this way, every movement of the trap region with respect to the breadboard and the table was measured with a few nanometers of resolution. Instead of counting fringes directly, three piezo-mounted mirrors were used on the reference path of the Michelson interferometers to lock the interferometer to a fringe (see Fig. 9). The PID servo loops had 1.8 kHz bandwidth and therefore could fully compensate acoustic noise over the frequency range of interest (up to 300 Hz). The voltage-to-distance conversion of the piezo-mounted mirrors was characterized on a static interferometer. This way, the output voltages applied to the piezos were a direct measurement of the displacement of the trap mount along the three principal axes of the trap. If interference fringes were measured directly, then a large displacement would be difficult to detect as the fringe contrast has a maximum value. The voltage signal driving the piezo provides a direct measurement of the displacement from vibrations.

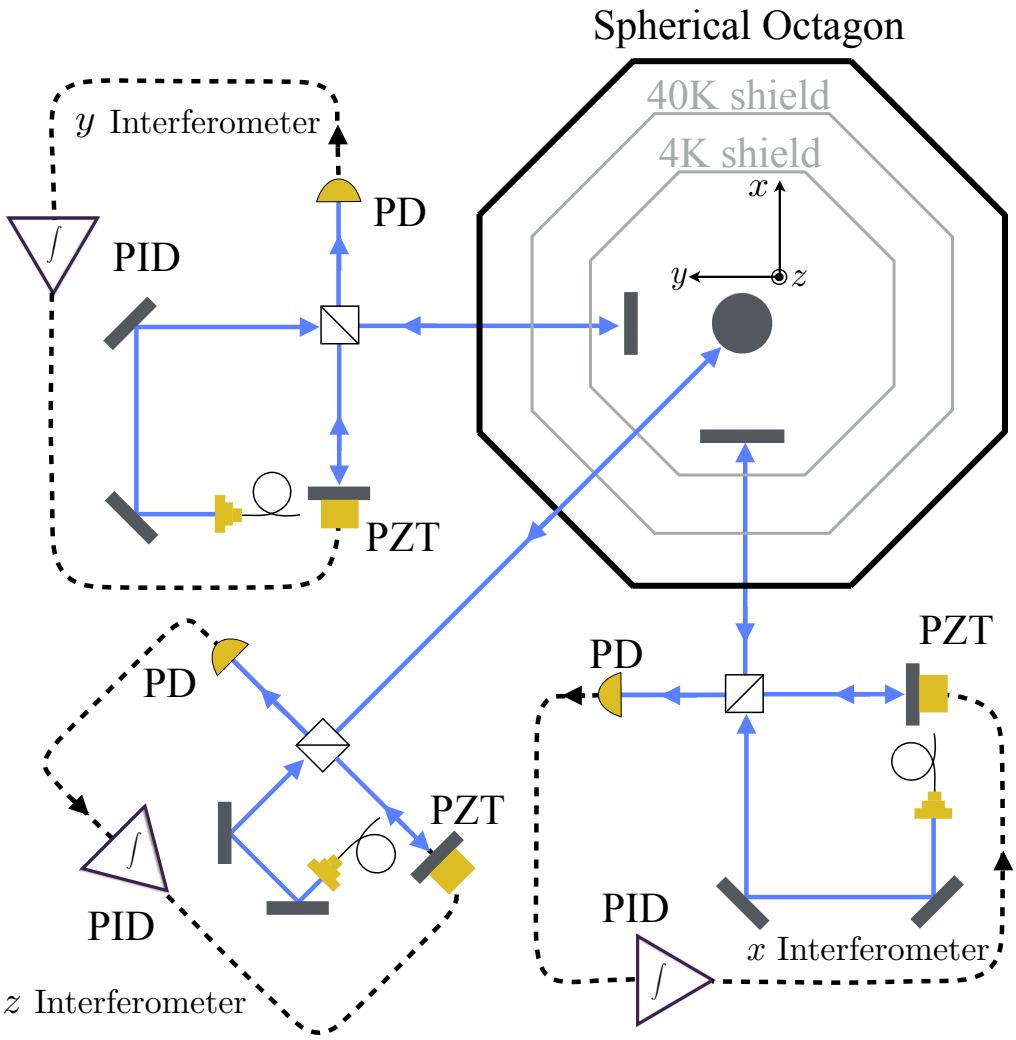

Figure 9: **Interferometric setup for vibration measurements**: Three mirrors are mounted inside the cryostat and attached to the trap mount along the three principal axes of the trap. Three different fibers deliver laser light to three interferometers with piezo-mounted mirrors (PZT) which lock the photodiode signal to a fringe with a feedback loop. The PID voltage output to the piezos compensate for vibrations and are used to monitor their amplitude and frequency.

In the x-y plane, the main contribution is given by a peak around 40 Hz, which is attributed to the normal mode of the cryostat's 60 cm long lever arm. Finite element analysis suggests that the vibration modes at higher frequencies (120 Hz and 282 Hz peaks) are to be attributed to the mechanical structure inside the 4 K shield, made up of the resonator and the trap mount.

Most of these vibrations were driven by the vibrating cold head through liquid helium condensed at the bottom of the exchange gas region at the lowest operating temperature, Fig. 8b. This condensation resulted in a reduced performance of the vibration isolation system, which can be overcome by heating up the 4 K stage and operating above the He boiling point. With the 4 K stage at $T = 7.7$ K, the rms displacements in both the x and y directions were reduced by a factor of 5, as shown in Fig. 10. The vibration modes above 100 Hz are the most problematic ones as they are on a similar timescale of a typical quantum simulation experiment. In order to eliminate these higher frequency modes, the resonator static support was strengthened, making the whole 4 K structure stiffer. By doing so, the higher frequency modes were suppressed by more than an order of magnitude (see Fig. 11). This leaves only two very well defined normal modes at 39 Hz and 45 Hz, which have also been suppressed with respect to Fig. 10b.

These lower frequency vibration modes constitute a manageable problem for a typical experiment duration as one could apply a spin-echo scheme to compensate the unwanted 40 Hz phase variation. In addition, a permanent mirror holder compatible with the trap was designed and installed in order to monitor the vibrations along the Raman y direction in real time. This was set up to compensate the unwanted phase shift via a feed-forward scheme feeding to the AOM phase or to an EOM in the Raman path.

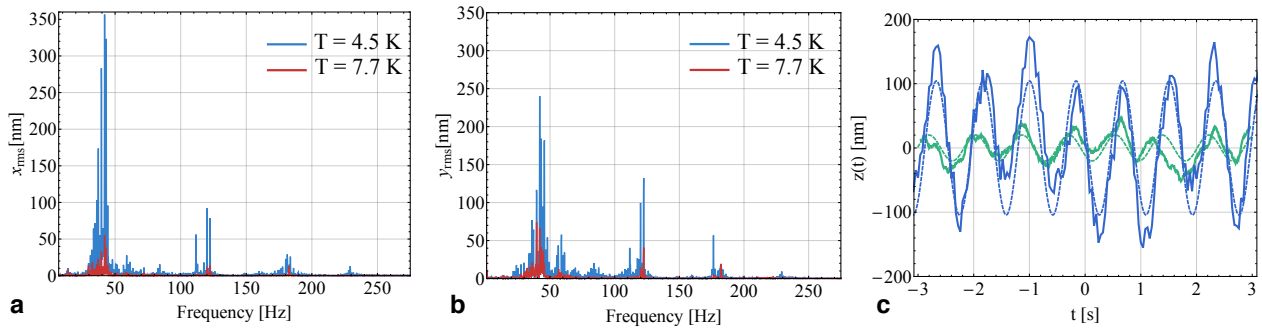

Figure 10: **Vibrations along the three trap principal axes**: a-b) In-plane x-y vibrations for trap mount temperatures $T = 4.5$ K and $T = 7.7$ K. Rms amplitudes along $x(y)$ are reduced by a factor of 5(6) respectively by raising the temperature of the cryostat above the helium boiling point. The resolution band width (RBW) is 0.1 Hz. c) Vertical vibration induced by the cryostat fitted with a sine at 1.2 Hz frequency (dashed lines). The blue (green) line refers to the vibrations before (after) improving the static support of the breadboard, yielding a 40 nm pk-pk oscillations.

The mechanical stability along the vertical z direction was investigated, and a very well defined oscillation at the cold head vibration frequency (1.2 Hz) with a peak-to-peak amplitude of 200 nm was measured, as shown in Fig. 10c. This was ascribed almost entirely to a vibrational mode of the whole breadboard on which the cryostat was supported. Indeed, the same oscillation was observed using a reference mirror attached to the underside of the breadboard, instead of the mirror attached to the trap mount inside the cryostat. In order to reduce these slow oscillations, more static support was added to the elevated breadboard and thus reduced the peak-to-peak amplitude to about 40 nm.

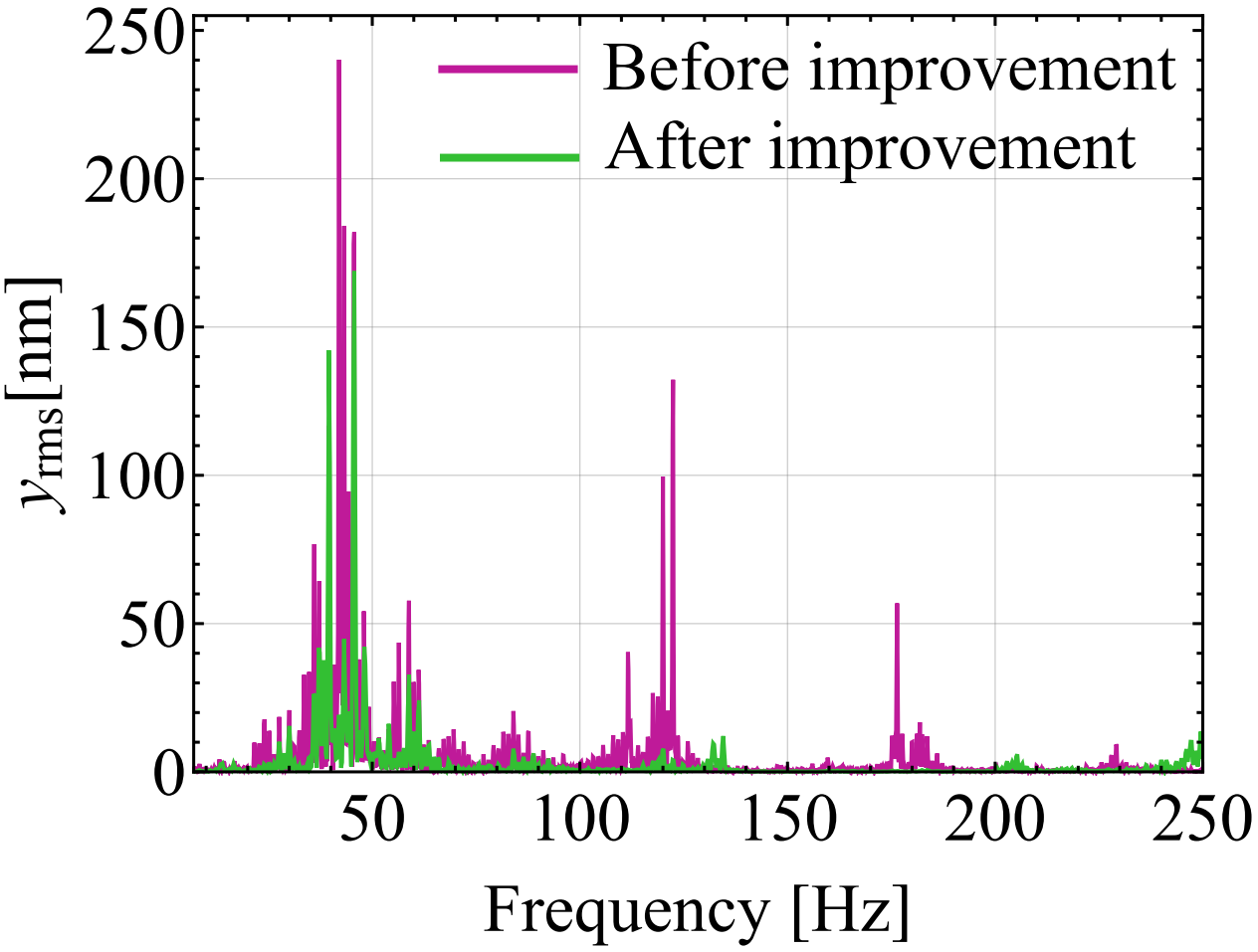

Figure 11: **Improved vibrations along the y axis**: After improving the resonator static support structure, the frequency modes above 100 Hz shown in Fig. 10b were suppressed by a factor of 10. The dominant acoustic modes remaining after the improvement were at 39 and 45 Hz. For both datasets, $T = 4.5$ K. The RBW is 0.1 Hz.

10 Cryogenic infrastructure

10.1 Cold-head infrastructure

The Gifford McMahon cold-head uses compressed He as the refrigeration medium. Connected to the cold-head, there is one high pressure and one low pressure He line. These lines are routed through a feed-through in the wall of the lab to the back service corridor. The other ends are connected to a Helium compressor (Sumitomo, F-70). The He compressor is chilled with a closed cycle of distilled water that is in turn chilled with an industrial chiller (Tek-Temp, Model: NRD550/S1/R2K). This chiller is further chilled with cold water supplied by the building[9]. The He in this closed cycle system has been under pressure since 2016 and it has not needed a He refill.

10.2 Magnetic field coils

Starting from the bottom of the cryostat, there is a magnetic field coil. This coil, as well as the other magnetic field coils, was made in-house, and provides a B-field in the $\hat{z}$ direction (vertical). Nested in this B-field coil is an aluminum ring with embedded heaters. This allows one to keep the reentrant window warm enough so that condensation does not form on the outside of this window. At the window level of the cryostat, there are three more B-field coils. Two are placed along the $\hat{y}$ direction and one is placed along the $\hat{x}$ direction. In this experiment, the counter-propagating (Raman) frequency comb beams[10] travel along the $\hat{y}$ direction and the length of the chain is along the $\hat{x}$ direction.

[9]The local lab filter that is cleaning the building water looks gross and the filter has never been changed...

[10]The pulsed 355nm laser, which provides the Raman beams, can be viewed as a frequency comb. This is explained extensively in other thesis papers and resources.

These B-field coils are placed as follows. One coil each is placed at the north and south window of the vacuum chamber[11] ($\hat{y}$ direction) which have current flowing through them in the same direction, and are wired in series so they are controlled together. One coil is at the East window[12] and the last coil is under the cryostat as mentioned above. The current in these coils is adjusted so that the net B-field is along the counter-propagating Raman beams (to be explained later).

10.3 Ion/getter pump

Further up on the cryostat is the ion/getter pump. Most vacuum systems use a roughing pump/turbo pump combination to initially pump down the vacuum and maintain low vacuum with an ion pump. In this system, one device (SAES, NEXTORR D 100-5 PUMP) works as both an ion pump and a getter pump. Most recently, when using the ion pump feature, the current it drew was on the order of 1.0 nA. Therefore, there was no need to keep this feature. With this decision, the associated magnets surrounding the device were taken off in order to decrease the stray B-field near the ions. The getter pump consists of a material that absorbs gas upon contact. At cryogenic temperatures, all gas should be frozen except for H_2, which the material of the getter is designed to absorb. At the top of the vacuum chamber section is a pressure relief valve, and electrical feed-throughs. The pressure relief valve is designed to open if the pressure inside the vacuum chamber becomes too high. This could happen if the cryostat stops working and heats up. While the cryostat is cold, one expects there to be a steady influx of gas coming into the vacuum chamber and becoming cryopumped. Upon

[11] Each of the 8 spherical octagon windows are positioned along N, NE, E... NW

[12] There is no coil across the experiment at the west window because of space constraints.

heating up, all this pumped gas will be released into the vacuum and can cause the vacuum chamber to become over pressured.

11 Cryostat wiring

11.1 RF voltage

The electrical feed-throughs on the vacuum chamber allow for RF power to reach the trap, the ion trap blades to be biased, connect to temperature probes, and to run an in-vacuum (in cryostat) heater. The RF is sourced from a signal generator (SRS DS345) at ~ 24.1564 MHz. The RF power passes through a voltage variable attenuator (VVA), then through a high power amplifier, and into the cryostat. Once in the cryostat, the power travels directly to the helical resonator without heat sinking (in contrast to the DC wiring described below)[13].

The RF power enters the resonator antenna coil and the voltage is stepped up so that the voltage amplitude is around 500V at the output of the resonator. This RF power goes directly to the RF electrodes of the ion trap. 1% of the high power RF is capacitively picked off and sent back through an SMA cable out of the cryostat. This RF signal is sent through a rectifier to give a DC voltage signal where the voltage value corresponds to the RF amplitude of the RF driving signal. The DC rectifier output is compared with a reference voltage on a PID, and is used to adjust the VVA voltage. This locking loop stabilizes the RF voltage on the RF trap blades and thereby stabilizes the transverse trapping frequencies. This is seen through the equation $\omega_{sec} \approx \frac{\omega_{rf}}{2}\sqrt{a_i + \frac{1}{2}q_i^2}$, where the secular frequency (in the transverse direction) is proportional to q_i and $|q_i| = \frac{2QV_0}{mR^2\omega_{rf}^2}$. Therefore, the transverse secular frequency is proportional to V_0, which is the amplitude of the RF voltage.

[13]Ideally, the RF power lines would be connected directly to the heat sinks as well. They are not connected because of the difficulty in connecting SMA cables to the heat sinks.

11.2 Static voltage

As there are two static potential trap blades that each have 5 sub-electrodes, it is necessary to individually bias these electrodes. The voltage source is from a set of chassis-mounted NI PXI-6713 cards. The analog output from these cards range from -10V to +10V. These outputs pass through a set of RF filters and then enter the vacuum chamber through electrical feed-throughs at the top of the cryostat. The wiring is configured so that the voltage can be amplified to range from -100V to +100V, but this has not been implemented. Thus far, all experiments have been performed with the lower voltage range and there is no need to use the higher voltage settings. The next section will discuss the in-vacuum wiring that makes the connection between the vacuum electrical feed-throughs and the trap blades.

11.3 Linear Paul trap

The ion trap used in this apparatus is a macroscopic linear RF Paul trap (34), (28). Each blade is subdivided into 5 sections, each of which can be individually biased. Figure 12 shows a RF blade with the five blade sections. Here, the top part of the blade is completely covered with gold in order to short the five sections together. The DC blades are the same as the RF blades to maintain symmetry, but the sub-electrodes are not shorted together. This is displayed in Figure 13. The blade on the left is the RF blade and the gold coating covers the entire surface. The DC blade is on the right, and one can see that toward the outside of the blade, there are uncoated sections allowing the five blade subsections to be individually biased.

As seen in Figure 14, the blades are set at angles so that the smaller angle between the

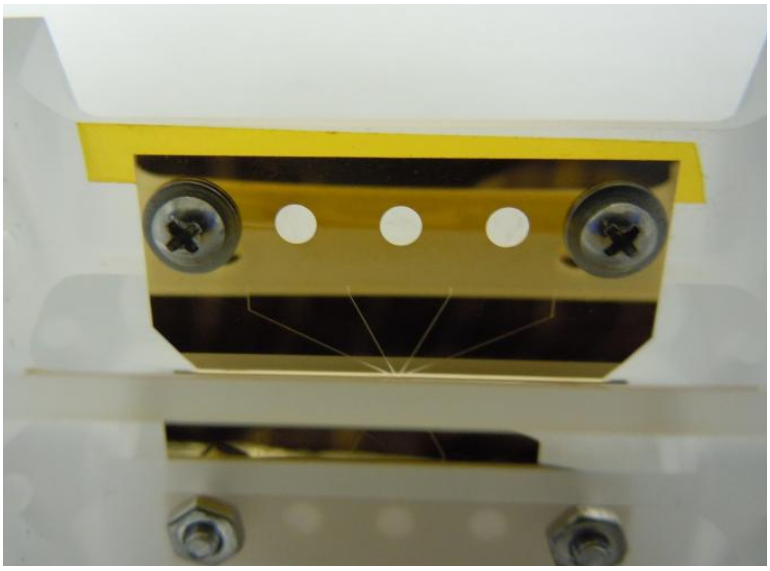

Figure 12: **RF blade displayed to show the five blade subsections**: Since this is an RF blade, the five sub-electrodes of the blade are shorted together at the top. For a DC blade, the five sub-electrodes are completely separate to allow for separate biasing.

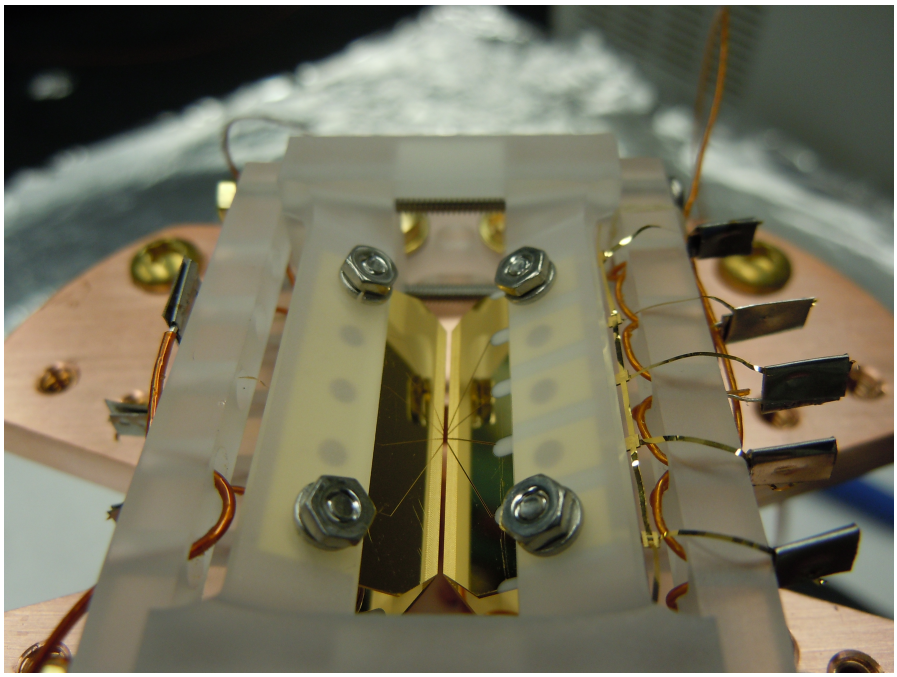

Figure 13: **RF and DC trap blades**: A DC (right) and RF (left) trap blades are pictured in a Saphire holder.

blades is 60° and the large angle is 120°. This blade arrangement is used for the following reasons. The ions are imaged from the bottom where the angle is wider. This way, the blades do not interfere with the Numerical Aperture (NA) of the imaging objective. Having the 60/90 blade configuration allows for the principle axes of the trap to be twisted. This is explained well in the thesis of Kale Johnson (5). This means that the strength of the transverse principle axes of the trap can be tuned and that the transverse principle axes of the trap can be rotated about the axis of the trap.

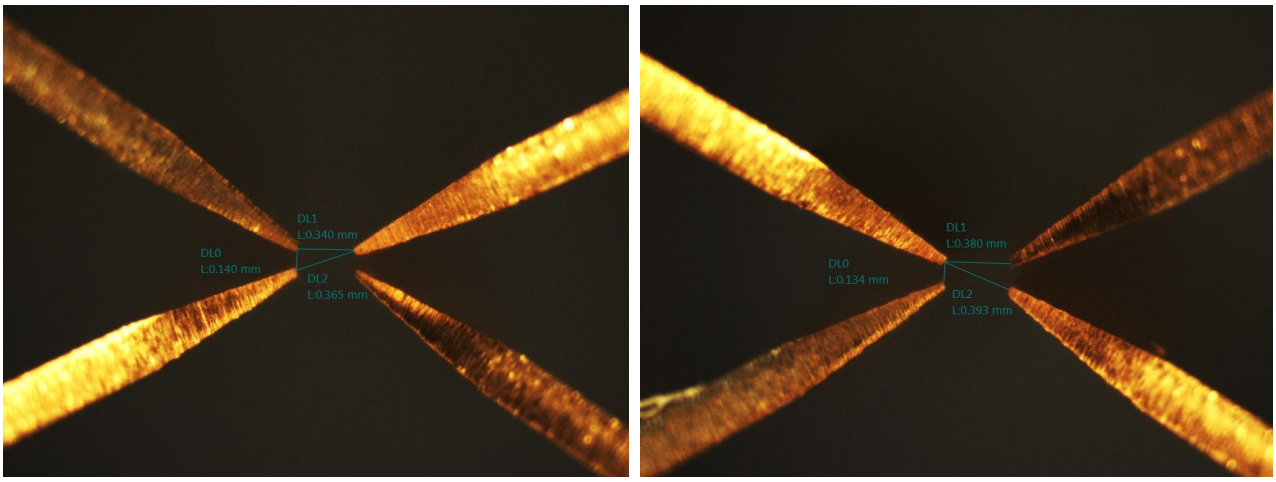

Figure 14: **both sides of the trap being measured**: The left picture shows the dimensions: vertical spacing: 0.140 mm, horizontal spacing: 0.340 mm. The right picture shows the dimensions: vertical spacing: 0.134 mm, horizontal spacing: 0.380 mm.

The central sub-electrode is 250 μm wide. For context, the length of the 121 ion chain pictured in Figure 1 is 500μm. The space between the center sub-electrode and the electrodes on either side is 100μm and the symmetrical sub-electrodes on either side of the center one are roughly as wide as the central electrode. When looking at the ion trap from the end (Figure 14), the spacing at the tip of the blades is roughly 140μm vertically and 340μm horizontally.

The macroscopic blades are effective with shielding the ions from electric fields originating

from outside the trap blades. There are certainly stray fields but they are likely from the dielectric substrate of the blades getting charged up. This can happen from the high power 355 beams scattering off the blades. This effect is apparent with a long ion chain trapped in a weaker potential. Upon flashing the two 355 beams, the ion chain correspondingly shifts up or down.

When the RF power drives the trap, there is heat dissipated on the RF trap blades. In a cryogenic vacuum chamber, large thermal gradients could build up and potentially cause harm to the trap. Using Solidworks, a total of 10W of heat was simulated to be dissipated across both RF blades in the blade mount. This is a good estimate given the equation

$$P_D = \frac{1}{2} V_0^2 C^2 \Omega_T^2 R_s$$

where P_D is the RF power dissipated on the blades, V_0 is the RF voltage, C is the trap capacitance, Ω_T is the RF drive frequency, and R_S is the RF resistance of the RF blades, (36).

Thermal simulations were run on one trap design[14] with two different materials considered, namely Macor and Sapphire as shown in Fig.15. The simulation considered 10mW of power dissipated on the RF blades and that the mounting surface of the trap was held at 4K.

The highest temperature simulated on the Macor and Sapphire trap assembly simulations were 15K and 5K respectively. The blades are made of Alumina and were considered to have a similar coefficient of thermal conduction as Sapphire. In particular, the blades are made of laser machined alumina from Sandia National Lab. The gold coating on the blades is adhered

[14]These simulations were carried out by Paul Hess. He did simulate the thermal distribution on another trap design as well, but the discussion here will be limited to the trap design that was used in the cryogenic system.

Figure 15: **Thermodynamic simulation of trap assemblies**: **Left:** Simulation using a Macor blade holder. **Right:** Simulation using a Sapphire blade holder. For both of these simulations, the surface that is mounted to the rest of the apparatus is held at 4K and the RF blades have 10mW total dissipated across both of them.

to the alumina with an intermediate titanium adhesion layer. Based on these simulations, the trap assembly was made out of Sapphire.

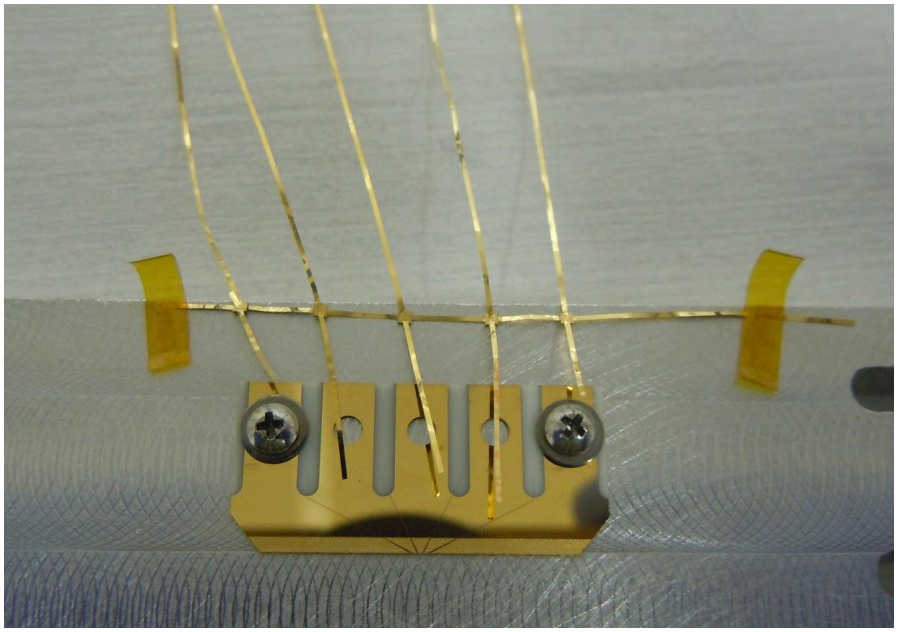

Figure 16: **DC blade with gold ribbons attached**: Gold ribbons attached to DC sub-electrodes to make electrical connections. The horizontal ribbon (as pictured) is connected to each of the other ribbons through a capacitor and is grounded to filter out RF noise from being picked up by the DC electrodes.

Each sub-electrode of the DC blades is wire-bonded to a gold ribbon as pictured in Figure

16. The horizontal ribbon (as pictured) is connected to each of the other ribbons through a capacitor and is connected to ground. This serves as an RF short to ground to filter out any RF that may be picked up by the DC blades and the associated gold ribbons. These gold ribbons are connected to more durable (and insulated) wires with the pad as shown in Fig.21[15]. These wires are connected to an RF filter board that is connected to the side of the resonator, Fig.17. These wires that are attached to the top of the filter board pass through heat-sink bibbins and are connected to the vacuum electrical feed-through at the top of the vacuum chamber. Figure 18 shows the vacuum chamber with the radiation shields removed. The 40K and 4K stages are shown with heat-sink bobbins attached. When wiring the cryostat, these wires were wound around the bobbins and covered with thermally conducting epoxy to thermally sink them.

[15]Figure 19 shown a previous method of connecting the gold wire to the durable wire using an aluminum 'flag'

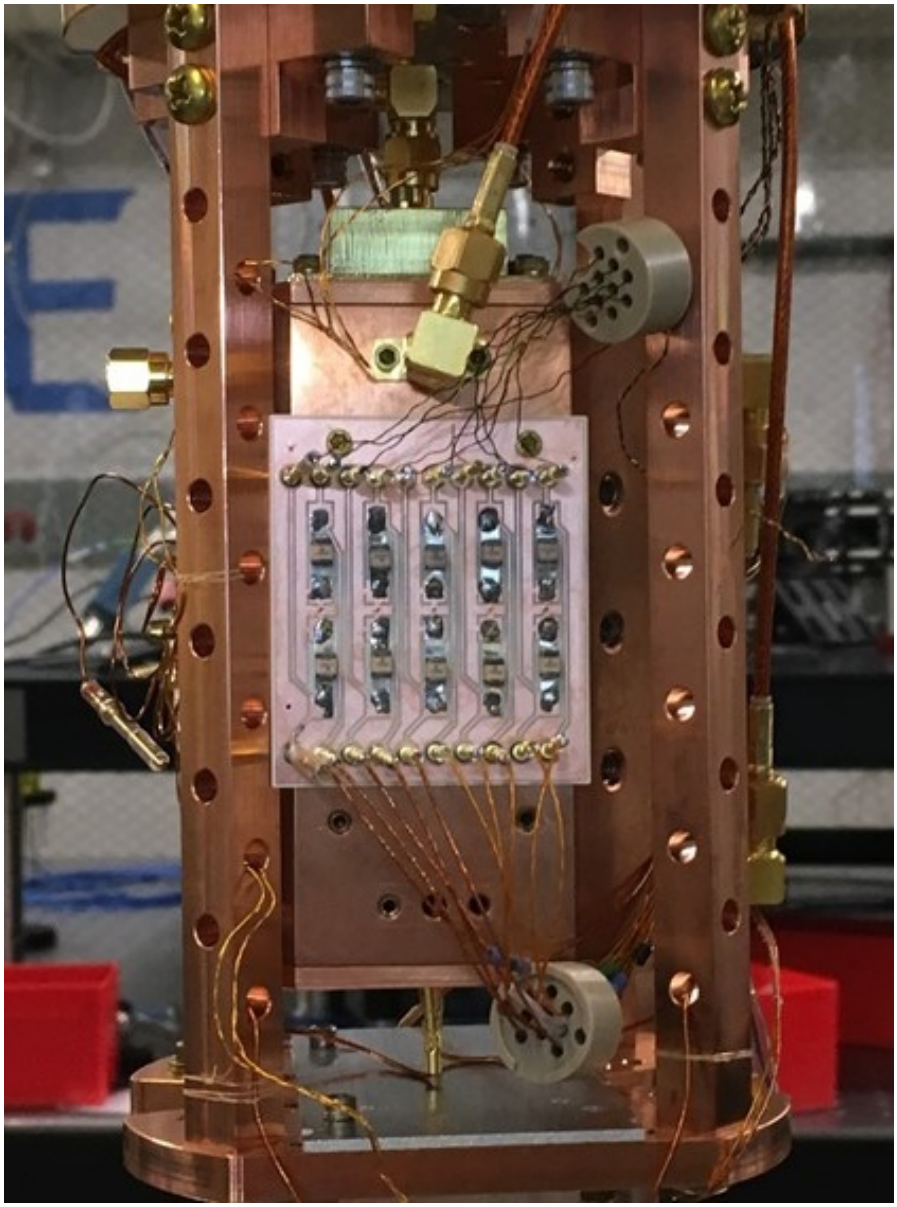

Figure 17: **Filter board mounted on resonator**: Here, the filter board is mounted on the side of the resonator to filter out RF signals from falling onto the DC blades.

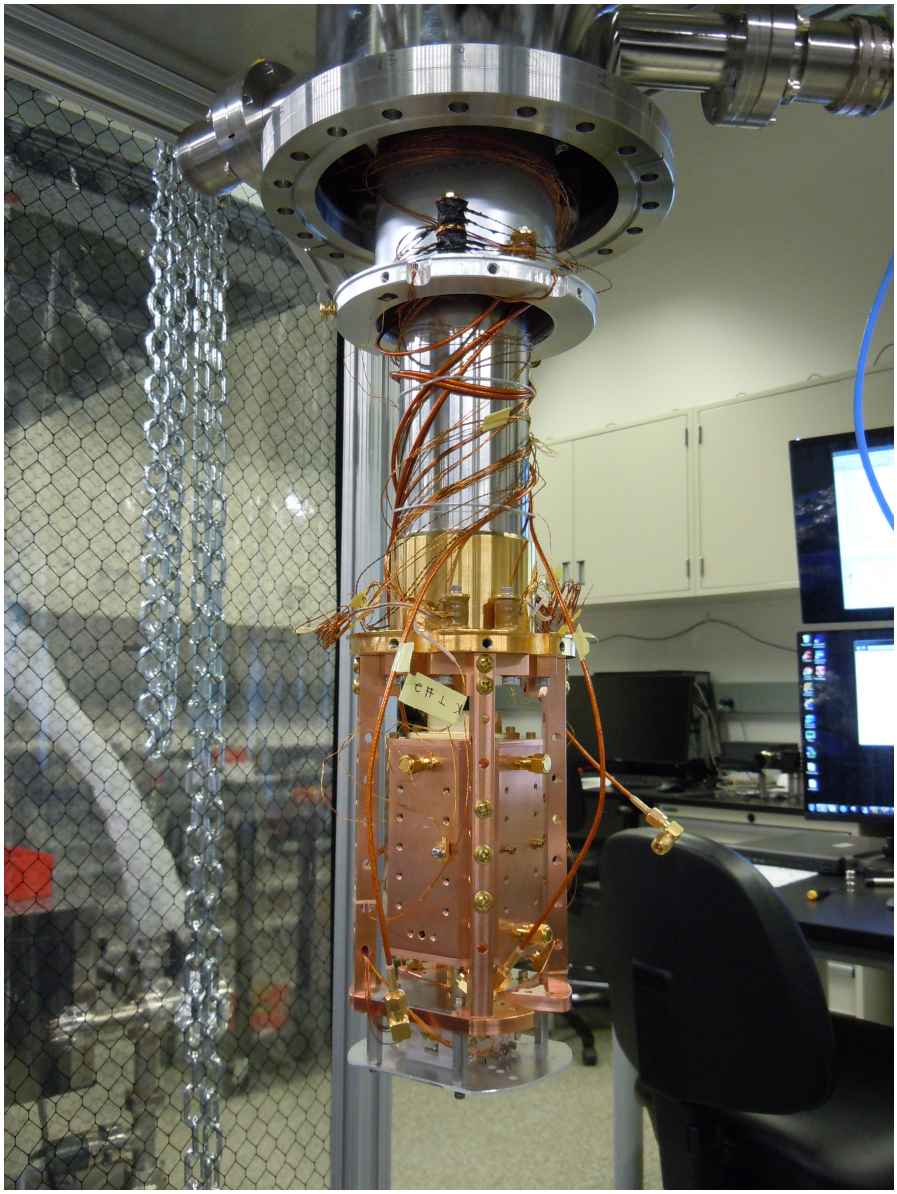

Figure 18: **Cooling Stages** : The inside of the cryostat is shown with the radiation shields removed. The DC wires are heat-sunk to the 40K and 4K heat stages with bobbins that are coated in thermally-conducting epoxy. The SMA cables are not heat-sunk.

12 Trap and Yb oven design

Over the course of setting up the lab, three different traps were used before settling on one of them and using it for conducting experiments.

Figure 19 shows the first trap assembly. The gold ribbons (as shown in Fig. 16) are connected to wires through metal flags that are wire-bonded together. As for the oven, Figure 19 shows one oven in a Macor holder. Though only one is pictured, there were two such ovens, one on each side of the trap. One was filled with natural abundance Yb and the other was enriched with ^{171}Yb. When loading ions, the ovens would heat up the entire 4K stage. This would cause He to blow out of the exchange gas region and cause the trap to move due to thermal expansion/contraction. Because of this, the pointing of the Doppler cooling laser would have to be adjusted as the ovens were ramped up and down. This entire process took anywhere from 30 minutes and longer. Both ^{174}Yb and ^{171}Yb were trapped, but the process was tedious and not conducive for work with long ion chains.

As time went on, the performance of this first trap progressively degraded and it became harder to load ions. At this point, the voltage on the trap blades was sourced from a precision voltage driver (iseg). The instrument registered how much current was flowing to or from each electrode and it was discovered that current on the order of 0.2-0.3mA was flowing between electrode blades. The first theory was that, given the extended loading times with the oven on, Yb 'bridges' formed between the electrodes. The response was to deliberately send current through the shorted electrodes to heat the Yb bridges off of the blades. While this did seem to work, other 'bridges' emerged and the general health of the ion trap declined.

By inspecting individual blades, it was discovered that the Gold coating was peeling off

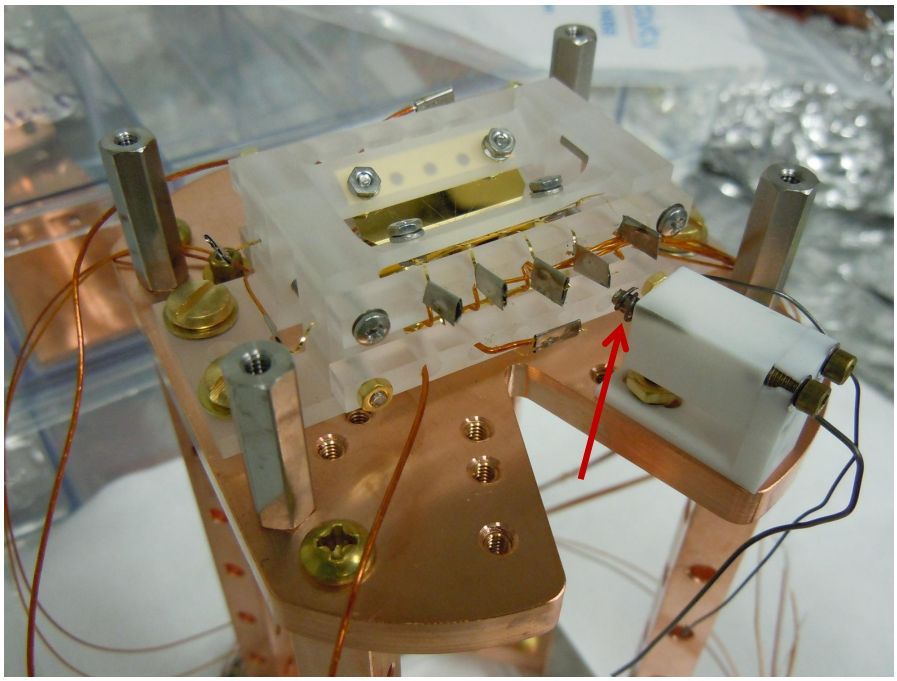

Figure 19: **First oven model mounted with trap**: The red arrow is pointing to the tube/oven that has a sample of Yb foil inside.

the blade surface and leaving the underlying Titanium adhesion layer exposed. Perhaps there were Yb bridges, but there also were gold flakes peeling off that could curl-up and contact a neighboring electrode to make an electrical short. Perhaps the process of heating up the Yb bridges induced more Gold peeling. During this phase of the experiment, a lot of heat and thermal gradients were applied to the blades and could have instigated this process.

The oven was upgraded to a more sleek design pictured in Figure 20. This oven featured a rounded Macor holder and ceramic beads insulating the leads. Subsequently, both the trap and the ovens were further upgraded. Instead of using the flags for the wiring, a pad made out of laminate (Roger) that was coated with conducting copper traces was used. This made the trap less fragile and more organized in terms of the wiring (Fig. 21).

With the second trap, a so-called 'room-temperature' oven, located outside of the 40K

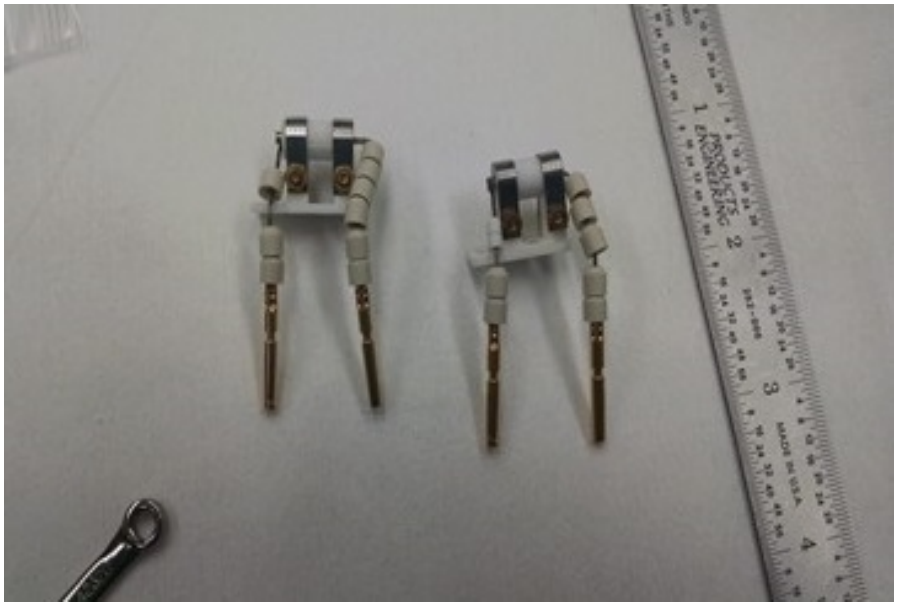

Figure 20: **Second version of oven**: The oven is held in a Macor holder with ceramic beads to insulate the leads to prevent heat transfer away from the oven when loading ions.

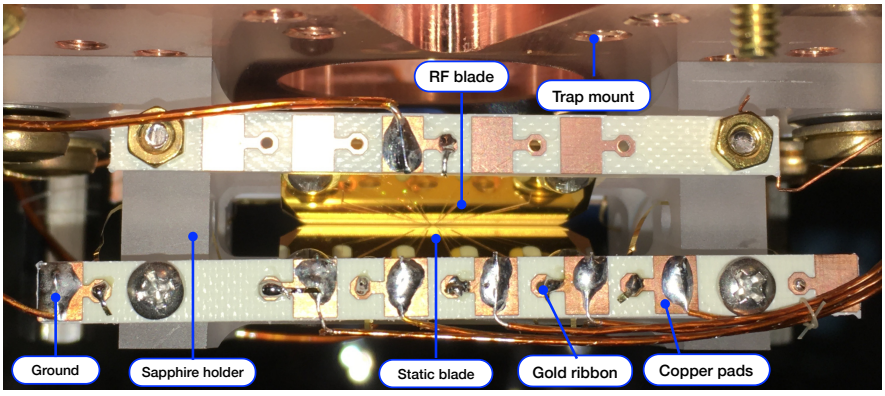

Figure 21: **Second ion trap**: Neatly placed pads with conducting traces were used to make the trap more organized and easier to build.

radiation shield, was introduced to the system. Figure 22 shows the room temperature oven on a vacuum flange. This was mounted in place of the east vacuum window[16]. The East-facing windows on the 40K and 4K stages were removed and replaced by aluminum plates with a 5mm in diameter hole to allow Yb from the oven to travel to the trap. The hole placement was calculated assuming that the 'anchor' point for the thermal expansion/contraction was near the top of the vacuum chamber where the rubber bellows are attached.

At this point, the room temperature oven was controlled by an automated ramp. On one day (March-21,2017), the program malfunctioned and ran the oven at 9 Amps for about 10 minutes, while the maximum current used previously was 3 Amps. The result was that the oven was coated in Yb and the window across from the oven was coated as well. And is pictured in Figure 23. After this event, there were extreme stray fields and no ions were able to be trapped. With this, a third trap construction was necessary.

The third trap consisted of a different blade arrangement. The RF blades were replaced with solid blades[17]. They are the same as the other blades used, but without individual trap blades patterned into the trapping edge. Figure 24 shows a closeup of the new RF blade mounted across from a standard static blade. One can see that the individual sub-electrodes are not present. This idea was tried under the assumption that having RF blades without segments would make for a more regular trapping potential. In practice, this removed symmetry from the system and resulted in an axial potential profile with more structure.

After experimenting with the third trap, the second trap was used again. Due to the placement of the room-temperature oven relative to the trap, there were no shorted blades,

[16]There are eight windows providing optical access to the ions. The windows can be labeled with the cardinal directions according to where they are facing: N, NE, E, SE, ...

[17]There were no sub-electrodes on the blade substrate.

Figure 22: **Room-temperature oven setup**: The oven design is the same as in Fig. 20, but on a vacuum flange so it can be placed far from the 4K region.

Figure 23: **Negative of trap blades along axis of room-temperature oven** : Accidentally, the room-temperature oven was on 9 Amps for about 10 minutes and the insides of the vacuum chamber became coated in Yb. Here is an artifact from this event.

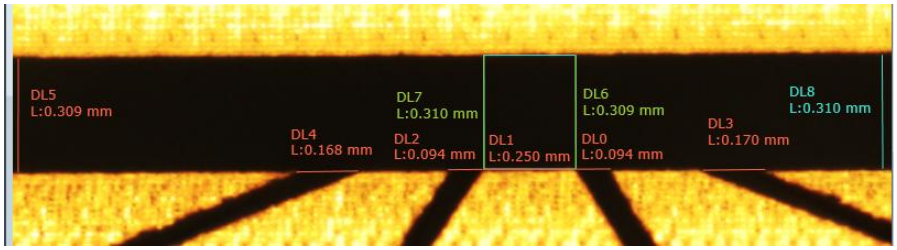

Figure 24: **Trap#3 used a RF blade that was not segmented**: The top blade is the non-segmented RF blade and the bottom is the regular segmented DC blade.

and any stray fields were able to be compensated for. The second trap is currently in use and has been used to take all of the experiments to date.

13 Diode laser systems

The diode lasers in use in the lab are Moglabs direct diode external cavity lasers which supply the lab with 369nm, 399nm, and 935nm light. The light from these lasers are used for: Doppler cooling, optical pumping, state detection, loading (ionization), and for repumping the ions to stay in the (near) cycling transition.

13.1 369nm laser light

Figure 25 shows the 369nm laser breadboard with branching beam paths. The 369nm light is split up into 3 fiber couples going to the experiment, the transfer cavity, and to the wavemeter (WS7 HighFinesse wavemeter). As with all of the diode laser breadboards, all of the branches are fiber coupled and the breadboard itself rests on Sorbothane brand vibration isolating material. In general, the diode lasers are sensitive to mechanical vibrations and will respond to a disturbance such as from the lab door opening quickly. The power coming out of the laser head has been progressively decreasing over its lifetime. The initial power value was 8 mW. Currently it has between 4.5 mW and 5 mW.

Before going to the experiment, the 369nm light goes to the so-called 'distribution board' Fig. 26. Here, the light is separated into detection, optical pumping, and Doppler cooling light. The detection light passes through an AOM driven at 318MHz and the $+1^{st}$ diffracted order is used. This frequency is sourced from one of the 10 DDS channels on the Sandia box[18].

The optical pumping light passes first through a 2.105GHz EOM driven at 2.115GHz with a Lab Brick Signal Generator LSG-402 and then a 300MHz AOM driven by one of the Sandia

[18]The Sandia box is an experiment control program that was created at Sandia national lab.

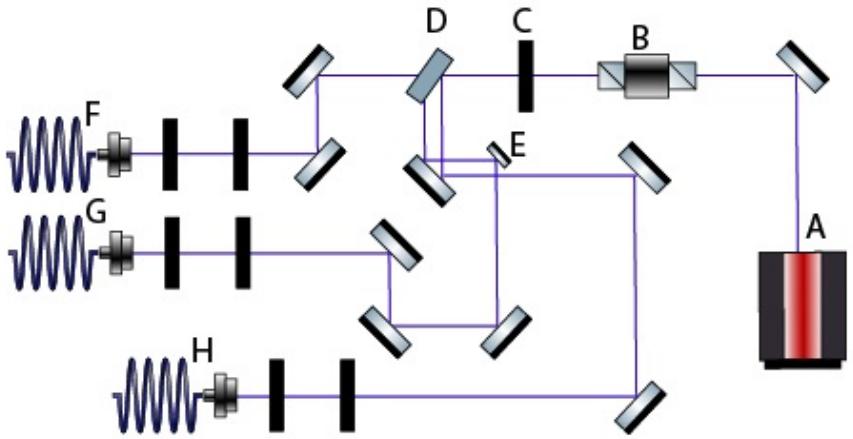

Figure 25: **369 Diode Laser Breadboard**: **A**: Moglabs direct 369nm external cavity diode laser. **B**: Optical isolator. **C**: $\lambda/2$ wave-plate to govern how much power transmits and reflects from the next element. **D**: Thick piece of glass, creating one transmitted beam and two strong reflected beams. **E**: D-mirror to pick off the secondary reflection from D. **F**: Fiber coupling to the rest of the experiment. **G**: Fiber coupling to the transfer cavity. **H**: Fiber coupling to the wavemeter for frequency locking. Each of the fiber couplings have a $\lambda/2$ and $\lambda/4$ waveplate before them to adjust the polarization going into the fiber.

box DDSs. This EOM is driven at a higher frequency, by 10 MHz, so that the AOM can be driven at a lower frequency to make the requisite optical pumping frequency. The EOM driving power was selected so that the 0^{th} order is negligible, but this precaution considers the case where there is some light in the 0^{th} order of the EOM. In this case, there will be light in the optical pumping beam that is only be shifted by the AOM. If the AOM frequency is too close to the detection AOM frequency (318 MHz), then there will be some detection light in the optical pumping beam. For this reason, the EOM is driven at an increased frequency so that the AOM can be driven at a frequency farther from the detection AOM driving frequency. The value of 10 MHz was picked as it is comfortably within the bandwidth of the optical pumping EOM and AOM. The detection and optical pumping light are combined on a PBS and sent to the experiment in the same optical fiber.

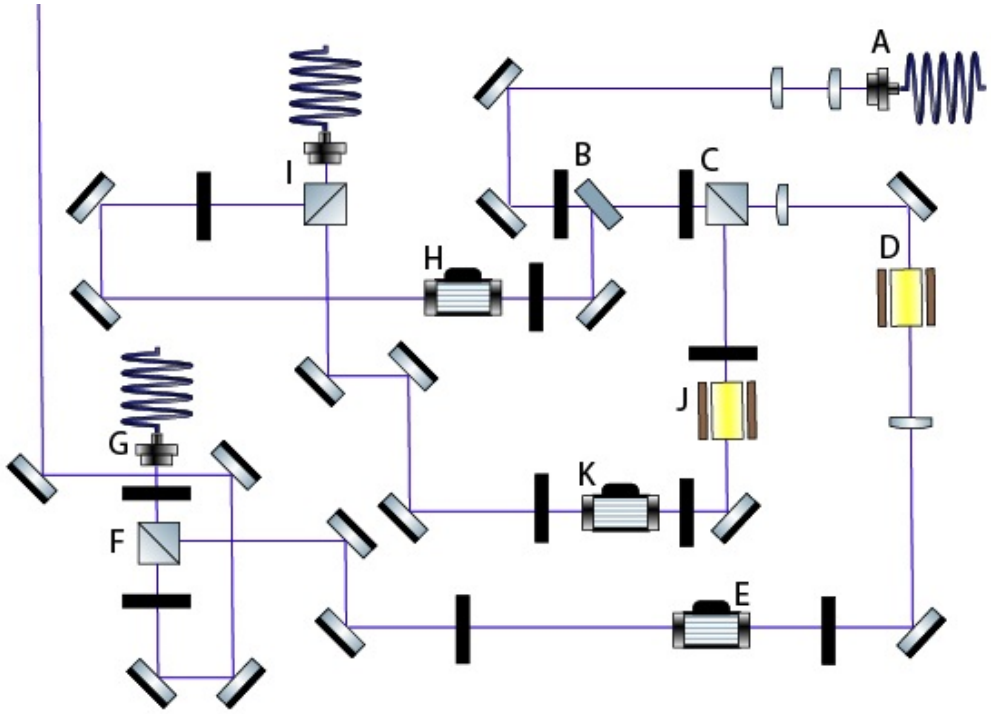

Figure 26: **369 Distribution Board**: Here, the 369 laser light is divided into the various 369 functions. **A**: Fiber coupling from Fig.25F. The two subsequent lenses are used to collimate the the beam. **B**: A $\lambda/2$ waveplate and a glass beam splitter to siphon off power into the detection path. **C**: A $\lambda/2$ waveplate and a PBS to siphon off power into the optical pumping path. **D**: Doppler cooling (DC) EOM. There is a lens before and after in order to focus the light through the small EOM aperture. **E**: DC AOM. **F**: PBS to combine DC light and other farther detuned cooling light. Currently, the farther detuned light is not used. **G**: Fiber coupling to the experiment. **H**: Detection AOM with a $\lambda/2$ waveplate in front. **I**: PBS to combine detection and optical pumping light into the same fiber coupling. **J**: Optical pumping EOM with a preceding $\lambda/2$ waveplate. **K**: Optical pumping AOM with a $\lambda/2$ waveplate before and after.

The Doppler cooling light passes through a 7.374GHz EOM (driven by Lab Brick Microwave Signal Generator LMS-802) and then though an AOM at 285 MHz (driven by one of the Sandia-box DDSs) where the $+1^{st}$ diffracted order is used. This light is sent to the experiment through an optical fiber. If another farther red detuned cooling beam is needed, it can be sent in the same optical fiber as the regular cooling light because there is a PBS before the fiber coupling with an empty port.

The detection and optical pumping light arrive at the experiment breadboard (Fig 32) through a common optical fiber. The two beams are shaped by a series of cylindrical lenses so the beam has an elliptical profile when focused onto the ion chain. Both these beams contain $\sim 20\,\mu$W of power and have a waist of $\sim 40\,\mu$m by $\sim 835\,\mu$m vertically and horizontally respectively. The Doppler light is similarly sent through a fiber to the experiment breadboard and shaped so it will hit all of the ions in the chain. The power in this beam is $\sim 60 - 100\,\mu$W and the beam waist measures $22\,\mu$m by $88\,\mu$m[19] vertically and horizontally respectively. Specifically for Doppler cooling, the light needs to hit the ion chain such that its $\vec{k}$ vector has projections along all three trap principle axes and can therefore cool motion along all axes. The mirrors in the DC beam path are adjusted to create these conditions.

13.2 399nm laser light

The 399nm light is used for the second stage of ionization and is therefore only needed during ion loading. As shown in Figure 27, the laser light is sent to the wavemeter, transfer cavity, and to both this experiment and the experiment next door. There is a flipper-mirror that

[19]These measurements are the $1/e^2$ intensity radius.

routs the light either to go to this experiment or to the experiment next door. The power out of this laser is $\sim$ 7.4 mW and the power reaching the ions is $\sim$ 1.4 mW of power. The 399 light travels to the experiment breadboard through a fiber (Fig. 32), gets shaped and has a waist of $\sim 43\,\mu$m by $\sim 243\,\mu$m vertically and horizontally respectively at the ion chain. In general, this beam does not need to be as wide as the entire chain, because it is just for ion loading.

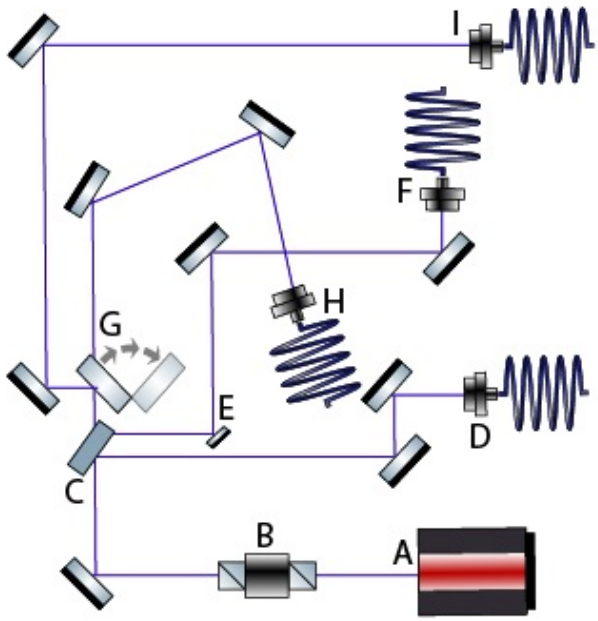

Figure 27: **399 Diode Laser Breadboard**: **A**: Moglabs direct 399nm external cavity diode laser. **B**: Optical isolator. **C**: Beam splitter with two reflections. **D**: Fiber coupling to the wavemeter. **E**: D-mirror to pick off the secondary reflection. **F**: Fiber coupling to cavity. **G**: Flipper mirror to switch the beam between this experiment or the experiment next door ("Networks" lab). **H**: Fiber coupling to the experiment. **I**: Fiber coupling to the lab next door.

13.3 935nm laser light

The 935nm laser path is shown in Figure 28. The beam is passed through a pair of Anamorphic prisms in order to change the beam cross-section from an ellipse to a circle. This should allow

for more efficient fiber coupling. The 935 light is sent to the wavemeter and to the experiment. In the past, there was another branch sending light to the transfer cavity, which was removed. The light coming out of the laser head is ~ 66 mW and the power reaching the ions is ~ 11 mW.

The 935nm light going to the experiment is fiber coupled into a fiber-coupled EOM (EOSpace PM-0S5-10-PFA-PFA-935-UL). This EOM is driven at 3.0695 GHz using the Lab Brick Signal Generator LSG-402. If the 935nm light is not properly fiber coupled to the polarization-maintaining (PM) optical fibers, then the polarization can drift around on the time scale of minutes and negatively effect ion detection. The output of the fiber-coupled EOM is coupled into another PM fiber and sent to the experiment breadboard, Figure 32. Here, the laser beam is shaped and focused onto the ion chain with a waist of $\sim 20\,\mu$m by $\sim 850\,\mu$m vertically and horizontally respectively.

13.4 Transfer cavity lock

The transfer cavity was designed to lock both 369nm lasers[20], 399nm, and 935nm lasers. A reference 780nm laser is locked to a Rb vapor cell resonance and used to lock the cavity. Presently, only the 369nm laser is locked to the cavity and the other lasers are locked using the wavemeter. The cavity length is scanned over a free spectral range (FSR) of the 780 light. Each of the other frequencies are locked by adjusting their frequency to be positioned as a fixed proportion of the 780 FSR.

The transfer cavity is made from one planar mirror, and one concave mirror with a radius

[20]Currently, only one 369nm diode laser is used in the experiment, but there is a second one which is on the optical table and coupled to the transfer cavity.

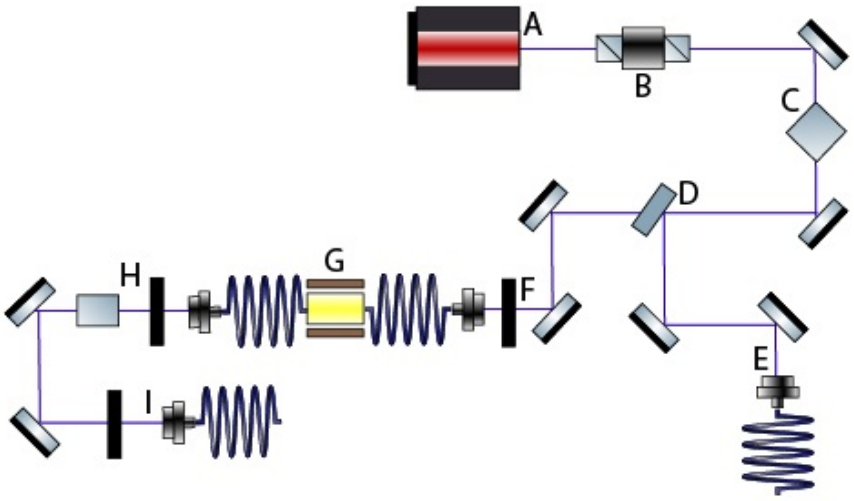

Figure 28: **935 Diode Laser Breadboard**: **A**: Moglabs direct 935nm external cavity diode laser. **B**: Optical isolator. **C**: Anamorphic prism pair used to shape the beam from having an elliptical profile to having a circular one. **D**: Beam splitter. **E**: Fiber coupling to wavemeter. **F**: $\lambda/2$ waveplate to align the polarization-maintaining optical fiber. **G**: Fiber-coupled EOM. **H**: $\lambda/2$ waveplate and a Glan-Thompson polarizer. To maximize the power out of the polarizer. **H**: $\lambda/2$ waveplate and fiber coupling to the experiment.

of curvature of 500mm. These mirrors are separated by ~ 7.5 inches, and are placed on either end of an invar hollow cylindrical spacer. The concave mirror is directly attached to a hollow cylindrical piezo which is in turn connected to the invar spacer. Modulating the length of the cavity allows for different frequencies to be locked by a single cavity. The cavity is placed in a vacuum chamber so there is no atmosphere to change the index of refraction and thereby perturb the measured frequencies. Figure 29 shows the vacuum chamber housing the cavity.

14 Coherent microwaves

The system is outfitted with a microwave horn in order to coherently drive global spin rotations. The $|\downarrow\rangle$ and $|\uparrow\rangle$ states are directly coupled by a magnetic dipole moment, so the microwaves can directly drive rotations. The source of the RF power is a HP 8672A signal

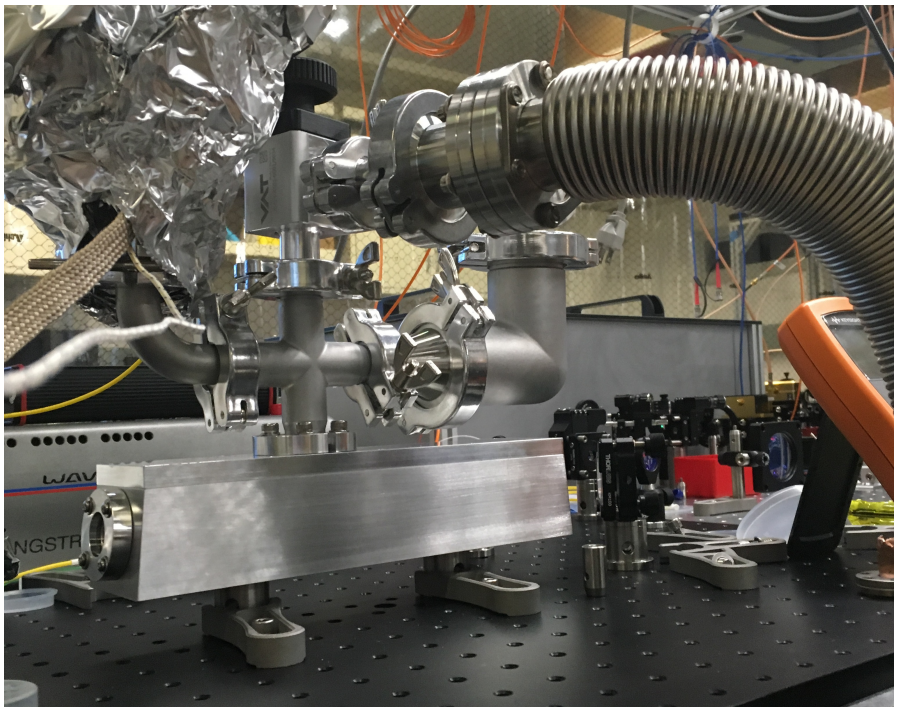

Figure 29: **Transfer cavity vacuum chamber**: The transfer cavity is placed in a vacuum chamber to increase stability of frequency measurements.

generator. This signal it sent through a power splitter (ZX10-2-183+) so it can be used for the microwave setup and the Raman beat-note lock. The HP8672 signal is mixed with a 200 MHz signal from a DDS channel (Sandia box) using a mixer (ZX05153+). Using the mixer allows one to control the microwave with the DDS channel. After the mixer, the signal is sent through a pre-amp (ZX60-183-S+) and then a 3 Watt amplifier (ZVE-3W-183+). The amplified signal is sent directly to the microwave horn. The microwave horn directly drives the carrier transition at 12.642812G Hz. The HP8672 is set to 12.442812 GHz so when mixed with the 200 MHz DDS signal, the resultant signal will drive the carrier.

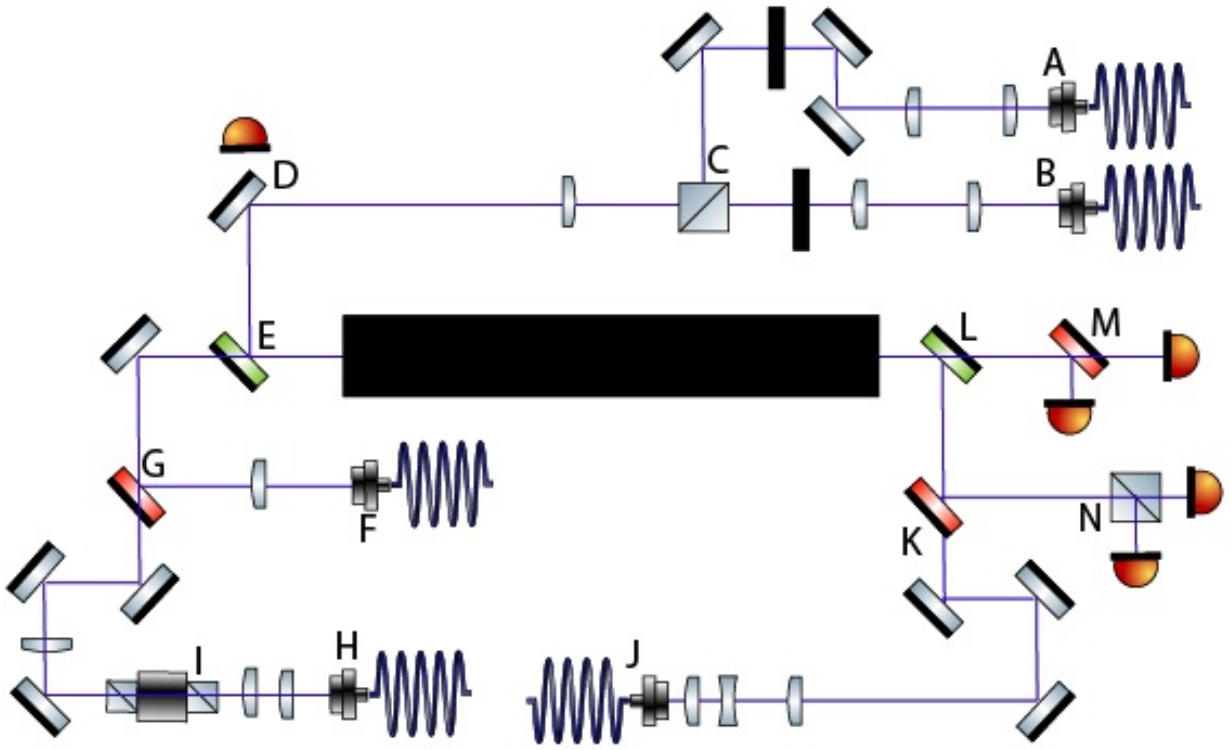

Figure 30: **Transfer cavity breadboard**: This is where the diode lasers (369nm, 399nm, 935nm) can be precisely locked to a reference 780nm laser using the transfer cavity. In practice, only the 369 lasers are locked here. All of the lenses are selected to match the longitudinal mode of each laser beam with that of the cavity. **A**: Fiber coupling from the 369b laser. This is a 369 diode laser that is intended for future experiments. **B**: Fiber coupling from the main 369 diode laser. **C**: PBS to combine both 369 beams. Each beam has a $\lambda/2$ waveplate before the PBS to maximize power to the cavity. These beams are kept separate with orthogonal polarization. **D**: This mirror is placed where a dichroic beam-splitter used to be. The dichroic would allow 399 light to pass to the PD. **E**: Dichroic beam splitter that reflects the UV frequencies and transmits the 780 and 935 light. **F**: Fiber coupling from the 780 reference light. **G**: Dichroic beamsplitter reflecting 780 light and transmitting 935 light. **H**: Fiber coupling from the 935 laser. **I**: Optical isolator for 935. **J**: Fiber coupling from the 399 laser. **K**: Dichroic beamsplitter separating 399 and 369 light. **L**: Dichroic beamsplitter separating between UV frequencies and 780 and 935. **M**: Dichroic beamsplitter allowing 935 light to pass and 780 light to reflect and fall incident on their respective PDs. **N**: PBS to distinguish light from the two 369 lasers and send them to individule PD detectors.

15 355nm pulsed laser system

15.1 Optical layout

The Coherent Paladin Advanced 355-24000 laser is used for all of the coherent spin manipulations and the long-range spin-spin coupling. The laser is pulsed and outputs 24W of 355nm light. The repetition-rate is 82MHz and the pulse length at 1064nm is between 15ps and 20ps. The optical setup is displayed in Figure 31.

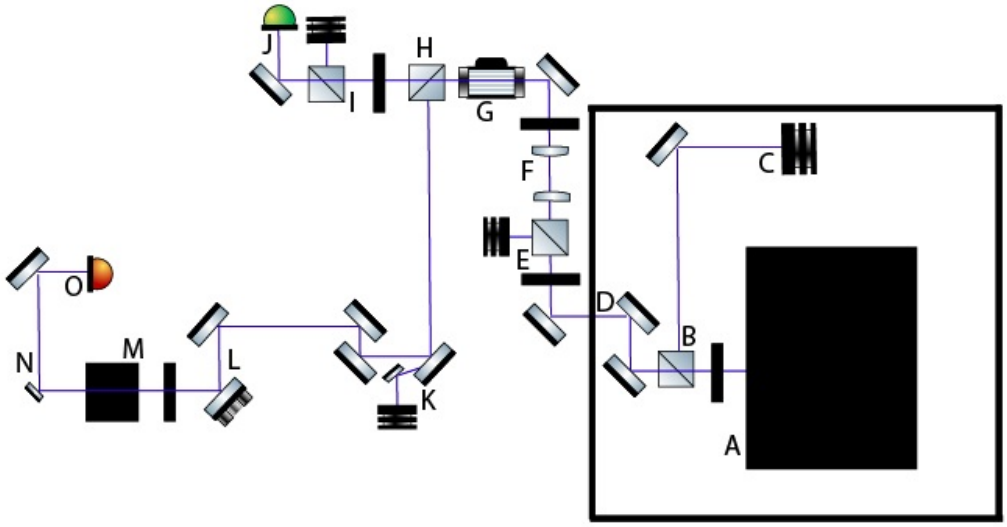

Figure 31: **355 frequency comb layout (optics table level)**: Here is the optics layout for the 355 pulsed laser directly out of the laser and on the main optics table. **A**: Paladin laser system, 24W 355nm pulsed laser. **B**: High power PBS and $\lambda/2$ waveplate to divide the high power beam. **C**: High power, water-cooled, beam dump to dump 20W of power. **D**: The remaining 4W of power are sent through a hole in the laser enclosure. **E**: High power PBS and $\lambda/2$ waveplate to switch between high and low power modes. **F**: Two lenses: The first lens collimates the beam. The second lens has a very long focal length of ∼1000mm. **G**: Noise-eating AOM with preceding $\lambda/2$ waveplate. **H**: PBS separating the path to the experiment from the path to the beat-note lock. **I**: PBS and $\lambda/2$ waveplate sending some of the light to a beam dump. **J**: Alphalas, fast PD. **K**: D-mirror to dump the diffracted orders from the AOM (G). **L**: Piezo controlled mirror to lock beam pointing. **M**: Periscope to bring 355 light to the experiment breadboard. **N**: Trace light that transmits through the first mirror of the periscope is reflected by this D-mirror. **O**: PD for the 355 laser intensity lock.

The 24W laser is sectioned off in a protective[21] box to prevent exposure to scatter from the high power region. 20W of the power are dumped and the remaining 4W are sent to the experiment. The beam is sent through another $\lambda/2$ waveplate and PBS (E) switching between the experiment and a beam dump. This allows one to switch between sending high and low power to the experiment. The low power setting is used only for alignment and diagnosing problems. Otherwise, the high power setting is used for experiments.

The first AOM the beam passes through (G) is used to lock the intensity of the beam. The 0^{th} order is used for the experiment and the 1^{st} order is dumped in the beam dump (K). A small part of the power is siphoned off and directed to the fast Alphalas (UPD-30-VSG-P) PD (J) in order to lock the relative spacing between the frequency comb teeth (beat-note lock). In order to lock the beam pointing, the beam is reflected off a piezo-adjustable mirror (L). This mirror is intentionally placed such that the beam is not focused when reflecting off the mirror. This makes it so that when the mirror is deflected, the focused beam position on the ions moves. If the focus were placed at the mirror surface, then tilting the mirror surface would change the $\hat{k}$ vector at the ions, but not the location of the beam waist. This, of course, assumes that the beam is also focused on the ion chain.

The beam then passes into the periscope (M) to bring the beam up to the level of the experimental breadboard. The mirror at the bottom of the periscope allows some light to transmit through. This light is directed toward a PD (O) which is the locking signal for the beam intensity lock.

In the entire 355 beam path, the lenses are arranged in a telecentric arrangement[22]. Prac-

[21] somewhat...

[22] Excluding the first two lenses in Fig. 31

tically, this means that all the lenses are placed f-to-f, regardless whether the light is focusing of collimated between a given pair of lenses[23]. This optical arrangement is meant to reduce the amount of spherical aberration at the image (37) (38). Having few aberrations will help to focus the beams down to a small size and to be able to reliably predict the behaviour of the beam.

The 355 laser beam continues to the optics on the experiment breadboard which is shown in Figure 32. The beam is split up into two paths using a PBS (A). Before the periscope, there is a $\lambda/2$ waveplate to control the power split ratio. The two beams are called Raman1 and Raman2, as both beams are necessary to make spin rotations using a Raman scheme.

The AOMs (B) and (C) are respectively termed AOM1 and AOM2. The 355 beams are focused into these AOMs with a f=300mm lens which is in the periscope. The idea is that the beams are focused in the AOMs and also on the ion chain. Therefore, when the AOM deflects the beam at different angles, the beams fall on the ions without displacements.

Right after the beams are split into two, some of the light in beam Raman1 transmits through a mirror and is focused onto the 4-quadrant photodiode (AU). The signal from this photodiode if fed into a PID and used to lock the beam pointing through the piezo-mirror in Fig. 31 (L).

Both beam paths have a Glan-Thompson polarizer, (E) and (P), to control the polarization incident on the ions. There is a rejected beam from each of these polarizers, each of which is sent to a PD. This allows one to look at the PD signal on an oscilloscope and confirm weather the Raman1 and Raman2 beams are on or off.

[23]f-to-f means that two lenses that are placed consecutively in an optics setup are placed so the spacing between them is equal to the focal length of both elements added up. There can be other optical elements between the lenses as long as they are not lenses.

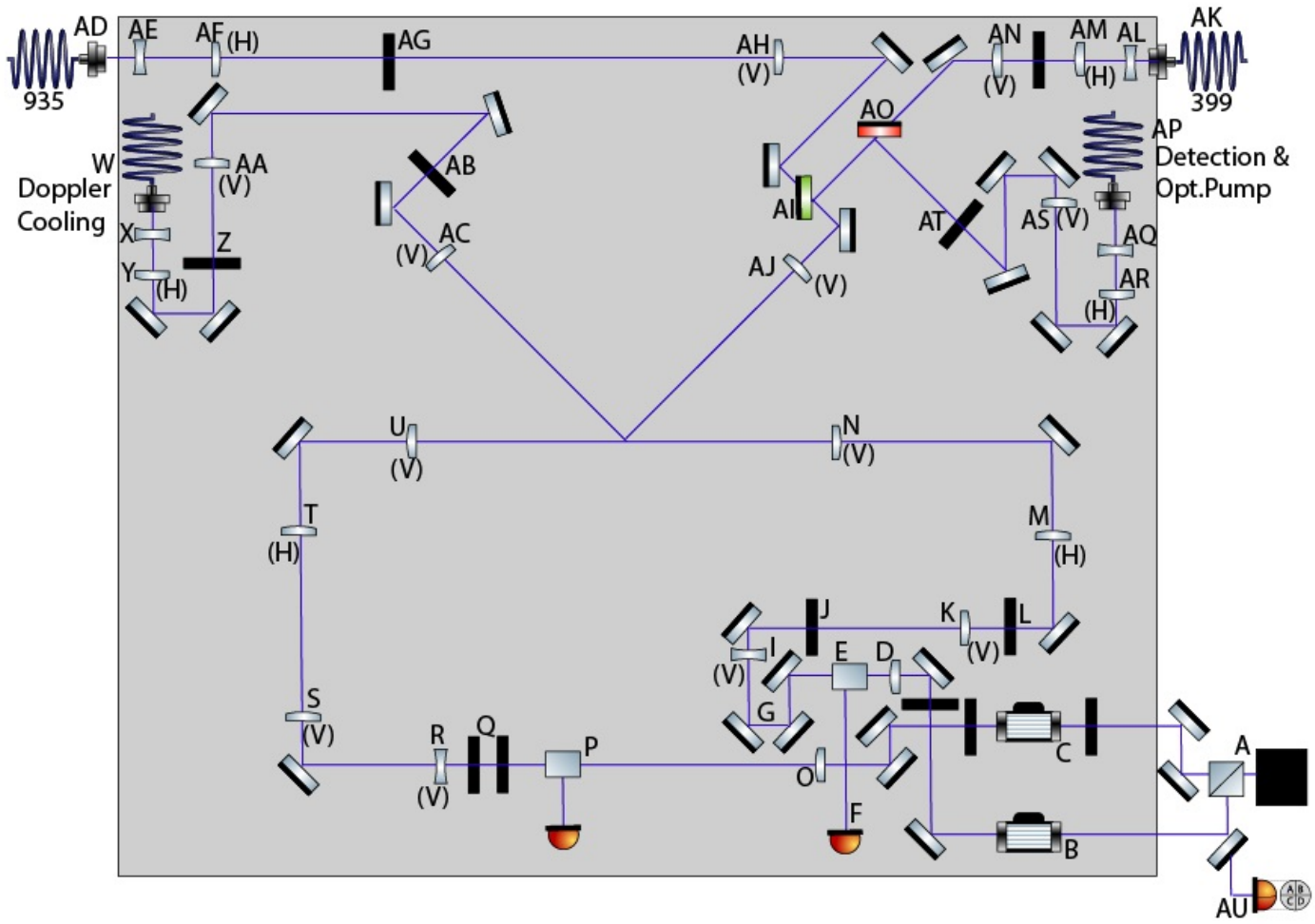

Figure 32: **Optical layout on the experiment breadboard**: The shaded region denotes the surface of the experiment breadboard. Cylindrical lenses are marked with (H) and (V) for horizontal and vertical. **A**: Top of the periscope. The 355 light is separated into two paths with a PBS. **B**: Raman1 AOM, **C**: Raman2 AOM with two $\lambda/2$ waveplates. **D**: f=300mm lens. **E**: Glan-Thompson (GT) polarizer. **F**: Rejected GT beam detected on PD. **G**: These two mirrors are on a translation stage to adjust the relative length of the Raman1 and Raman2 paths. **I**: f=-30mm lens. **J**: $\lambda/2$ waveplate. **K**: f=200mm lens. bf L: $\lambda/4$ waveplate. **M**: f=400mm lens. **N**: f=200mm lens. **O**: f=300mm lens. **P**: GT polarizer with rejected beam incident on a PD. **Q**: $\lambda/2$ and $\lambda/4$ waveplates. **R**: f=-30mm lens. **S**: f = 200mm lens. **T**: f=400mm lens. **U**: f=200mm lens. **W**: Fiber coupling for DC light. **X**: f=-125mm lens. **Y**: f=150mm lens. **Z**: $\lambda/2$ waveplate. **AA**: f=500mm lens. **AB**: $\lambda/2$ waveplate. **AC**: f=150mm lens. **AD**: Fiber coupling for 935 light. **AE**: f=100mm lens. **AF**: f=130mm lens. **AG**: $\lambda/2$ waveplate. **AH**: f=500mm lens. **AI**: Dichroic beams-plitter separating UV from 935. **AJ**: f=150mm lens. **AK**: Fiber coupling for 399 light. **AL**: f=-350mm lens. **AM**: f=250mm lens. Followed by a $\lambda/2$ waveplate. **AM**: f=500mm lens. **AO**: Dichroic beam-splitter, separating 369 and 399 light. **AP**: Fiber coupling for detection and optical pumping light. **AQ**: f=-125mm lens. **AR**: f=150mm lens. **AS**: f=500mm lens. **AT**: $\lambda/2$ waveplate. **AT**: Some light transmitts through the mirror and is focused on a 4-quadrant photodiode as part of the beam-pointing lock.

Each of the Raman beams pass through an identical set of optics to shape the beams and to focus it on the ions. The profile of the beams are as follows. The focus of the Raman beams have a horizontal and vertical waist ($1/e^2$ radius) of (190, 11)μm for Raman1 and a waist of (250, 12)μm for Raman2 respectively.

Each beam has a set of two polarizers, a $\lambda/2$ and $\lambda/4$ waveplate to set the polarization of the light on the ions. The $\lambda/4$ waveplate is turned to change the polarization between being linear and circular. Linear light is used for the experiment, and circularly polarized light is used to check the Light shift of an individual beam (explained later). In the Raman1 path, there is a delay stage (G). This can be adjusted in order to make the path for Raman1 and Raman2 the same length. This is necessary for the Raman process to work properly both for single spin rotations and for the MS protocol.

15.2 355 beam control

The Raman AOMs serve the function of providing the various frequencies necessary to coherently manipulate the spin chain. All rotations and the sidebands used in the MS scheme are derived from the resultant beat-note from a Raman process between beams Raman1 and Raman2. As explained thoroughly in the appendix, for each of these Raman processes, each ion is effectively absorbing a comb-tooth from one beam and emitting into a comb-tooth of another beam. The beat-note between the absorbed and emitted comb-teeth is the relevant frequency and not the absolute frequencies of the comb-teeth; though the absolute frequency is chosen so that it is detuned from the nearest resonances and will minimize spontaneous emission from these higher energy states (12).

Therefore, the beat-note between the two beams (two frequency combs) is what is locked, and the relative spacing between comb-teeth (the laser rep-rate) is allowed to drift. To be complete, the rep-rate could also be locked in order to lock the beat-note frequencies. In the present system, this is not a reasonable option as the Paladin laser in use does not have direct access to the internal cavity that would need to be stabilized.

The beat-note between Raman beams is stabilized using a feed-forward locking scheme. This is performed by adjusting the driving frequency to one of the Raman AOMs while the other AOM stays at a fixed frequency. Specifically, AOM1 is driven with a compensating frequency to preserve the Raman beat-note while AOM2 is used to scan and set the absolute frequency of the beat-notes used. This beat-note lock is the same as used in the warm experiment and is explained in the thesis of Crystal Senko (12).

15.3 Experiment control

The current experiment control program was written by Peter Maunz at Sandia National Labs and controls what is known as the Sandia box. It consists of 8 DDS channels, TTL outputs and input signal counters. It is written using the Python programming language, and has been integrated with the Andor iXon camera for data taking as well as the AWG (Keysight M3202A) for experimental control. It can be used to execute an arbitrary experimental sequence and allows for definition and use of global variables and their use in mathematical expressions to define other experimental parameters.

The entire lab is synchronized to a Rb clock (SRS FS725). This clock distributes 5 MHz and 10 MHz reference signals to equipment all over the lab. There is a 1 GHz frequency

reference (Wenzel 500-28884) that is fed into the Sandia box pulser box, as well as to an independent DDS source.

In a generic experiment, there are many RF tones that need to be placed on AOM2. While one can do this with individual frequencies from a set of DDS channels and combine them together, it is simpler and more versatile to use an AWG (arbitrary waveform generator). The Keysight M3202A, chassis mounted AWG is used to drive AOM2. This AWG is triggered from the Sandia box and allows a waveform to be easily programmed by means of typing a mathematical function.

16 Ion-state readout

16.1 Imaging system

The imaging system is used to collect ion fluorescence for ion state detection. The fluorescence is either focused onto a PMT, or onto an EMCCD camera (Andor iXon Ultra). The image of the ions gets focused onto the camera such that each of the ions are resolved and the florescence of each ion can be measured.

The imaging objective is custom made from Photon Gear, Inc. and made from off-the-shelf 2-inch diameter lenses from Newport optics. The lenses were bought, coated for 369.5nm and 355nm light, and sent to Photon Gear for assembly and testing. Figure 33 shows the lens stack that composes the objective with three pieces of glass between the ions and the objective lenses to simulate the glass from the vacuum chamber. The front NA is 0.43 and the back NA is 0.046; making the magnification nearly X10. The rays traced from the ions represents

the chief ray (center ray) and the extreme rays. This objective was designed in-house using Zemax optics simulation software.

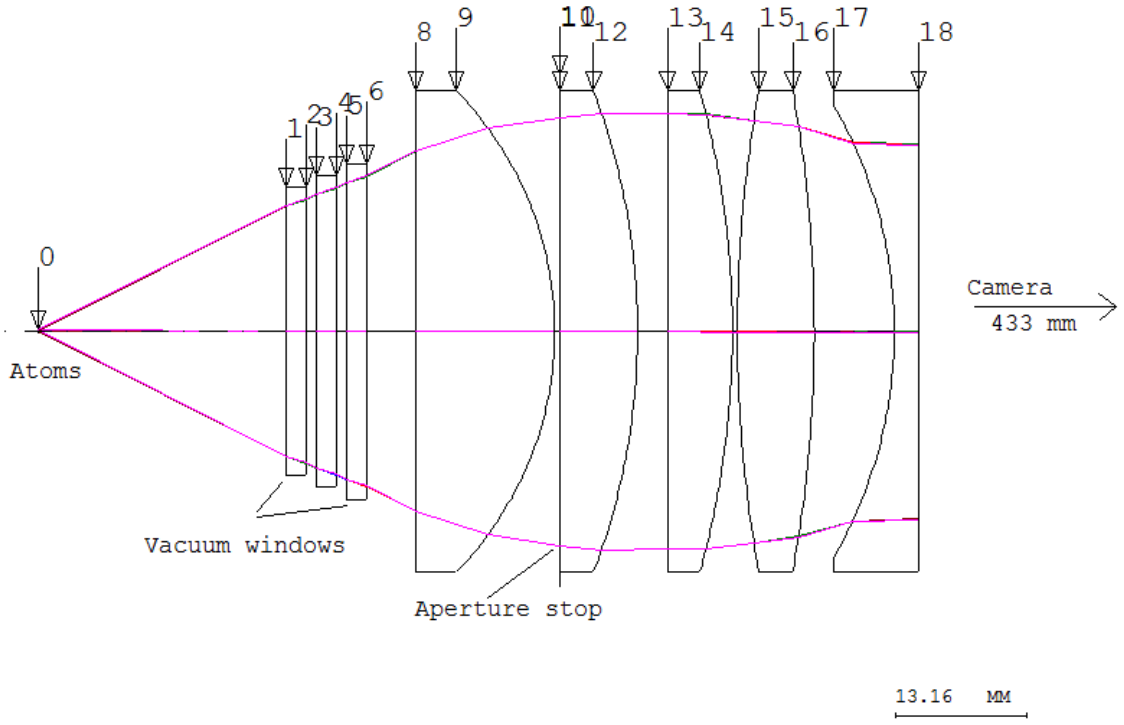

Figure 33: **0.43 NA imaging objective**: Schematic of the imaging objective lenses. The chief and extreme rays are emerging from a point source to simulate an ion, and the three flat slabs immediately to the right of the "atoms" simulate the three layers of glass in the vacuum chamber.

Figure 34 shows the objective in the context of the rest of the imaging system. This figure is from Zemax. (A) is a simulation of the glass from the three layers of glass at the reentrant imaging window underneath the vacuum chamber. (B) is the Photon Gear custom objective. (C) is the intermediate focus of the system, which is used for spatial imaging. Since the desired image is a linear chain of ions, an adjustable slit is placed here and closed so

that the background will be removed [24], and the light from the ions will continue through the imaging system. (D) is a 0.13 NA Thorlabs objective that is used here to minimize the amount of aberration that the second stage of magnification applies. (E) is a lens used to focus the image onto the camera at (F). The focal length of the lens at (E) will determine the magnification of the second imaging stage.

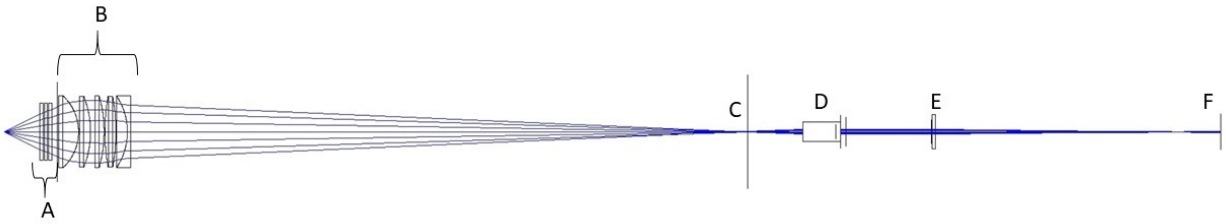

Figure 34: **Imaging system**: Zemax schematic of imaging system. The light is simulated to emerge from a point source on the left. **A**: Glass slabs to stand in place of the 3 layers of reentrant windows. **B**: The lenses in the imaging objective. **C**: Intermediate focus. **D**: 0.13 NA Thorlabs objective. **E**: f=250mm lens. **F**: Focused light onto the camera.

Figure 35 shows the physical layout of the imaging system. The imaging objective and connected mirrors are positioned with a 3-axis translation stage and a tip-tilt stage. (A) and (B) are holders for dichroic beam splitters so a 355nm individual addressing beam can be applied through the objective. While only one dichroic is needed, having a second dichroic at a particular angle to the first one will cancel out optical aberrations along the imaging path[25]. (C) is the adjustable slit for spacial filtering at the intermediate focus. (D) is the 0.13 NA Thorlabs objective [26]. Between (D) and (E) is a flipper box which switches the imaging path between the camera and the PMT. (E) is where the last lens is held before the image is

[24]Using this technique, any scattered light from the object (the ion chain) should continue through the system, and any scattered light from a different location should be cut off.

[25]This can be demonstrated by simulating two dichroic beam splitters in Zemax. This method was implemented in the warm QSim lab and they should be consulted for details on dichroic placement.

[26]This smaller objective was the first objective used to image the ions in this system.

focused onto the camera. Along the PMT path, there is also a last lens to focus the image onto the PMT. The current magnification of the system is X100.

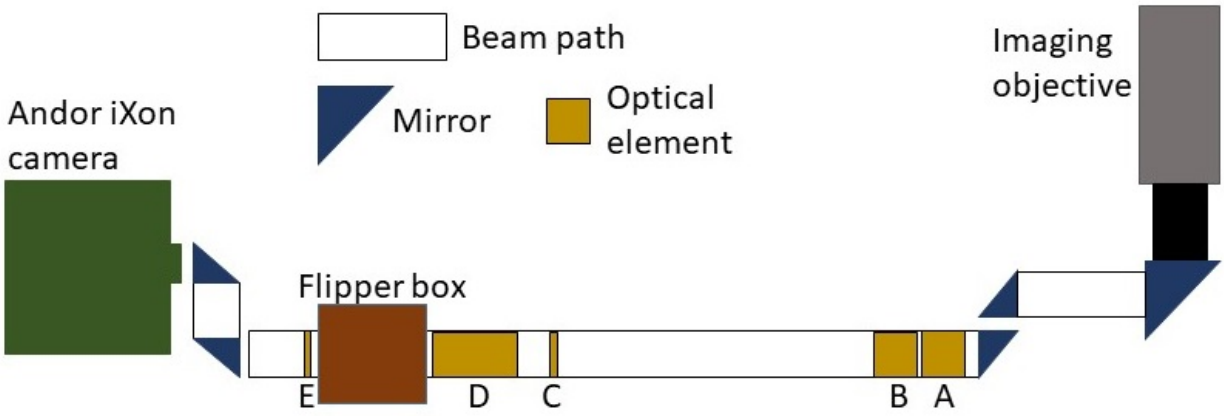

Figure 35: **Imaging system schematic**: The imaging objective directly collects light from the ions and focuses a magnified image onto the camera. The objective collects about 0.45 NA of light from the ions. (More explained in the text)

16.2 State detection

When collecting data, one can read out data using the PMT or the camera. The PMT responds quickly and is ideal for working with one or two ions. Once the individual ion magnetization of a longer chain is needed, the camera is used, though it is slower. In order to find the fluorescence of each ion in an ion chain, individual ROIs (region of interest) must be figured for each ion. This is done by taking an exposure with cooling light so each ion will appear bright. From this camera exposure, the location of each ion is determined.

In this experiment, the ion trap is connected to a long[27] pendulum, contrary to the other Monroe experiments with room-temperature vacuum chambers. This is seen from Figure 8a and results in the ion chain moving around during an experimental scan. The ion chain

[27]...and oddly shaped

will typically move on the order of an ion spacing over the time of a few minutes. This is problematic as an experimental scan can take anywhere from 30 seconds to 2 minutes. This problem was fixed by introducing so-called 'local cooling shots'. Just as cooling light was used before to take a bright ion picture and use it to identify an ROI for each ion, this method is used to take a cooling shot before each experimental time step. For instance, for the Many-Body Dephasing experiment, each experiment scan consisted of 50 time steps with 200 experiments per time step (each time step took an average of 2 seconds). Before a new time step, a cooling shot was takes so the ROI positions could be updated for each time step.

The general data taking process is as follows. Once the system is calibrated (to be explained later) a series of bright and dark shots are taken separately for the chain of N ions. Unlike the cooling shots for figuring the ROIs, the bright and dark shots here are taken with the detection light as would be in an experiment. For each ion, the bright and dark shots are used to create a bi-modal fluorescence distribution, Fig.36. From this, a fluorescence threshold is demarcated to discriminate between a bright and a dark ion. Namely, to distinguish between the $|\uparrow\rangle$ and $|\downarrow\rangle$ state for each ion. Detection cross-talk is detected by taking a large sample of data where each ion is rotated with a $\pi/2$ pulse and then measured. With this, each ion is prepared in the superposition $(|\downarrow\rangle + |\uparrow\rangle)/\sqrt{2}$. Upon measurement, each ion randomly collapses to $|\downarrow\rangle$ or $|\uparrow\rangle$, and when this is averaged over with a large sample, ideally, no two ions should be correlated with each other. Of course, the fluorescence from an ion will bleed over to the ROIs of its neighboring ions. Such detection correlation is minimized before an experiment by adjusting the imaging objective and beam pointing of the detection and optical pumping lasers. The collected data from the camera are a set of pictures of the ion chain. Using the discrimination

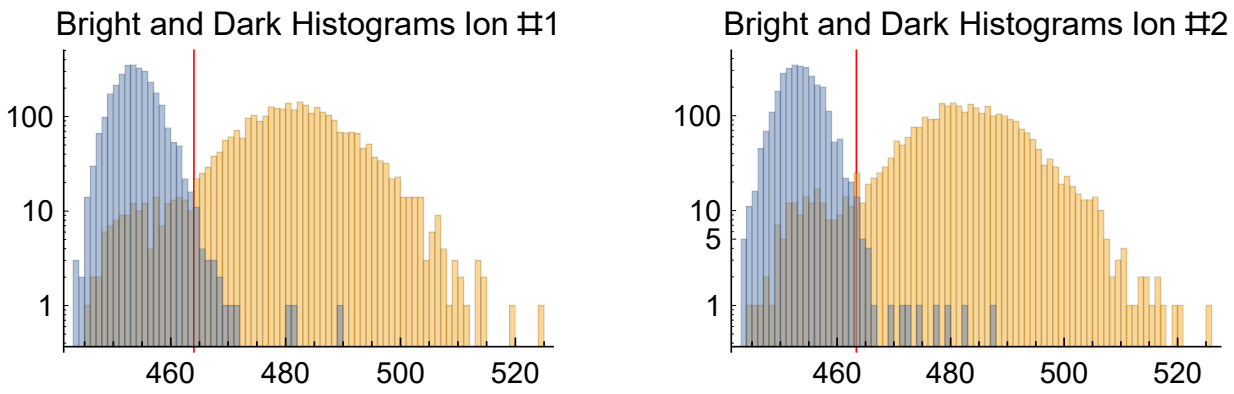

Figure 36: **Histogram of bright and dark calibration shots for 2 ions**: For each of the two ions, the bright and dark counts form a bimodal distribution. The red vertical line represents the detection threshold for discriminating a bright from a dark ion for a single experiment. Both histograms contain 3000 calibration experiments for the bright and dark counts. In this case, the dark and bright fidelity are 99.1% and 94.5% respectively.

threshold and the updated ROI of each ion for each time step, each picture is translated into a binary string. Each string is as long as the ion chain and $0 = |\downarrow\rangle$ and $1 = |\uparrow\rangle$. When in this form, the data can be manipulated and processed in a straight-forward way.

Part IV

Calibrating the apparatus for experiments

This section will be split up into two sections, the former discussing calibration that does not happen on a regular basis, and the latter section describing the daily calibration procedure.

17 Infrequent Calibrations

17.1 Magnetic field aligning

As mentioned in the last section, there are magnetic field coils which create a B-field at the site of the ions. The reason for this field is to separate the Zeeman states of the ${}^2S_{1/2}|F=1\rangle$ triplet. If these states are not separated, then during optical pumping, the ion can be pumped to a coherent dark state resulting from a dark superposition of the $|F=1, m_F=-1\rangle$ and $|F=1, m_F=+1\rangle$ states (22). This can be thought of in the following way. When the Zeeman states are separated by the B field, each of the Zeeman levels occupy a different energy. Therefore the time evolution of a superposition of these states has a relative phase that is continually changing. If the atom decayed into a dark superposition of Zeeman energy levels, it will immediately evolve out of that dark superposition.

The B-field also defines a quantization axis. This is important as it determines which polarizations of light are driving the ions. For instance, when performing spin rotations or the Molmer Sorensen scheme, the π light component of the Raman beams should be minimized. Having a π light component will allow the ion to transition into one of the Zeeman states.

In practice, if the B-field is aligned along the same axis at the counter-propagating Raman beams, then there will be no π polarization components driving the electronic transition. In order to perform a Raman transition, the counterpropagating Raman beams and the B-field need to be in the Lin-Perp-Lin configuration (10). Practically, this means that the polarization of both Raman laser beams must be linear, mutually perpendicular, and both of them must be perpendicular to the B-field.

The process of aligning the B-field with the Raman laser beams, constitutes minimizing the π component of the laser light incident on the ions; thereby minimizing Raman coupling to the Zeeman levels. To experimentally test this, one can directly drive transitions between the states $|\downarrow\rangle$ and $|F = 1, m_F = -1\rangle$ or $|F = 1, m_F = +1\rangle$, and minimize the Rabi flopping. The challenge with this is that when the B-field is adjusted, the resonance frequency with the Zeeman states changes. This necessitates the need to remeasure the resonance after adjusting the B-field.

17.2 Rabi flopping

When performing Raman Rabi flopping, there are two schemes that can be used, the copropagating and non-copropagating schemes. As the name suggests, the copropagating scheme is when the ion absorbs and emits from and into either the same laser beam, or copropagating laser beams. Using these schemes, there is no net momentum kick imparted on the ion chain. There is a net momentum kick when using non-copropagating beams. For driving an electronic transition, no momentum kick is needed, but in order to drive a motional sideband (ie. an electronic transition +/- a phonon of energy) the non-copropagating scheme is needed.

17.2.1 Copropagating scheme

When first performing Raman Rabi flopping, it is wise to start with the copropagating method as it is not sensitive to interferometric instabilities that arise by having two separate beam paths. The Raman laser system is set up so that the AOM is imaged onto the ions. This means that each Raman beam comes to a focus in the AOM and then is focused again onto the ions chain. Since the beam is focused into the AOM, it is as if there is a point source in the AOM. When light from a point source is focused down, it converges to a common point. This means that the AOM can be driven with different frequencies (corresponding to different deflection angles of the outgoing light from the AOM), and each beam path will focus on the ions. In the copropagating scheme, the pulsed laser/frequency comb is focused into an AOM and two different RF tones are used to drive the AOM such that the beat-note between the comb teeth of the two copropagating combs will drive the electronic transitions. Once the copropagating beams are overlapped with the ions (Light Shift method explained in daily calibration section, later), the frequency of one of the two tones can be scanned to look for the resonance. Once a resonance is found, a word of caution is to sweep the driving frequency and search for the resonances for the carrier, $|\downarrow\rangle$ to $|\uparrow\rangle$, as well as the resonance to the Zeeman states. This is so one is sure they are in fact Rabi flopping on the carrier and not mislead from the excitement of having a signal. The copropagating scheme requires that the beam have circular polarization. If the polarization is purely circular, and the B-field is aligned well with the beams, then only the carrier will be excited and not the other Zeeman levels.

17.2.2 Counter-propagating scheme

When preparing to perform the non-copropagating scheme, the main purpose of starting with the copropagating scheme is to measure the carrier frequency. The remainder of this discussion will specifically consider the system at hand which consists of counter-propagating Raman beams. The general non-copropagating scheme can be deduced in a straight forward way from the treatment here.

In the counter-propagating scheme, the single frequency (355nm pulsed laser) comb is split up into two beams. Each beam is focused into an AOM and is imaged onto the ions. As the beams are counter-propagating, each beam travels its own path to the ions. Given that the laser is pulsed, it is necessary to make sure that both paths are the same length, so that two pulses, split from a single pulse, will impinge on the ion chain simultaneously from both sides. The relative path length of both paths is adjustable using a delay stage. In Figure 32 feature (G) depicts the three mirrors on one of the Raman paths on a translation stage that can shorten or lengthen that path.

The coincidence of two pulses on the ion chain is measured in the following way. The 355 pulsed laser scatters off the blades and can be detected on the PMT through the imaging system. With the output signal from the PMT fed into a PicoHarp, one is able to trigger on the first laser pulse that is detected and measure the time delay until the next pulse. The delay stage can be adjusted until the pulses are coincident. Once the pulses are overlapped on the ion location, one can look for Rabi flopping directly using the PMT with the counter-propagating scheme and use this signal to continue to optimize the relative path lengths.

When using the counter-propagating scheme, the polarization of each beam must be linear

and mutually perpendicular with the B-field. This is described in the Lin-Perp-Lin description in the previous section. In order to drive the carrier, or any other transition, both AOMs can be tuned such that the difference between the comb teeth on the counter-propagating combs will drive the desired transition (as described in the appendix).

17.3 Molmer Sorenson scheme

When performing the Molmer Sorenson scheme[28], a red and a blue detuned Raman beat-note are applied simultaneously as pictured in Figure 5. The red and blue dashed lines represent the red and blue detuned Raman beat-notes that off-resonantly couple to the transverse collective sidebands of motion[29] which creates spin-spin interactions as discussed in the appendix. In this system, the AOM in the Raman1 path is used to lock the beat-note as explained in another section. The AOM in the Raman2 path is used to create two frequency combs. When an ion absorbs (emits) from each of these Raman2 combs and emits (absorbs) into the Raman1 comb, a red (blue) detuned tone is created to off resonantly drive the ion chain. Although a red or blue sideband is the result of an absorption and emission event, the two tones on the Raman2 AOM will be called the red and blue frequencies and beams accordingly. Since the red and blue sidebands are off resonant with respect to the carrier transition, they create a Light Shift which shift the carrier and corresponding motional sidebands in opposite directions. The red sideband pushes the carrier to higher frequencies and the blue sidebands to lower frequencies. Because of this, the Light Shift can be balanced by changing the relative strength of the red

[28] As explained later, this is the scheme that creates spin-spin interactions.

[29] Only one set of transverse modes is pictured in Figure 5, but the Raman beat-notes do couple to both sets of transverse modes.

and blue beams. If the red and blue beams are not overlapped well, or if either of them have a non-Gaussian intensity profile, it is possible that there will be a light shift gradient across the ion chain. This can be detected by shuttling one ion to different locations along the chain and performing a Ramsey experiment to detect a net Light shift between the red and blue tones. In order to adjust the Light shift gradient, the position of a cylindrical lens can be adjusted along the Raman2 beam path which is shown in Figure 32 feature (T). This can also be diagnosed by looking directly at the beams. Using the Guppy camera/beam profiler, the focus of the Raman2 beams can be imaged. Each beam can be turned on individually to see if it has a Gaussian profile and if the red and blue beams overlap well. Using the fitting functions on the Guppy beam profiler software, it is fairly easy to see if the beams are overlapped.

17.4 Micromotion nulling

When the ion is trapped, it sits in an RF field that is oscillating at $\sim$ 24MHz. If the ion is precisely at the RF null of the trap, then it will not feel this RF oscillation termed micromotion. This is so if the particle is truly a point particle. The quantum description of an ion's position is a wavefunction spread out in space. Therefore, the ion will always feel the micromotion to some degree (16). There are other sources of micromotion that can not be compensated (15). These result from having imperfections in the construction and placement of the blades or from the RF blades being driven by RF with a phase offset between the two blades. For the rest of this discussion, it will be assumed that there are no flaws in the geometry of the trap. Indeed, the trap used for experiments is quite symmetric and the micromotion can be minimized to a high degree.

Though micromotion can't be eliminated it can be minimized to a high degree. The proper way to do this is to use the procedure outlined in (7). This reference prescribes to look at the fluorescence of a single ion over one trap RF cycle along each axis. This technique was performed along one axis, namely, the axis of the Doppler cooling beam. The fluorescence from the cooling beam was collected on the PMT and fed into the PicoHarp which can scan over time scales on the order of the RF period. If the ion is moving with the micromotion, then the fluorescence signal on the PMT will oscillate along with the RF period.

Practically speaking, the micromotion needs to be nulled whenever the trap parameters are changed. This usually happens when the target number of ions to trap changes. The simple way of nulling the micromotion is to perform Rabi flopping on the micromotion sideband and to move the ion until the flopping is minimized. As with the fluorescence technique mentioned above, this method only minimized micromotion along one direction, namely, along the direction of the Raman beams.

17.5 Measuring trap frequencies

Over the life of this experiment, three traps have been used. For each new trap, there are a number of items that need to be measured and characterized. Most importantly, the trapping frequencies need to be measured. This can be measured either by doing Raman spectroscopy and measuring the motional sidebands, or by modulating one of the trap electrodes. If the Raman beams are well aligned, they should only be able to directly probe one or both of the transverse vibration modes. To directly measure the axial mode, the electrode modulation technique might work best. If only the Raman beams are being used, then the axial trap

frequency can be related to the transverse trap modes using the equation $\omega_x = \sqrt{\omega_{CM} - \omega_{tilt}}$, where ω_{CM} and ω_{tilt} are both from either the $\hat{y}$ or $\hat{z}$ axis.

17.6 Imaging system magnification

The magnification of the objective system is an important value to know, especially when dealing with long chains. After all, it is necessary that the entire ion chain can be imaged onto the camera. As with any optical system, the magnification is the ratio of image size to object size. In this system, the object consists two trapped ions, and the image is on the camera. Therefore, one can use software in order to measure the distance between two ions in units of pixels and then use the pixel size to determine their separation. For the actual separation of the ions, the following method is employed as explained in (8).

If the ion chain is assumed to be trapped in a harmonic potential, then the equilibrium positions of all the ions can be calculated for any length of ion chain. Reference (8) uses a length scale l to convert the actual distance to a dimensionless distance. The relationship between the actual ion equilibrium position, $x_m^{(0)}$, and the scaled position, u_m, of the mth ion in a chain is $u_m^{(0)} = x_m^{(0)}/l$, where

$$l^3 = \frac{Z^2 e^2}{4\pi\epsilon_0 M \nu^2}.$$

Here, Z is the degree of ionization of each ion, e is the electron charge, ϵ_0 is the permitivity of free space, M is the mass of a single ion, and ν is the axial trapping potential.

Using the scaled coordinates, the equilibrium positions are calculated. For two ions, the scaled equilibrium positions are (-0.62996, 0.62996). Multiplying these scaled positions by l gives the real positions and the real ion separation is calculated. Currently, the magnification

is about X100, and a linear chain of 40 ions can fit across the camera.

17.7 Transverse mode calibration

As will be explained in the daily calibration section, the collective transverse motion of the ion chain needs to be characterized to enable an experimental determination of the spin-spin interaction, J_0. In brief, this is performed with one ion in the center of the trap. It was assumed that the transverse frequencies should be the same at all locations across the ion chain (along the trap axis).

It was found that the transverse modes of motion decrease away from the center of the chain. This means that the collective modes of motion are going to be different from the anticipated spectrum of modes from a uniform transverse potential. The transverse modes were measured across the length of the ion chain by shuttling 2 ions to different positions along the chain and measuring the center of mass (CM) and tilt modes for both sets of transverse modes. This measurement was taken and the results are recorded in Figure 37.

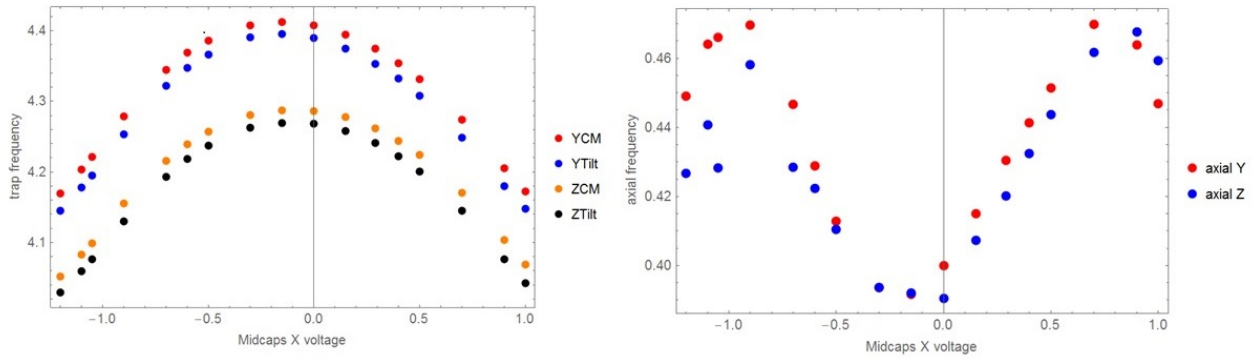

Figure 37: **Collective ion chain modes as a function of position along the ion chain**: The figure at left shows the CM and tilt modes for both transverse axes of motion. To the right are the calculated axial modes from the two sets of transverse modes measured. The variable Midcaps X on the $\hat{x}$ axis represents a voltage that is used to axially shuttle the ion chain.

Here (left), one can see that the CM and tilt modes for both transverse axes decrease away from the center location. To measure this, the ion pair was shuttled using the global control variable 'MidCapsGlobalX'. The measurement of these sidebands were taken with the Raman beams, so the axial modes were not directly probed. For this reason, the axial modes were calculated from each set of transverse modes as follows,

$$\omega_{axial} = \sqrt{\omega_{CM} - \omega_{tilt}}$$

Where ω_{CM} and ω_{tilt} are both along either of the transverse trap axes. The calculations agree fairly well and show that the axial frequency also changes as a function of ion position. Once these frequencies are known, then the spin-spin interaction across the entire chain can be properly characterized.

17.8 Parity scan

The bread and butter of the Monroe lab quantum simulation experiment is the Molmer Sorenson (MS) protocol which creates an effective spin-spin interaction[30]. When first performing a MS scan, it is necessary to test how well the participating spins are getting entangled with each other.

Calibration of the MS interaction is performed with two ions, so the following discussion will consider two spins. In a system where two spins start in the $|\downarrow\downarrow\rangle$ state, if each spin is rotated individually, then the system will evolve in time through the state $\frac{1}{2}(|\downarrow\rangle + |\uparrow\rangle)(|\downarrow\rangle + |\uparrow\rangle)$

[30]Everything we do is Molmer Sorenson, whether it be baked, minced, marinated, sauteed, fried, stir-fried, pan-fried, deep-fried, air-fried, grilled, roasted, steamed, broiled, or burnt.

before reaching $|\uparrow\uparrow\rangle$ and will continue to flop. In the case of an ideal MS scheme, if the system starts in the $|\downarrow\downarrow\rangle$ state, then the system will evolve in time through the $\frac{1}{\sqrt{2}}(|\downarrow\downarrow\rangle + |\uparrow\uparrow\rangle)$ state (which is entangled) before reaching $|\uparrow\uparrow\rangle$ and continuing to flop. The degree to which the system is entangled must be determined. This is done with a parity scan as explained in (9).

The parity scan procedure is as follows. Starting from $|\downarrow\downarrow\rangle$, the spins are evolved under the MS protocol until the state $|\Psi_0\rangle = \frac{1}{\sqrt{2}}(|\downarrow\downarrow\rangle + |\uparrow\uparrow\rangle)$ is reached. Next, using a global rotation (rotating each spin individually), the spins are rotated by $\pi/2$ around the variable axis ϕ in the x-y plane. This rotation takes the state $|\Psi_0\rangle$ to the state

$$\Psi_0(\pi/2) = \frac{\mathrm{i}}{\sqrt{2}}(e^{-\mathrm{i}\phi}\sin\phi|\downarrow\downarrow\rangle + \cos\phi|\downarrow\uparrow\rangle + \cos\phi|\uparrow\downarrow\rangle - e^{\mathrm{i}\phi}\sin\phi|\uparrow\uparrow\rangle).$$

This process is repeated many times to build up statistics.

Finally, the populations $P_{|\downarrow\downarrow\rangle}$, $P_{|\downarrow\uparrow\rangle}$, $P_{|\uparrow\downarrow\rangle}$, and $P_{|\uparrow\uparrow\rangle}$ are measured and used to make the parity observable

$$\Pi = P_{|\uparrow\uparrow\rangle} + P_{|\downarrow\downarrow\rangle} - P_{|\uparrow\downarrow\rangle} - P_{|\downarrow\uparrow\rangle} = 2\left(\frac{1}{2}\sin\phi^2\right) - 2\left(\frac{1}{2}\cos\phi^2\right) = -\cos(2\phi).$$

The equation shows that a parity curve should take on the shape of the function $-\cos 2\phi$ dependent on the rotation axis ϕ.

If the fidelity (which is the contrast of the parity curve) is greater than 50%, then it is known that entanglement is being produced. With two spins, the parity curve can also be collected from the PMT as shown in Figure 39.

With two spins, there are three fluorescence levels that are easy to discriminate. Namely,

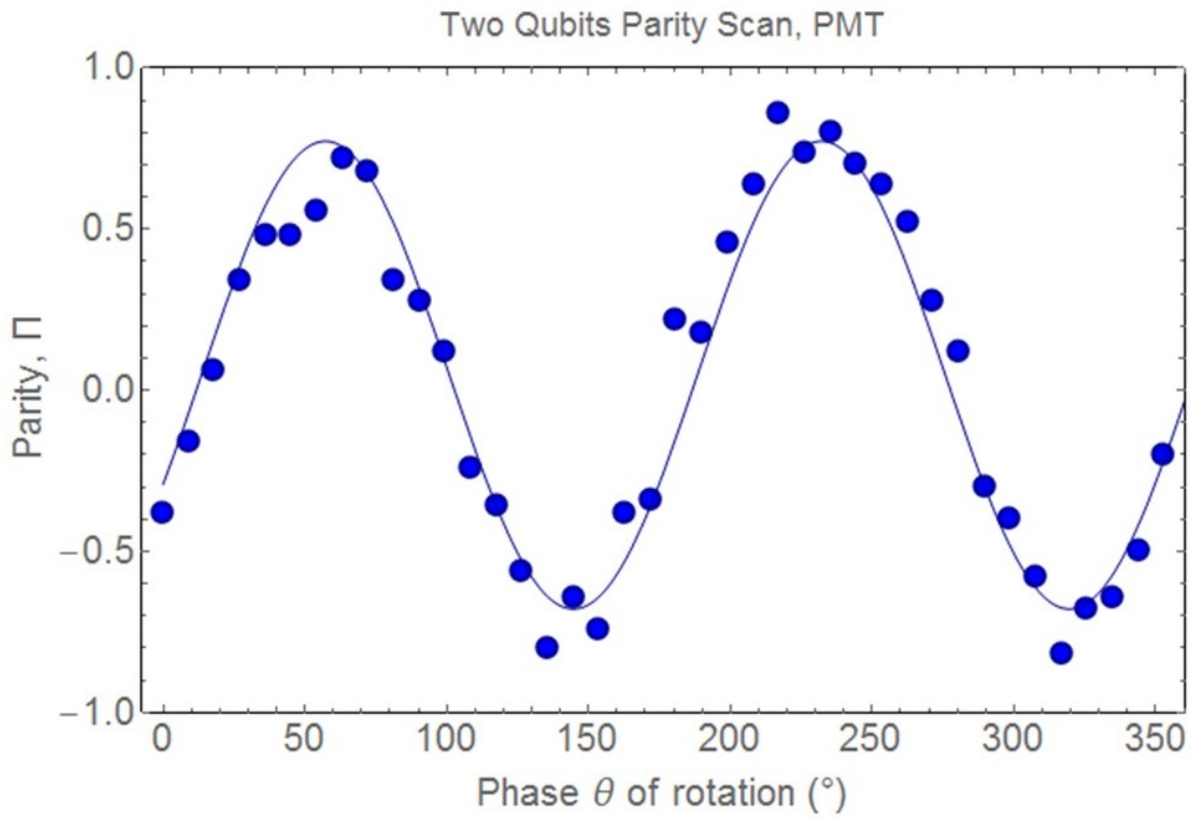

Figure 38: **2 spin Parity Scan with 85% fidelity**: This parity scan was taken on July, 3 2018. The fidelity was measured at 85% which is the best parity fidelity measured in this lab.

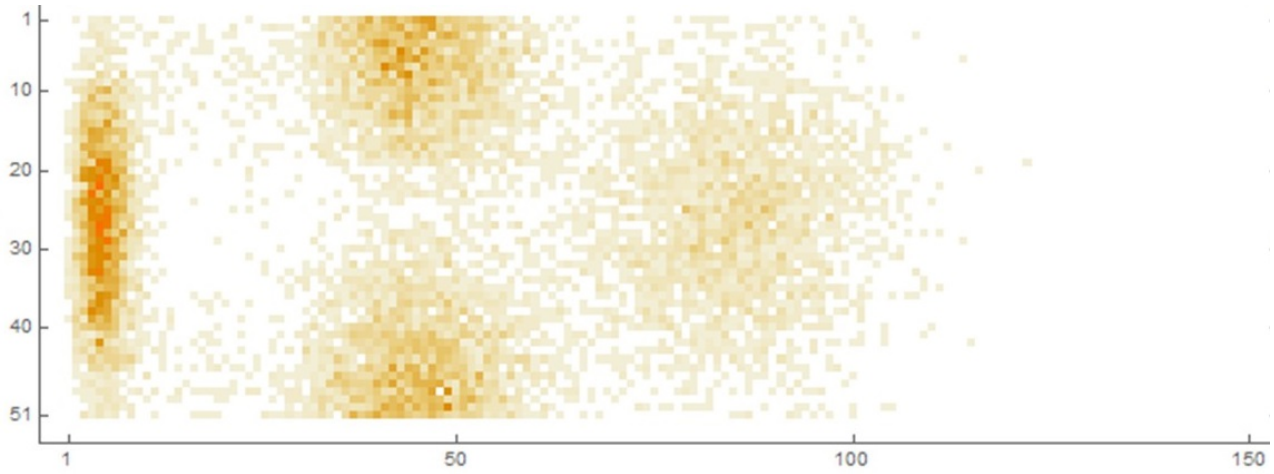

Figure 39: **2 spin Parity Scan measured on the PMT**: This parity scan was taken on June, 5 2018. The horizontal axis displays the fluorescence histogram, and the vertical axis shows the 50 steps taken to scan the $\pi/2$ rotation axis ϕ from 0 to 180°.

the fluorescence levels with both spins down, one spin up, and both spins up. When starting in $|\downarrow\downarrow\rangle$ and evolving under MS, the only fluorescence levels measured should be those with both spins down and both spins up. Using the PMT to collect fluorescence, the counts collected during a time step can be binned in a histogram to show oscillations between the $|\downarrow\downarrow\rangle$ and $|\uparrow\uparrow\rangle$ fluorescence levels. When doing a full parity scan with two spins (including the $\pi/2$ rotation following the MS scan), the fluorescence levels can be binned in a histogram as in Figure 39.

17.9 Molmer Sorenson tuning

In principle, when performing a MS scan on two spins, the detection contrast of the magnetization of the system is expected be full. In practice, the MS scans performed will have maximum contrast anywhere between 40% to 90% of the full detection contrast. In order to try to improve the quality of the MS scan, the following procedure was tested. As will be explained in the daily calibration section, part of the calibration procedure consists of measuring the Rabi flopping frequency of the red and blue detuned beat-notes with 2 ions. While these beat-notes drive the motional sidebans off-resonantly during the MS scan, the Rabi frequencies on these motional sidebands are needed for the calculation of J_0. Implicit in the MS calculation is the assumption that the Rabi rate of the red and blue CM motional sidebands are the same. This is in the derivation on page 54 of the Islam thesis (10). Explicit in the calibration for a MS scan in this aparatus is that the red and blue CM sideband Rabi frequencies are not the same; they can be around 10% off from each other. That said, a new method was tested in order to balance the red and blue Rabi frequencies of the CM mode. The intensity of the red and

blue frequency combs can not simply be adjusted to balance the Rabi flopping because the power in these two beams are already tuned to null the differential Light shift between the red and blue Raman beat-notes. The solution to this is to add another tone to one of the Raman AOMs (Raman2 AOM), which will create a beat-note farther off resonant from the motional modes than the red and blue tones. This third tone will help to balance the Light shift so that the power of the red and blue combs can be adjusted to have the same Rabi frequency, Fig.40. This scheme did work to balance the Light shift while having the red and blue Rabi

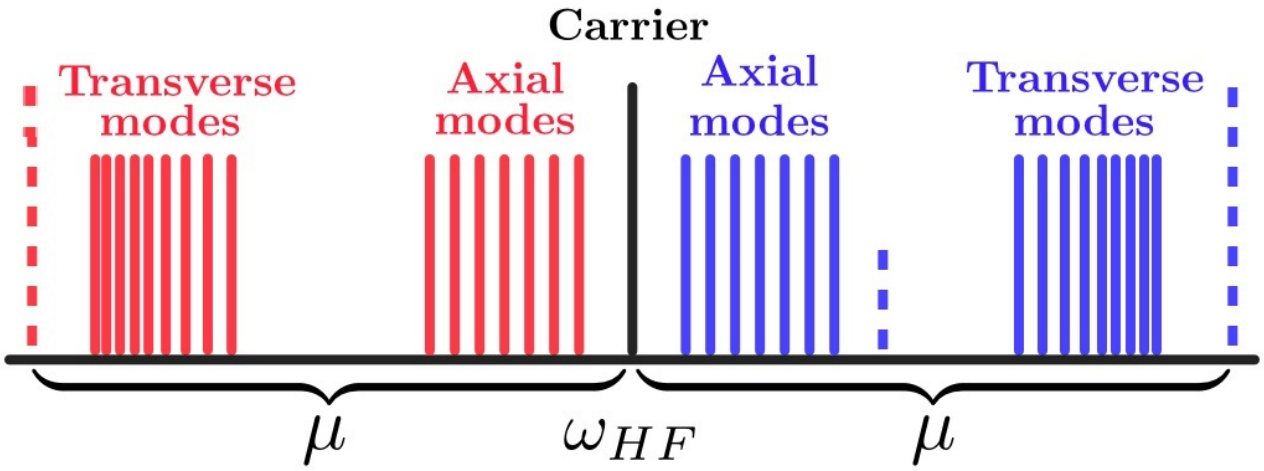

Figure 40: **Alternative MS calibration scheme**: In order to allow for the red and blue Raman beat-notes to induce the same sideband Rabi flopping, another beat-note is needed. The extra beat-note was added on the blue side and is represented by the shorter blue dotted line in the figure. Though the figure is not to scale, this third beat-note does not excite the axial modes and is detuned farther from the transverse modes than the full power red and blue beat-notes. The amplitude of the third beat-note is adjusted so that the net Light shift of the carrier frequency is zero.

flopping at the same rate, but this did not help to improve the MS scan. It did not hurt it either, the performance with and without this technique were nearly identical.

17.10 Coherence time

Decoherence is the limiting factor that prevents simulation experiments from extending beyond 1 or 2 milliseconds. In clock experiments using $^{171}Yb^{+}$, the coherence time[31] was measured to be more than 15 minutes (18) (39) (40). Other experiments, report the coherence time[32] to be on the order of a few milliseconds, which is also the case in this experiment. This means that the decoherence is limited by the performance of the supporting infrastructure. This includes the stability of the trap frequency, the pointing of the laser beams, and the vibrations from the cryostat. The transverse normal modes are used for the MS scheme because they are faster than using the lower frequency axial modes, but they are less stable. The transverse modes can drift by around 0.1%.

The pointing noise of the laser beams and noise from the cryostat are the main culprits of decoherence. Performing a Ramsey experiment on the carrier, the coherence time is measured to be around 5-10 ms. When doing a similar Ramsey experiment while driving on the red or blue motional sideband, the coherence time is around 1-2 ms. This shows that there is noise in the laser beams and in the trap RF (which determines the transverse trap frequencies).

17.11 Cryostat transport and vacuum procedures

Along with using a cryogenic vacuum chamber comes the benefit of being able to pump to low pressures without baking the vacuum chamber, as well as the luxury of not needing to be as careful with vacuum cleanliness during fabrication and assembly. In this section, the detailed process of moving the cryostat and vacuum chamber and opening and closing it will not be

[31] This is t_2 because echo pulses were used.
[32] t_2^*

discussed, but general ideas and important points will be discussed. Since the natural habitat for the cryostat is on the experiment optics table, this discussion will start with heating and moving the vacuum chamber from its position in the experiment.

17.11.1 Heating up the cryostat

Heating up the vacuum chamber refers to heating it up from cryogenic temperatures to room temperature. This is quite easy as it involves turning off the cryostat, but there are some points to note. There is a heater built into the cryostat near the 4K stage, and other external heating elements such as the reentrant window heater, the RF power, the pressure gauge, and the B-field coils. Typically, the 4K heater is used to hasten the heating process. The roughing/turbo pump is connected to the vacuum and is used to pump down the chamber while heating. This makes the pressure more controlled during the heating process and also prevents the possibility of over pressuring the vacuum chamber. The chamber can be under vacuum for one year or longer. During this time, if gas is seeping in from the outside and getting cryo-pumped, then during heating, it is possible that the volume of gas released into the chamber will make it over-pressured at room temperature. During the heating (and cooling) process, the resonance of the resonator-trap system is monitored with a vector analyzer as shown in Figure 61.

17.11.2 Moving the cryostat

As mentioned before, the cryostat comes in two parts that are not rigidly attached to each other. Namely, the vacuum chamber and the Gifford McMahon cryo-cooler. These two parts

are connected using 8 stand-offs before moving the entire unit as one. Running above the cryostat and out toward the control station is an I-beam with a trolley attached. The trolley has a chain hoist on it which is used to hoist the cryostat up above the surrounding sea of optics and out toward the control station. The cryostat is then placed in the service station, Fig.41. The service station is designed to allow the vacuum to be opened up and worked on. To put the system back, the vacuum chamber is closed, hoisted up using the pulley system, and lowered into place on the optics table.

Figure 41: **Service station:** When the cryostat is removed from the experiment, it is placed in this 'service station'. Here, the vacuum cover and the radiation shields can be removed so work can be performed on the in-vacuum apparatus.

17.11.3 Cooling down the cryostat

During the cool-down there is an entire process that will not be explained here but is written in the lab logs. This process outlines when the various pumps are turned on in relation to when the cryostat is turned on. This is an art that must be learnt through experience[33].

Figure 42: **Copper gaskets used to seal the 8" vacuum flange**: This collection of copper gaskets represents the number of times that the vacuum was opened and closed in the process of tuning the in-vacuum resonator, and make improvements inside the vacuum.

A typical cool-down is plotted in Figure43. Though the temperatures become cryogenic in

[33]Since the resonator is in vacuum, the resonator coupling could only be tuned by heating up and opening up the apparatus. Though the system has relatively fast turn around time since no bake is needed, this proves to be a very tedious process, where every iteration was very precious.

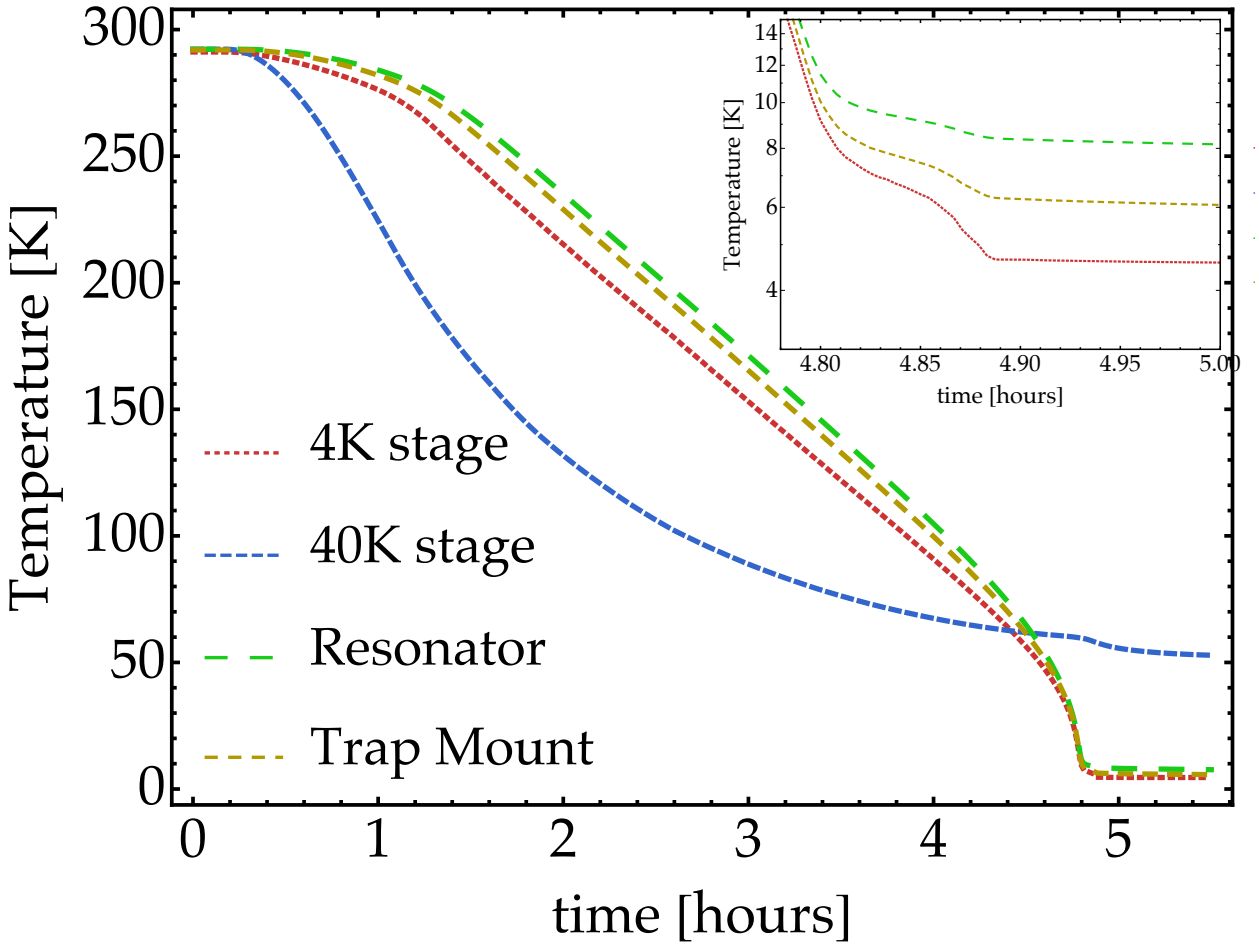

Figure 43: **Cryostat temperatures over time during a cool-down**: The initial cool down takes 5 hours, but the system as a whole takes about one day to completely settle down. The acceleration at the end of the cool-down is due to the steep decrease in the specific heat capacity of copper below 100 K (13).

about 5 hours, the entire system takes about one day to equilibrate, and the pressure takes about one week before the incremental pressure decreases are not noticeable. For instance, it will take about one day for the resonator-trap RF resonance to settle down and stabilize to one resonance frequency.

17.11.4 Pressure maintenance

Interestingly, when under vacuum for a very long time, the collision rate with the trapped ions can increase. Before March 2019, ion chain lifetimes were decreasing. By early March 2019, a chain of 10-20 ions would last between 10 to 30 minutes. This was during the time of taking data for the Confinement experiment and it was making it very difficult to collect good data considering the required calibrations before data collection. This problem was fixed by heating up the cryostat and cooling back down.

18 Daily Calibrations

On a daily basis, before performing an experiment, the following calibrations are typically performed. From day to day, certain aspects of the experiment are fairly stable while others are expected to drift[34].

18.1 Ion state detection contrast

The detection of the ions is heavily dependent on the power of the detection and optical pumping beams. On a daily basis, the fiber coupler that both detection and optical pumping beams travel through will get misaligned, and likely the beam pointing needs to be adjusted. The sequence of steps for a bright detection scan is: Doppler cool $\Rightarrow$ Optical pump $\Rightarrow$ $\pi/2$ pulse $\Rightarrow$ measure(detection). If a detection step is added right after the optical pumping step, then one can see two simultaneous traces coming from the PMT of the full detection contrast. One trace shows the dark state and the other shows the bright state fluorescence levels. This scan can be used as a signal to maximize the detection contrast.

For one ion, a contrast of 35-40 kilo-counts is a good value. When performing a frequency scan in order to look for a resonance, it is not uncommon to measure a false positive. One method to test this is to perform the scan twice. Once in the 'start-to-stop' scan option (on the Sandia experimental control program) and once using the 'center-out' option. Using 'center-out' one can see if the resonance features are symmetric with the center point of the scan. If so, then the peaks are artifacts in the detection light. In this case, the 'start-to-stop'

[34]The alignment of the laser systems are strongly dependent on the stability of temperature and humidity in the lab.

scan acts as a crosscheck.

18.2 Raman beam alignment

The Molmer Sorenson scheme and single spin manipulations use counter-propagating Raman beams. This necessitates that each beam be centered on the ion chain and overlapped with the other beam. Given that the beams have a regular Gaussian profile horizontally and vertically, the individual beam Light shift is used to achieve this alignment.

18.2.1 Alignment with a single ion

The idea is that if each of the two beams are centered on a single ion, then they should both be overlapped with each other. This is performed using the 4^{th} order Light shift from an individual beam (14). Since a Raman scheme is used, it turns out that the differential 2^{nd} order Light shift from the two states $|\uparrow\rangle$ and $|\downarrow\rangle$ is negligible. However, the 4^{th} order Light shift is significant and can shift the carrier transition by about 5 kHz. To perform this calibration, the polarization of both beams is adjusted to be circular and a Ramsey experiment is performed to look for the Light shifted carrier frequency. The Ramsey experiment sequence is: Doppler cooling $\Rightarrow$ Optical pumping $\Rightarrow$ $\pi/2$ Microwave pulse $\Rightarrow$ Time scan with one Raman beam on $\Rightarrow$ $\pi/2$ Microwave pulse $\Rightarrow$ Measure (detection). Using this, the Light shifted carrier frequency produces oscillations. By performing a step-in-place experiment scan on the slope of the oscillation, the Light shift can be increased by adjusting the pointing of the beam.

18.2.2 Alignment with an ion chain

When working with a longer ion chain, it is important to determine that the beam is centered over the length of the chain. When checking the Light shift with an individual ion, the ion can be shuttled to the extremes of the chain to see if the Light shifted Ramsey signal is symmetric about the center of the chain. This can also be performed by trapping a long chain and measuring the Light shifted Ramsey signal on each ion to see if it is symmetric. If this does not work, as is sometimes the case, the beam profile can be directly checked with the Guppy camera beam profiler. If the beams are not Gaussian, then the problem could likely be poor transmission of the Raman beams through the Raman AOMs, or other beam deformities such as clipping. Here, the goal is to determine that the interaction between each the laser beam and the ion chain is symmetrical about the center. Similarly to the method described above, one can shuttle around a single ion and see that the Rabi flopping is symmetrical. This is a two beam effect, so the individual beam position is not determined from this, but the relevant effect is the Rabi flopping.

18.3 Sideband-cooling calibration

When working with a long chain of ions, it is necessary to perform sideband cooling in order to remove phonons from the collective modes of motion. The location of the sidebands are determined by performing a frequency scan over the sidebands with the power level that will be used during the sideband cooling process, Fig.44. This is necessary, because the location of the sidebands is light-shifted by the intensity of the driving laser which makes their location intensity-dependent.

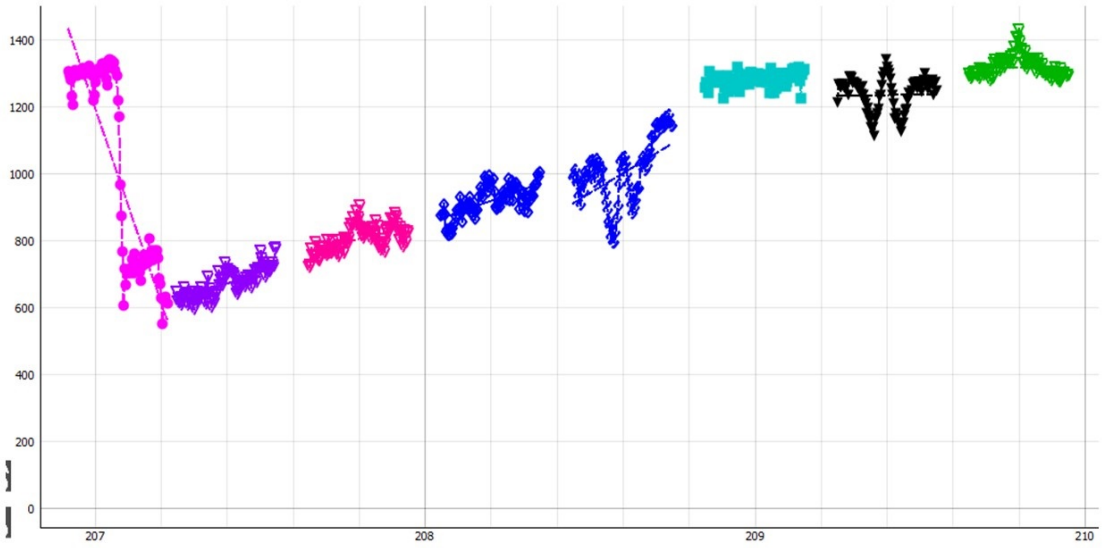

Figure 44: **Red sideband scan with 31 ions**: Using full power (that is used for sideband cooling), the red sidebands were measured, so sideband cooling frequencies can be determined. The x-axis is frequency in MHz, and the y-axis is fluorescence detected on the PMT in units of kilo-counts. Data taken on April, 23 2019.

Figure 44 shows the red sidebands measured for a collection of 31 ions[35]. Clearly, individual peaks are not resolved, rather they blend together. This means, that even if the sideband cooling frequency is not precisely centered on a particular sideband, it should still be able to cool the neighboring transverse modes. The most important modes to cool are the CM modes. This is because the CM modes are the most susceptible to getting heated. An intuitive way to think about this is to consider that if there is a disturbance in the trapping potential that is going to heat up the chain, the disturbance will heat only the modes which it is able to particularly excite. More precisely, if a perturbation in the trapping potential disturbs the ion chain, various modes of motion will be excited based on how the perturbation drives each of the modes, just like a driving waveform that can excite frequencies in a system that are

[35]This is performed using Raman spectroscopy with the full amount of power used during sideband cooling.

in the Fourier decomposition of the original waveform. For this reason, the CM mode is the easiest to drive and the higher order modes, having a more complicated pattern of motion (eigenvector), are more difficult to drive. Nevertheless, if there is a transverse mode of motion that is close to the carrier frequency, then there is a concern that a carrier rotation will excite phonons in these close-by modes. An ion chain will start becoming zig-zag when the transverse confining potential is too weak compared to the axial potential to keep the ions in a linear chain. When this happens, the highest order transverse vibrational mode (lowest mode frequency), approaches zero frequency; this sideband of motion becomes degenerate with the carrier frequency. The ions will sit in a linear chain if the inequality

$$\frac{\omega_{y,z}}{\omega_x} > 0.77 \frac{N}{\sqrt{\log N}}$$

is true. Because there are two non-degenerate transverse confining frequencies, $\omega_{y,z}$, the lower frequency transverse axis should be considered. For this reason, when working with long ion chains, it is common practice in the lab to put one or two sideband cooling frequencies at modes which are close to the carrier to mitigate heating.

18.4 Rabi flopping signal

Frequently, one will center the Raman beams onto the ion chain using the Light shift, but small adjustment will still be required. In such a case, the carrier Rabi flopping signal can be directly maximized by performing a step-in-place scan on one of the slopes of the Rabi flopping curve. The beam pointing can be adjusted with the adjustment lenses just as during the Light

shift optimization. If the Rabi flopping frequency does not improve, then the following might need to be checked: micromotion, Light shift, beam transmission through the Raman AOMs and vacuum chamber, and the power balance between both Raman beams. All of these items have been explained except for the last point which will be explained here.

Even though both beams have a different intensity of light incident on the ion chain, the greatest Rabi flopping frequency is achieved when the power in both beams is balanced. Equation 27 shows the effective Hamiltonian for a 2-level system. The coupling between the two states is $\Omega_1^*\Omega_2$ where $\Omega = -\langle\downarrow|d|\uparrow\rangle E_0$, and d is the dipole operator along the direction of the polarization of the driving laser field (22). Since E_{0i} is proportional to $\sqrt{I_i}$, where I_i is the light intensity of the i^{th} Raman beam, the Rabi flopping frequency is proportional to $\sqrt{I_1 \times I_2}$. The Rabi frequency is maximized when $\sqrt{I_1 \times I_2}$ is maximized which is when $I_1 = I_2$.

18.5 Molmer Sorensen calibrations

The following steps are needed for calibrating the MS scan, so they are all included in one section and are performed each day when an experiment is being performed.

18.5.1 Sideband measurement

With a single ion, the frequency of the red and blue transverse motional sidebands are measured. The goal is to measure these sidebands with no Light shift, therefore, the power of the probe is turned down to 5% of its full value.

18.5.2 Balancing light-shift

With the red and blue sidebands at full power, the differential Light shift is balanced to zero. This is done using a Ramsey experiment. Between two $\pi/2$ pulses, the red and blue detuned beat-notes are turned on for a varying amount of time. If the net Light shift is zero, then the signal will be flat, if not, an oscillation will be measured.

18.5.3 Measuring $\eta\Omega$

Using the red and blue sideband locations previously measured at low power, Rabi flopping is performed on these sidebands with full power. Since the red and blue detuned beat-notes were just balanced (net zero Light shift), these resonances to not get shifted during this measurement. Measuring the Rabi frequency on the red and blue sidebands is directly needed to calculate the MS interaction.

18.5.4 MS adjustments

The next step is to load a second ion into the trap and measure the frequency of the tilt mode along the Y axis (this frequency lies between the two CM frequencies measured with one ion). Assuming a harmonic axial trapping potential, the CM modes and this tilt mode are needed to calculate the frequencies of all the sidebands on the chain. These frequencies are needed to calculate the spin-spin coupling matrix.

At this point, the MS scan is performed with two ions. The detection contrast and frequency of the MS scan are used to determine its quality. The detection contrast is compared to a Rabi flopping scan, and the frequency of the MS curve is compared to theory. The knobs

that are used to adjust the quality of the MS scan are the red/blue intensity balance and the placement of the red and blue sidebands. The red/blue intensity balance is simply the ratio between the intensity of the red and blue detuned tones. This effectively adjusts the differential Light shift; perhaps it changed or was not calibrated correctly in the first place. The latter knob is an offset of the red and blue detuned beat-notes in the same direction. This changes their symmetrical placement about the carrier. If the carrier was measured incorrectly, this adjustment will bring the sidebands to sit symmetrically on either side of the carrier. Adjusting either of these knobs is effectively adjusting an effective B-field in the Z direction to be zero.

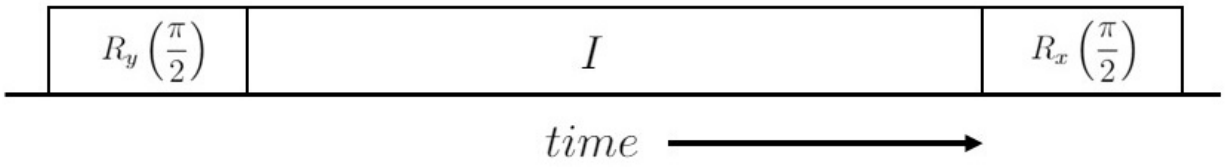

Figure 45: **Ramsey sequence to balance the strength of the red and blue Raman beat-notes**: The Ramsey experiment starts and ends with $\pi/2$ rotations that differ by a phase of $\pi/2$. During the interrogation time, I, both the red and blue beat-notes are on. If there is a net Light shift between the red and blue beams, then there is an effective B-field in the $\hat{z}$ direction. If there is rotation around $\hat{z}$ from the net Light shift, then the fluorescence signal will oscillate. If the net Light shift is zero, the fluorescence signal will be flat at 50% contrast.

18.5.5 Balancing light-shift with a spin chain

Over time, the differential Light shift from the red/blue detuned beat-notes will noticeably shift around and must be calibrated frequently. This becomes impractical if the calibration must be carried out with one or two ions as the goal is to do experiments with long ion chains. Here is a method for balancing the red and blue Light shift with a long ion chain. This method utilizes a Ramsey experiment where the initial and final $\pi/2$ pulses have a relative $\pi/2$ phase

between them. The initial pulse rotates the spins into the $\hat{x}$ direction of the Bloch sphere so the spins are aligned with the spin-spin interaction from the MS interaction. This places the spins into an eigenstate of the MS interaction. If there is no effective B-field along Z, then after the final $\pi/2$ pulse, the magnetization of the spins gives a signal at 50% contrast. Accordingly, if there is a net B-field along Z, then oscillations are measured. The red/blue balance can be adjusted until the oscillations are minimized.

Part V

Many-body dephasing in a trapped ion quantum simulator

The thermodynamic and statistical mechanical behaviour of a closed many-body spin system is of fundamental importance. Most commonly, this problem is investigated by studying the time evolution of the expectation value of a local observable, e.g., particle density and magnetization, after quenching the system from an initial out-of-equilibrium state. For a generic nonintegrable system in the thermodynamic limit, the expectation value tends to relax to a constant value which can be described by a thermal state at some temperature depending on the initial state. However, if the system size is finite, there exists persistent temporal fluctuations around the constant average value as sketched by Fig. 46. Studying these temporal fluctuations represent the next level of the description of quench dynamics than merely looking at long-time observable averages.

A crucial question for statistical physics is how temporal fluctuations are suppressed for increasing system size N. In the case of integrable systems, it has been found that the variance of temporal fluctuations scales as $1/N$ or as polynomial of N [36]. In the case of generic nonintergrable systems, the temopral fluctuations are exponentially suppressed by the system size. In reference (1), by providing an exact analytical result for the exponential scaling of fluctuations with N spins in a weakly nonintegrable sysyem, the authors identified a general dynamical

[36] Depending on which integrable regime the system is in; as will be discussed later.

regime which they term "many-particle depahsing" or "many-body dephasing". In the thermalization process, the dephasing mechanism comes from the relaxation of the quasiparticle distribution to thermal equilibrium by quasiparticle scattering described by the Boltzmann equation. However, many-body dephasing results from the lift of exponentially large degeneracies of transition energies in integrable systems while the quasiparticle distribution remains practically unchanged.

Nevertheless, the exponential size scaling due to many-body dephasing in nonintegrable systems has not yet been verified experimentally. Here, an experimental observation of persistent temporal fluctuations after a quantum quench with a long-range interacting transverse-field Ising Hamiltonian is presented. The temporal fluctuations in the average magnetization are measured for a finite-size system of spin-1/2 particles, which presents a direct measurement of relaxation dynamics in a non-integrable system. After including the experimental noise in the data analysis, the temporal fluctuations from experimental data are consistent with numerical simulations and theoretical analysis.

The Hamiltonian used in this experiment is the long-range transverse-field Ising model,

$$H = \sum_{i<j} J_{ij}\sigma_i^x\sigma_j^x + \frac{1}{2}B\sum_i \sigma_i^z, \tag{19}$$

with tunable, long-range coupling that falls off approximately as power-law $J_{ij} \approx J_0/|i-j|^\alpha$.

Experiments are initiated with the spin chain initialized in the $|\downarrow\downarrow ... \downarrow\rangle_z$ state, a quench is then performed with Hamiltonian 19, and the magnetization along $\hat{z}$ is measured as a function of time after the start of the quench. The spin-spin coupling is antiferromagnetic, $J_0 > 0$, and

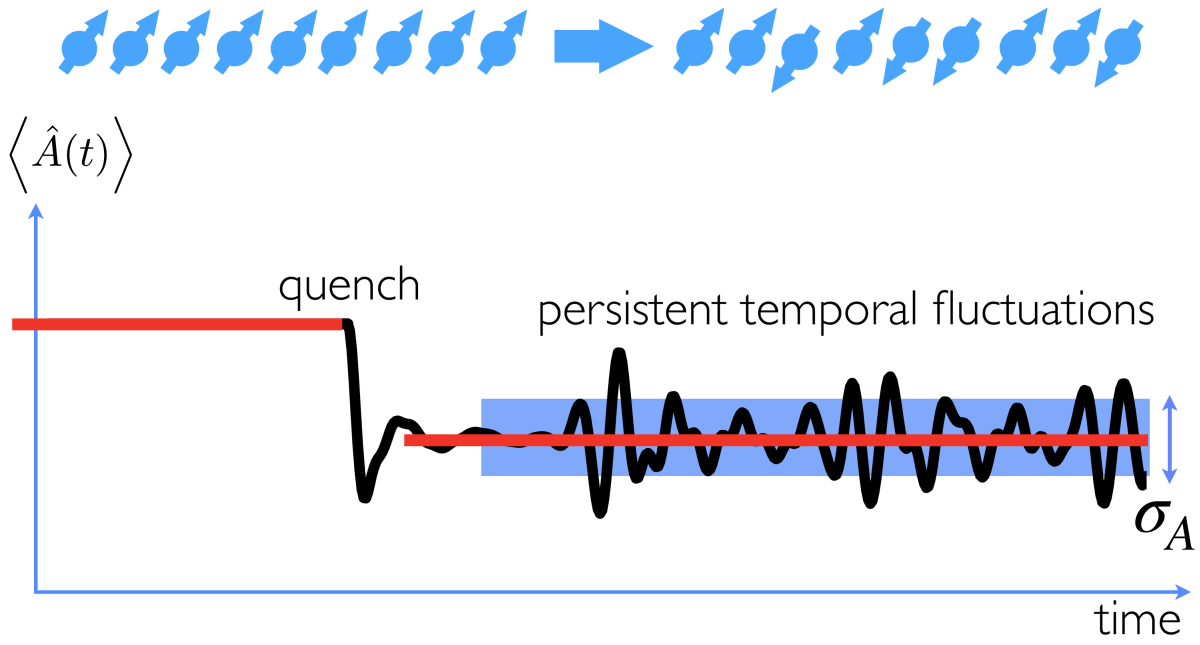

Figure 46: Schematic behaviour of an observable after a quench, in a finite-size system.

the power-law exponent α in general can be tuned between 0 and 3. The cases of $1/\alpha = 0$ and $\alpha = 0$ correspond to two integrable limits, i.e., the nearest neighbor coupling and global coupling models respectively. For a finite $\alpha > 0$, the above Hamiltonian is nonintegrable in general.

In the present experiment, the observable is the magnetization, $\hat{A} = \frac{1}{N}\sum_j \sigma_j^z$. The temporal average is calculated as $\overline{\langle \hat{A}(t) \rangle} \equiv T^{-1}\int_{t_i}^{t_i+T} \langle \hat{A}(t) \rangle dt$ where T is the length of the time window for processing data. The variance of temporal fluctuations of $\langle \hat{A}(t) \rangle$ is defined via $\sigma_A^2 \equiv \overline{\left(\langle \hat{A}(t) \rangle - \overline{\langle \hat{A}(t) \rangle}\right)^2}$ with σ_A the standard deviation. $|\Phi_n\rangle$ is used to represent the many-body eigenstates of Hamiltonian (19) with eigenenergy E_n ($n = 1, 2, \cdots, 2^N$). Given the initial state $|\psi(0)\rangle$, the time evolution of $\langle A(t) \rangle$ is described by

$$\langle A(t) \rangle = \sum_{m,n} \langle \psi(0)|\Phi_m\rangle\langle\Phi_m|A|\Phi_n\rangle\langle\Phi_n|\psi(0)\rangle e^{i\Delta_{mn}t},$$

where $\Delta_{mn} \equiv E_m - E_n$ is the transition energy between the two energy levels m and n. In the long time window limit ($T \to +\infty$),

$$\overline{\langle A(t)\rangle} = \sum_{m,n,\Delta_{mn}=0} \langle\psi(0)|\Phi_m\rangle\langle\Phi_m|A|\Phi_n\rangle\langle\Phi_n|\psi(0)\rangle$$

and

$$\sigma_A^2 = \sum_{\Delta\neq 0} \Big| \sum_{\Delta_{mn}=\Delta} \langle\psi(0)|\Phi_m\rangle\langle\Phi_m|A|\Phi_n\rangle\langle\Phi_n|\psi(0)\rangle \Big|^2$$

with Δ denoting the set of all possible Δ_{mn}. For the integrable models ($\alpha = 0$ and $1/\alpha = 0$), there are exponentially large degeneracies for a given transition energy Δ_{mn}, and for a generic nonintegrable model, the energy transitions are nondegenerate. It is assumed that all the degeneracies of transition energies are lifted, making it so $\Delta_{mn} = 0$ is only possible for $m = n$. As a result, the variance of time fluctuations of a nonintegrable Hamiltonian is given by

$$\sigma_A^2 = \sum_{m\neq n} \Big|\langle\psi(0)|\Phi_m\rangle\langle\Phi_m|A|\Phi_n\rangle\langle\Phi_n|\psi(0)\rangle\Big|^2. \tag{20}$$

In Fig. 47(a), the fluctuation σ_A is plotted as a function of exponent α at fixed λ parameters for $N = 7$ spins. The size scaling exponent κ is extracted from fitting with $\sigma_A \propto e^{-\kappa N}$ and is plotted as a function of α in Fig. 47(b). In both figures, there are two distinct regimes separated by the critical value α_c which depends on the dimensionless parameter $\lambda \equiv 2J_0/B$. This results from the competition of the two terms in Hamiltonian (19), i.e., the magnetic field energy $B\sum_i \frac{1}{2}\sigma_i^z$ and the interaction energy from next-nearest-neighbor (NNN) coupling $2^{-\alpha}J_0\sum_i \sigma_i^x\sigma_{i+2}^x$ [37]. The critical value α_c can be estimated by comparing these two terms,

[37] Of course there are longer range interactions, but only the NNN interactions are considered here.

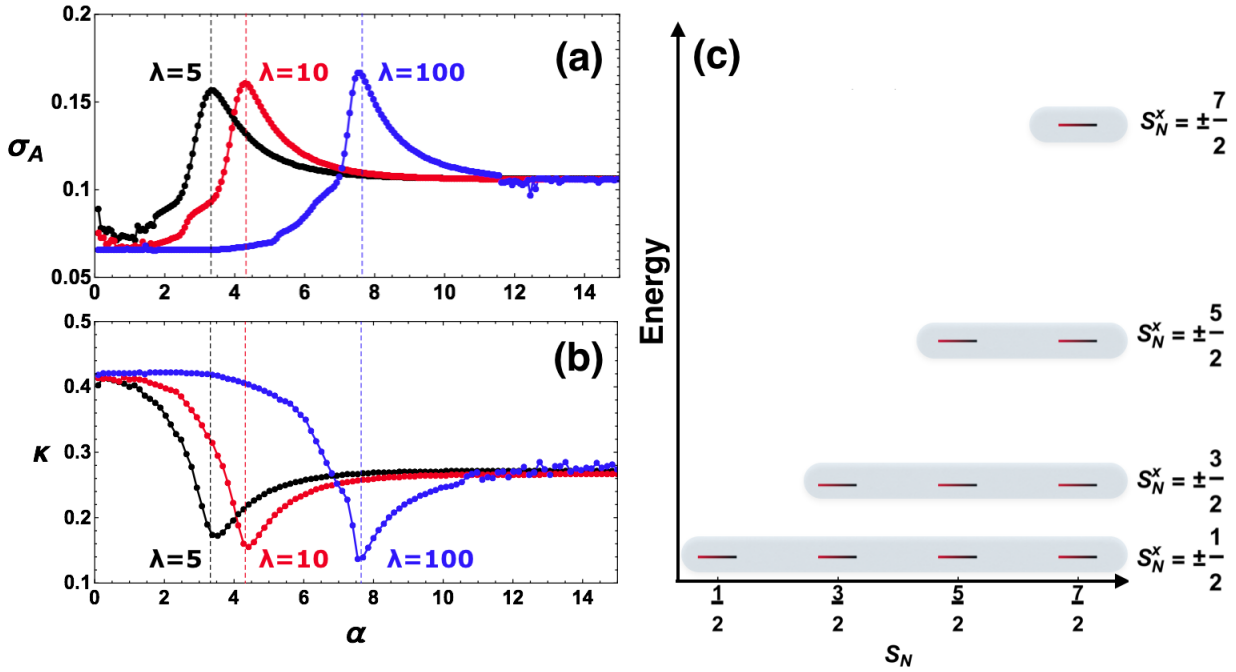

Figure 47: **Many-body dephasing:** (a) Standard deviation of temporal fluctuation σ_A for N=7 ions. (b) Size scaling exponent κ as a function of power-law coupling exponent α for fixed paramters $\lambda \equiv 2J_0/B$. (c) Energy level structure for $\lambda \to \infty$ ($B \to 0$), at $\alpha = 0$. S_N is the spin quantum number of N particles and S_N^x is the total spin component along the x-axis. These plots are produced from numerical calculations.

i.e., $|2^{-\alpha_c} J_0| = |B|$ resulting with $\alpha_c = \ln(2|\lambda|)/\ln 2$. In the regime of $\alpha \gg \alpha_c$ where the magnetic field energy overwhelms the NNN coupling, the Hamiltonian can be reduced into an integrable model by neglecting the NNN coupling (and other long-range coupling) terms. Then, adding the NNN coupling terms will weakly break the integrability and result in many-body dephasing, which is the case investigated thoroughly in Ref. (1). This regime is not accessible here, since the power-law exponent is around $\alpha \approx 0.7$. This experimental work lies in the opposite regime of $\alpha \ll \alpha_c$ where the coupling terms are dominant over the magnetic field energy.

In the global coupling limit of $\alpha = 0$, the Hamiltonian becomes

$$H_{\alpha=0} = BS_N^z + 2J_0(S_N^x)^2 + NJ_0/2$$

with $S_n^{x(z)} \equiv \sum_{i=1}^{n} \frac{1}{2}\sigma_i^{x(z)}$ as the total $x(z)-$component of spin for n particles. The Hamiltonian is an integrable model since there exist N conserved quantities of $\vec{S}_n^2$ $(n = 1, 2, \ldots, N)$ satisfying $[\vec{S}_n^2, H_{\alpha=0}] = 0$. In the case of $\lambda \to \infty$ $(B \to 0)$ and $\alpha = 0$, each energy level can be labeled by $|\Phi^{\lambda=\infty}_{S_1,\cdots,S_N,S_N^x}\rangle \equiv |S_1, S_2, \cdots, S_{N-1}, S_N, S_N^x\rangle$, which provides degeneracy[38]. These energy levels can be grouped into $N+1$ subspaces according to S_N^x as indicated in Fig. 47(c). The degeneracy of each S_N^x energy level grows exponentially in the limit of large N as

$$\frac{2^N}{\sqrt{N\pi/2}} e^{-2(S_N^x)^2/N}$$

(69). For a finite α, all the degenerate eigenstates in the subspace of S_N^x couple together and

[38]There are many options for choosing S_2 - S_{N-1} to yield the same energy state.

form new hybridized eigenstates $|\tilde{\Phi}_m\rangle$, which are assumed to be a roughly even admixture of all the (previously) degenerate energy states of S_N^x. As N increases, the number of lifted degeneracies grows, and there are assumed to be no redundant energy transitions (after the lift of degeneracy). The exponential increase in the number of lifted degenerate levels with N is what gives rise to the exponential decrease of fluctuations with N.

To conduct the Many-Body dephasing experiment, the spins are initialized into the $|\downarrow\downarrow ... \downarrow\rangle_z$ state by optical pumping with resonant 369.5nm light. Coherent spin rotations and spin-spin interactions are performed with a Raman scheme using counter-propagating Raman beams from a 355nm pulsed laser. State detection is performed with light that is resonant with the $|\uparrow\rangle$ state and off-resonant with the $|\downarrow\rangle$ state. Each ion is spatially resolved and imaged on an ICCD camera for state readout (6).

More specifically, the frequency comb from the 355nm pulsed laser is used to apply bichromatic Raman beat-notes to drive the Molmer Sorenson (MS) protocol (2) which is used to create the Hamiltonian 19. The bichromatic beat-notes are comprised of a tone red detuned of the red transverse motional sidebands and another tone blue detuned of the blue transverse motional sidebands. These tones off-resonantly excite the transverse modes of motion which determine the structure of the long-range spin-spin- couplings. MS is performed in the far detuned limit so spin-phonon entanglement is minimized.

The MS scheme in the far detuned limit creates the Ising Hamiltonian (43)

$$H = \sum_{i<j} J_{ij}\sigma_i^x\sigma_j^x, \;\; J_{ij} = \Omega^2\omega_R \sum_m \frac{b_{im}b_{jm}}{\mu^2 - \omega_m^2}. \tag{21}$$

Ω is the global carrier Rabi frequency between the electronic states $|\downarrow\rangle_z$ and $|\uparrow\rangle_z$. $\omega_R = \hbar\Delta k^2/(2M)$ is the recoil frequency, b_{im} is the normal mode transformation matrix of the i-th ion with the mth normal mode, Δk is the difference wave-vector between the two Raman beat-notes. M is the mass of a single ion, ω_m is the frequency of the m-th normal mode, and μ is the detuning of each beat-note from the carrier. Equation 21 shows that the collective modes of vibration of the ion chain mediate the long-range spin-spin coupling. The transverse field, along $\hat{z}$, is created by adjusting the detuning μ in the same direction for both the red and blue Raman tones. For a shift of D, the effective magnetic field is $B_z = D/2$ (3).

The noise in the experiment is mainly σ_z noise which results from instability in the laser fields driving the interaction, and noise in the RF drive on the trap blades. If the Light shift from the laser fields are not balanced, a stray B_z field will result and is explained in the following description. In the course of data collection, the differential Light Shift between the red and blue Raman tones is routinely balanced. While the light shift is fairly stable over the course of one experimental scan (which takes $\sim$ 2 minutes), the net Light Shift will change between different scans; mainly from drifts in beam pointing. When corrected for, this noise will vary by about 0.1 kHz$\times 2\pi$. With a net Light Shift, an effective B-field is created along $\hat{z}$. J_0 is typically more stable, and was measured before and after taking a set of data and will drift by around 5%.

After the quench with Hamiltonian 19, the spins are allowed to evolve and are measured in 50 time-steps between (0-2.0) ms. The magnetization of the spins is measured in the $\hat{z}$ basis. During a given scan, 200 experiments per time-step are taken. Each experimental scan is repeated 5-7 times (Figure 48) in order to have a large sample which will suppress

Experimental Parameters

Experimental Details			
Ions	mean α	Total exp/point	Range of J_0 (kHz)
3	0.725815	1000	0.53-0.541
4	0.70957	1000	0.50-0.60
5	0.692255	1000	0.45-0.55
6	0.678499	1200	0.41-0.53
7	0.664681	1200	0.39-0.52
8	0.648291	1400	0.38-0.48

Figure 48: Experimental values used for $N = 3$ to 8 ions.

the measurement noise. This allows for the detection of persistent fluctuations. Figure 48 summarizes the experimental values used. The number of ions used was 3 to 8, and the number of total experiments taken increased with ion number since the fluctuation signal decreases as ion number increases.

For each ion, and for each time step, all of the data points are averaged; that is an average of 1000-1400 values depending on N (Fig.48). Then, all of the ions in a given time step are averaged. This results in data that can be plotted as average magnetization as a function of time, Fig.49.

The two plots in Figure 49 show the magnetization data as a function of time with a 4 ion chain taken with Bz=+/-0.5 kHz$\times 2\pi$. The blue points are data while the black and red are theory. The black curve is theory with the measured values for J_0 and B taken as exact values with no variance. The red curve is a theory fit where the measured values for J_0 and B are fixed and the variance in those values, σ_{J_0} and σ_B, are varied using a gradient descent algorithm to fit to the data[39]. In the case displayed in Fig.49, the best fitting values for the

[39]This assumes that the noise in J_0 and B are Gaussian distributed.

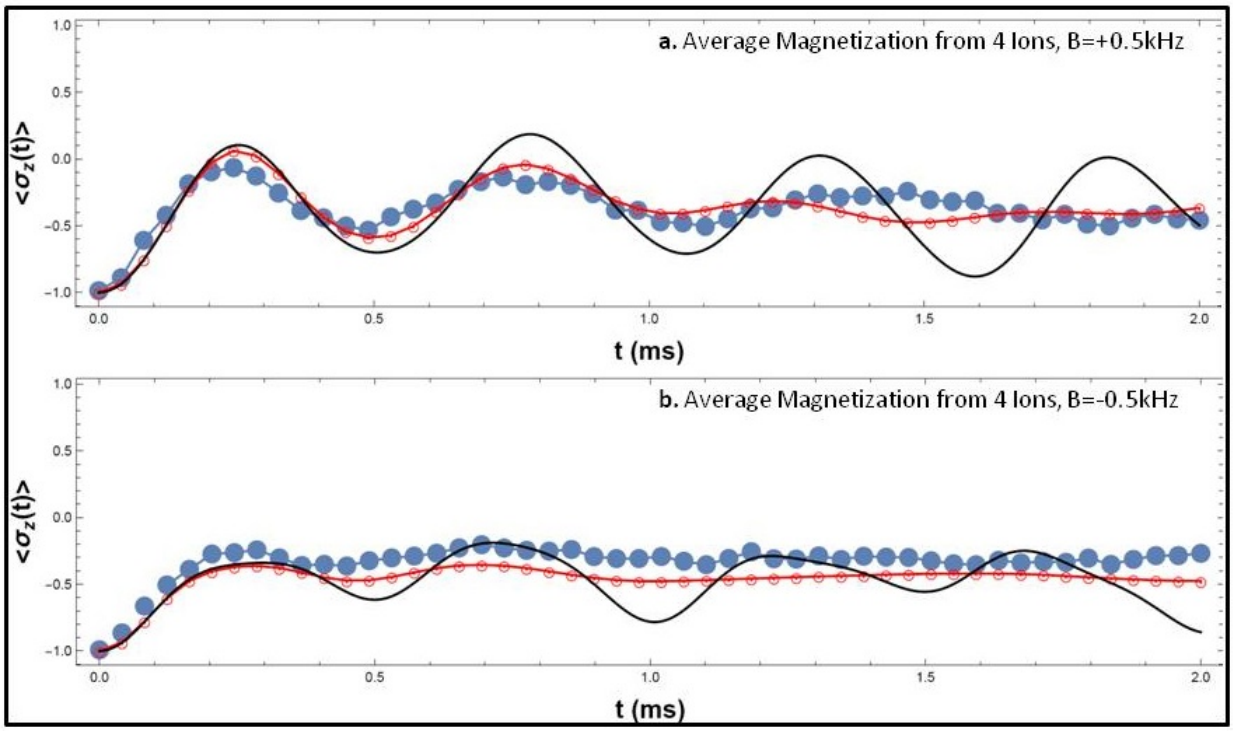

Figure 49: Average magnetization, $\langle\hat{\sigma}_z(t)\rangle$, over 4 ions out to 2ms. Each data point is the average of 4000 experiments. **a.** shows the magnetization for $B = +0.5$ kHz$\times 2\pi$. **b.** shows the magnetization for $B = -0.5$ kHz$\times 2\pi$. For both plots: Blue are experimental data points, Red and Black are theory, respectively with and without noise in J_0 and B considered.

variances are $(\sigma_{J_0},\sigma_B) = (0.0617, 0.030)$ kHz$\times 2\pi$ for (a) and $(\sigma_{J_0},\sigma_B) = (0.10, 0.162)$ kHz$\times 2\pi$ for (b).

In general, with a positive B-field, there are more significant oscillations than when using a negative B-field[40]. When considering the energy spectrum of the Hamiltonian in the non-integrable case with long-range decaying interactions as compared to the integral case, an energy gap opens up in the ferromagnetic (FM) side of the energy spectrum. If the quench Hamiltonian has a positive B-field, the dynamics start from the FM end of the spectrum and respond to the energy gap with more persistent oscillations. Accordingly, when using a

[40]The sign of the B-field depends on the relative orientation between the B-field and the initial state of the ions.

negative B-field, the dynamics start from the AFM side of the spectrum (35).

The fluctuations are characterized by measuring the standard deviation of the average magnetization of the sum of all ions in a chain. The standard deviation of the last 48 (out of 50 total) steps is taken to characterize the fluctuations, Fig.50.

The stdev of the average magnetization can be plotted as a function of $\lambda = 2J_0/B$, where B takes on the values of $^+/_-(0.5, 0.75, 1.0, 1.5, 2.0)\text{kHz}\times 2\pi$, as in Fig.50. Other B values are used to fill in features of the curve. Since the stdev was calculated from the last 48 time steps, the associated 95% confidence interval of the stdev extends between (0.83, 1.25) of the calculated value (68).

The standard deviation of the average magnetization was plotted as a function of $\lambda = 2J_0/B$ for fixed N in Figure 50. The theory and experiment match well for $N = 3 - 7$ ions. For $N = 8$ ions, there is too much experimental noise to resolve the fluctuations of interest.

In the stdev plots, the values near $\lambda = 0$ were not taken, as $B \gg J_0$, and the ions are predominantly acting paramagnetically. In this regime, fluctuations are expected to be very small and well below the noise floor of this experiment[41].

The shape of the data is asymmetric with a pronounced slope at $2J_0/B = +1/2$. This point marks the FM to paramagnetic phase transition of the ion chain. The fluctuations are enhanced here as this is an unstable point for the system. The AFM to paramagnetic phase transition at $-|\lambda|$, is not well defined as explained in (67).

The theoretical formula used to calculate the temporal fluctuations implies integrating over an *infinite* time window, i.e, averaging over $J_0 t \in [0, +\infty]$. However, experimentally, one

[41] As seen in Fig. 50, the noise floor rises with increasing N.

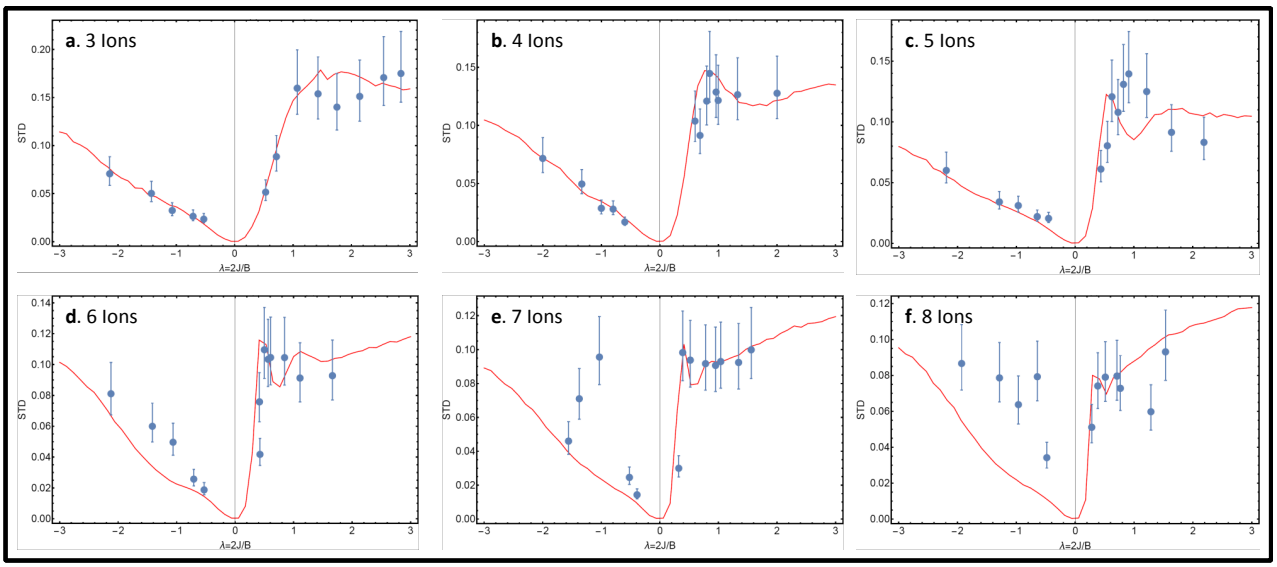

Figure 50: Standard deviation of the average magnetization for N=3-8 ions as a function of $\lambda = 2J_0/B$. The data for 3 to 6 ions agree with the theoretical prediction. The 7 ion data largely agrees with theory excluding the two outlying points at negative λ values. For 8 ions, the data points tend to gather around the 0.07 level. This indicates that the measurement noise for 8 ions obscures the measured fluctuations.

can only average over a *finite* time window as the long-time fluctuations are suppressed by the noise of interaction J_0 and magnetic field B.

First, the finite window effect is discussed. In Fig. 51(a), the experimentally accessible parameters $\alpha = 0.7$ and $\lambda = 1.7$ are chosen and used to numerically plot the logarithm of temporal fluctuation $\ln \sigma_A$ as a function of system size with different finite time windows (the connected black empty circles). The short-time-window averaging only makes sense for small system size, e.g., the time window $J_0 t \in [0, 2\pi]$ works up to $N = 6$ spins. Larger system sizes result in smaller level splittings which make the period of temporal fluctuations longer; thus necessitating a longer time window to calculate the temporal fluctuations. The linear fitting to the infinite time window averaging is shown with the red dashed line. The slope determines the fluctuation decay constant as $\kappa = -0.35$.

In Fig. 51(b), the noise of interaction J_0 and magnetic field B in the experiment is considered. The results plotted are extracted from measured data (blue dots with error bars) and compared to numerical results (unconnected circle dots) calculated with finite window $J_0 t \in [0, 2\pi]$, with $J_0 = 0.5\,\mathrm{kHz}$ and $B = 0.59\,\mathrm{kHz}$ (i.e., $\lambda = 1.7$), both with $0.1\,\mathrm{kHz}$ standard deviation.

The slope, $\kappa = -0.35$, from the infinite time window is compared to the experimental data. This slope seems reasonable to describe the first three data points. This suggests that the experimental noise basically shrinks the temporal fluctuations by a factor without changing the size scaling exponent κ.

Using this trapped ion quantum simulator, the first experimental observation of persistent temporal fluctuations after a quantum quench was measured. The Hamiltonian used is that of a long-range interacting transverse-field Ising model. The transverse field is varied to measure the fluctuations in the average magnetization of the spin chain. This experiment was performed in the near-integrable regime where analytical solutions are available, though the system is non-integrable. Numerical simulation compared with experiment show that as a function of system size N, the exponent describing the decay of fluctuations matches well with the theoretical value.

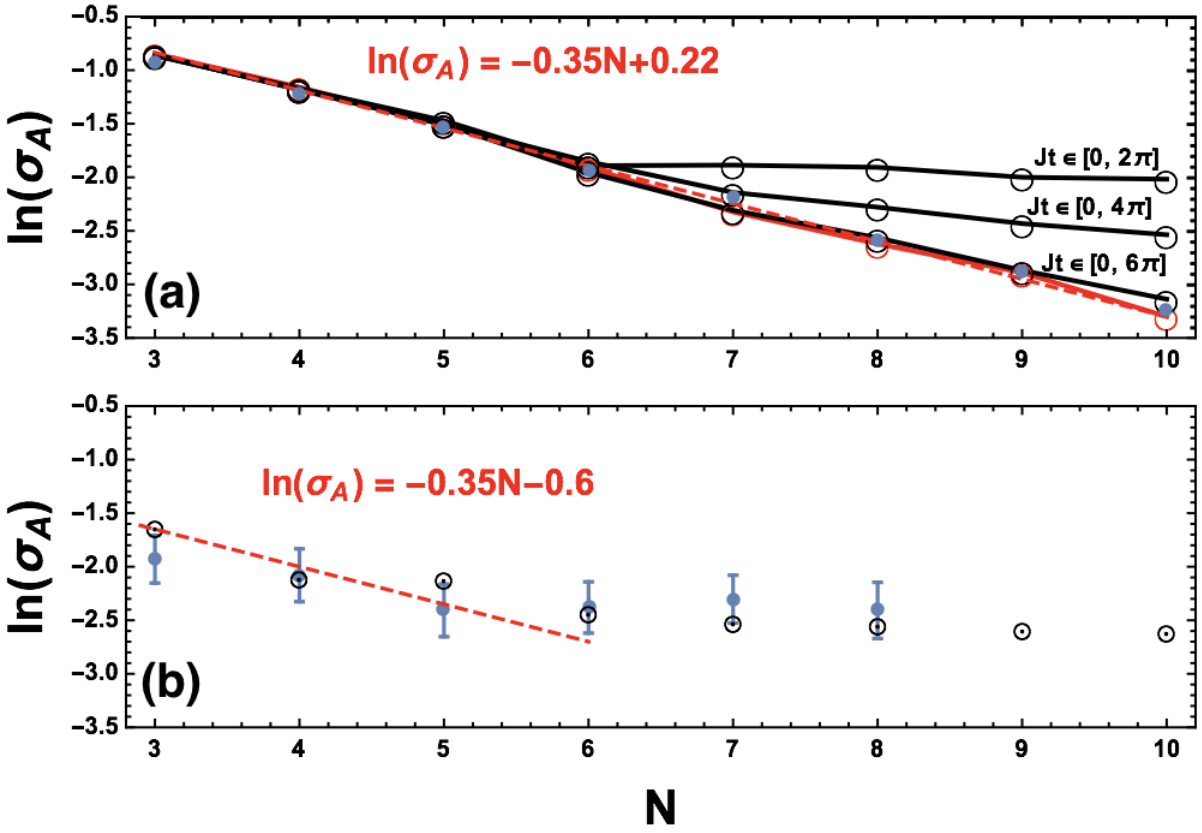

Figure 51: **System size scaling:** (a) Logarithm of temporal fluctuation $\ln \sigma_A$ vs system size N with experimentally accessible parameters $\alpha = 0.7$ and $\lambda = 1.7$. The connected red empty circles are calculated from the analytical formula (20) which is valid for infinite time window averaging. The three curves of connected black empty circles are calculated from numerical time evolutions with finite time window averaging as indicated beside each curve in the plot. The blue dots are from an approximate empirical formula. (b) $\ln \sigma_A$ vs system size N extracted from experimental data (blue dots with error bars). The circle dots are calculated numerically with finite window $Jt \in [0, 2\pi]$ and parameters $J = 0.5\,\mathrm{kHz}$ and $B = 0.59\,\mathrm{kHz}$ ($\lambda = 1.7$) with the same standard deviation $0.1\,\mathrm{kHz}$. The upper and lower red dashed lines are the linear fittings.

19 Future experimental directions and conclusion

The cryogenic quantum simulation experiment has been used to perform a number of experiments (19) (21) with others on the horizon, but there are still technical features that beg to be improved. This chapter serves to discuss areas where improvements can go a long way in making the apparatus more stable, or to add more functionality. The ideas presented here are on the speculative end of the spectrum, but it is important to include them when considering future directions.

It is clear that the cryostat dramatically decreases the heating rate and the vacuum pressure (or at least the energy of the background gas) (6) (44). For one ion, the heating rate was measured to be 1.28(1.09) quanta/second for the $\hat{y}$ direction and 2.92(1.73) quanta/second for the $\hat{z}$ direction. For room temperature traps, heating rates can be anywhere from 20 to 130 quanta/second (12). In spite of these improvements, there are clearly challenges that are introduced, and include the following:

-The ions are far from the objective,

-The ions move around in time.

If one is able to improve the vacuum and heating rate for room temperature systems, that would be very useful to eliminate these problems. If the cryogenic apparatus is necessary, then one idea is to put much of this apparatus in vacuum. In particular, this would include taking the laser systems and the imaging system and designing them to sit in vacuum with the trap. This could take on the form of integrated photonics (23) or in-vacuum lens and fiber systems. With this, there will be no relative motion between the ions and the rest of the supporting equipment. As the supporting infrastructure gets smaller, this vision will become

more compelling.

On a more immediate level, this experiment will greatly benefit from having an individual addressing beam (as the warm experiment has greatly benefited from (24) [42]). The main challenge is concerning the fact that the ions drift around on the order of the ion spacing. Recently (August 2019), experiments were performed with the imaging system which indicated that much of this motion was coming from the objective moving around. The objective was held on a cantilevered holder mounted on a 3-axis translation and tilt stage. Since the objective is out of vacuum, it should be reasonable to mount it in a more stable way. This improvement may not completely eliminate the ion position drift, as some of the drift may still be coming from the fact that the ion trap is mounted on a pendulum. Potentially, this could be delt with by using a feedback loop that corrects the pointing of the 'poke beam'. This feedback could look at a certain mechanical object on the trap, or it could perhaps track the position of a given ion or even an ion of a different isotope or species.

Currently when cooling a long ion chain, sideband cooling tones are tuned to specifically cool individual modes of motion. When scaling to larger systems, cooling this way may take significant time and slow down experiments, or one mode might get heated when another is becoming cooled. An alternative cooling technique is to use EIT cooling, which has been adapted to the energy structure of $^{171}Yb^{+}$ (25) (26). Using EIT cooling will allow for the entire bandwidth of motional modes to be cooled simultaneously. This should reduce cooling times and leave no way for individual modes to get heated during the cooling process.

[42] This allows for the preparation of arbitrary product states.

As discussed earlier, the ion chain experiences decoherence from vibration from the cryostat and from beam-pointing instabilities. Currently, the frequency comb scheme used with the Raman beams to create the red and blue sidebands for the MS scheme is setup so it is sensitive to these vibrations. In short, when the ions move relative to the Raman beams, or when the relative length of the Raman paths change, the ions sample different phases from the Raman beams than if they were stationary. There is another configuration of the Raman beams such that, based on how the red and blue sideband tones are created from the Raman beams, the different phase sampled cancels out (45). This is a more short term project and is already underway in the lab.

One of the goals of this apparatus is to perform quantum simulation experiments with long ion chains. In particular, long enough so that classical computers can't keep up (27). This regime of quantum simulation is termed quantum supremacy or quantum advantage. In this regime, the elephant in the room is: How does one verify the results from a quantum simulator in this regime and expect others to believe the results that are peddled to them?

This is not an easy question to answer, but there are several approaches. One approach is to, for a given system size, perform experiments where the answer is classically tractable to verify that the simulator is doing what it is alleged to be doing. Then, the non-classically tractable simulation can be run with some level of confidence. The other option is to build a second quantum simulator of the same size. In principle, the same simulation can be run on separate quantum simulators and the results can be compared together to see if they agree. Perhaps both of these methods should be used together to increase the confidence of results.

Part VI

Appendixes

A Raman rotations with CW tones and a frequency comb

Stimulated Raman transitions are responsible for all the coherent atomic manipulations performed with the 355 pulsed laser. First, the case of a Raman scheme between two continuous wave (CW) light fields on a Λ atomic structure will be considered. Figure 52 shows a Λ energy level structure where the spin states $|\uparrow\rangle$ and $|\downarrow\rangle$ are directly coupled to the state $|e\rangle$, but not to each other. Two CW laser frequencies are applied to the system with frequencies ω_1 and ω_2 which are detuned by Δ_1 and Δ_2 from the energy splittings ω_{01} and ω_{02} respectively (22).

The general idea is to off-resonantly use the state $|e\rangle$ to make the spin states into an effective 2-level (spin 1/2) system.

The Hamiltonian describing the atomic levels interacting with two laser fields is

$$\begin{aligned}\hat{H} = (\omega_{01}-\omega_{02})|\uparrow\rangle\langle\uparrow| + \omega_{01}|e\rangle\langle e| - \left(E_1 e^{-\mathrm{i}\omega_1 t} + E_1^* e^{\mathrm{i}\omega_1 t}\right)(\mu|\downarrow\rangle\langle e| + \mu^*|e\rangle\langle\downarrow|) \\ - \left(E_2 e^{-\mathrm{i}\omega_2 t} + E_2^* e^{\mathrm{i}\omega_2 t}\right)(+\mu|\uparrow\rangle\langle e| + \mu^*|e\rangle\langle\uparrow|)\end{aligned} \tag{22}$$

where the state $|\downarrow\rangle$ is defined to be at zero energy. E_i is the electric field, μ is the dipole operator, and the Rabi frequency $\Omega_i = \mu E_i$.

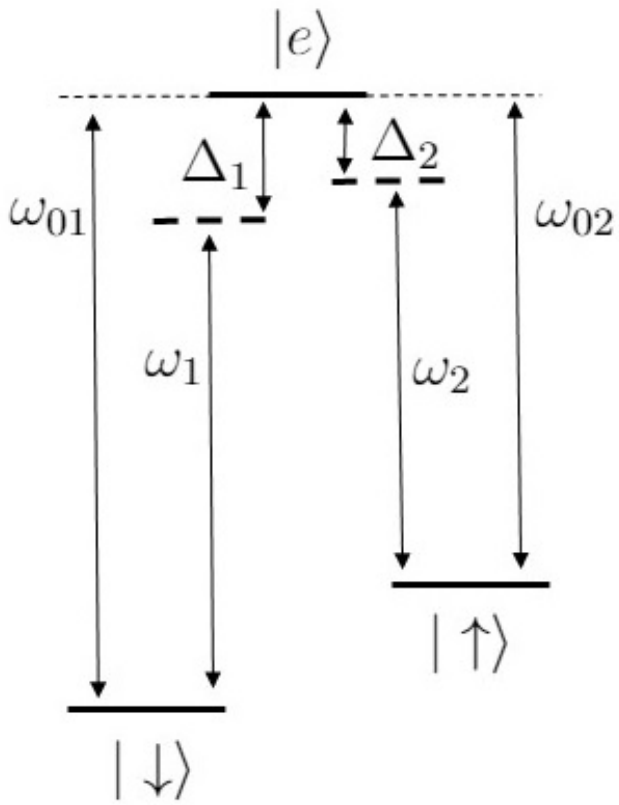

Figure 52: Λ **Raman scheme**: The states $|\uparrow\rangle$ and $|\downarrow\rangle$ are directly coupled to the common excited state $|e\rangle$, but not to each other. When driven with off-resonant laser fields, the excited state is effectively eliminated and the lower two states become an effective 2-level (spin 1/2) system.

The Hamiltonian, Eq. 22, is transformed into the rotating frame with the unitary

$$\hat{U} = e^{-\mathrm{i}\omega_1 t|e\rangle\langle e| - \mathrm{i}(\omega_1 - \omega_2)t|\uparrow\rangle\langle\uparrow|} \tag{23}$$

using the transformation to the rotating Hamiltonian given by

$$\hat{H}_{rot} = \hat{U}^\dagger \hat{H} \hat{U} - \mathrm{i}\hat{U}^\dagger \dot{\hat{U}}. \tag{24}$$

The Baker-Hausdorff formula (65), is used to manipulate $\hat{H}_{rot}$, and the rotating wave

approximation is made by neglecting any terms that have a very high effective frequency. For example, exponential terms that go as $e^{(+/-)\mathrm{i}2\omega_{1,2}}$.The resulting Hamiltonian is

$$\begin{aligned}\hat{H}_{rotApprox} &= (\Delta_1)|e\rangle\langle e| + (\Delta_1 - \Delta_2)|\uparrow\rangle\langle\uparrow| \\ &- [\Omega_1|e\rangle\langle\downarrow| + \Omega_2|e\rangle\langle\uparrow| + \Omega_1^*|\downarrow\rangle\langle e| + \Omega_2^*|\uparrow\rangle\langle e|)]\end{aligned} \tag{25}$$

Where the relationships between $\Delta_{1,2}$, $\omega_{1,2}$, and $\omega_{0(1,2)}$ are given by Figure 52.

Assuming the generic time-dependant state $|\psi\rangle = c_1|\downarrow\rangle + c_2|\uparrow\rangle + c_e|e\rangle$, the equations of motion become

$$\begin{aligned}\dot{c_1} &= \mathrm{i}\Omega_1^* c_e, \\ \dot{c_2} &= -\mathrm{i}(\delta)c_2 + \mathrm{i}\Omega_2^* c_e, \\ \dot{c_e} &= -\mathrm{i}\Delta_1 c_e + \mathrm{i}\Omega_1 c_1 + \mathrm{i}\Omega_2 c_2\end{aligned} \tag{26}$$

where $\delta = \Delta_1 - \Delta_2$. Now the state $|e\rangle$ can be adiabatically eliminated by setting $\dot{c_e} = 0$. This is motivated by saying that the detuning Δ_1 is large and particularly larger than the line-width of $|e\rangle$, and therefore the population transferred into and out from $|e\rangle$ is negligible which is written as $\dot{c_e} = 0$.

The last equation can be solved for c_e and plugged into the first two equations. The terms are arranged to identify the effective 2-level Hamiltonian as

$$\hat{H}_{2Level} = \frac{|\Omega_1|^2}{\Delta_1}|\downarrow\rangle\langle\downarrow| + \left(-\delta + \frac{|\Omega_2|^2}{\Delta_1}\right)|\uparrow\rangle\langle\uparrow| + \left(\frac{\Omega_1^*\Omega_2}{\Delta_1}|\downarrow\rangle\langle\uparrow| + h.c.\right) \tag{27}$$

where the effective Rabi frequency is proportional to $\Omega_1^* \Omega_2$.

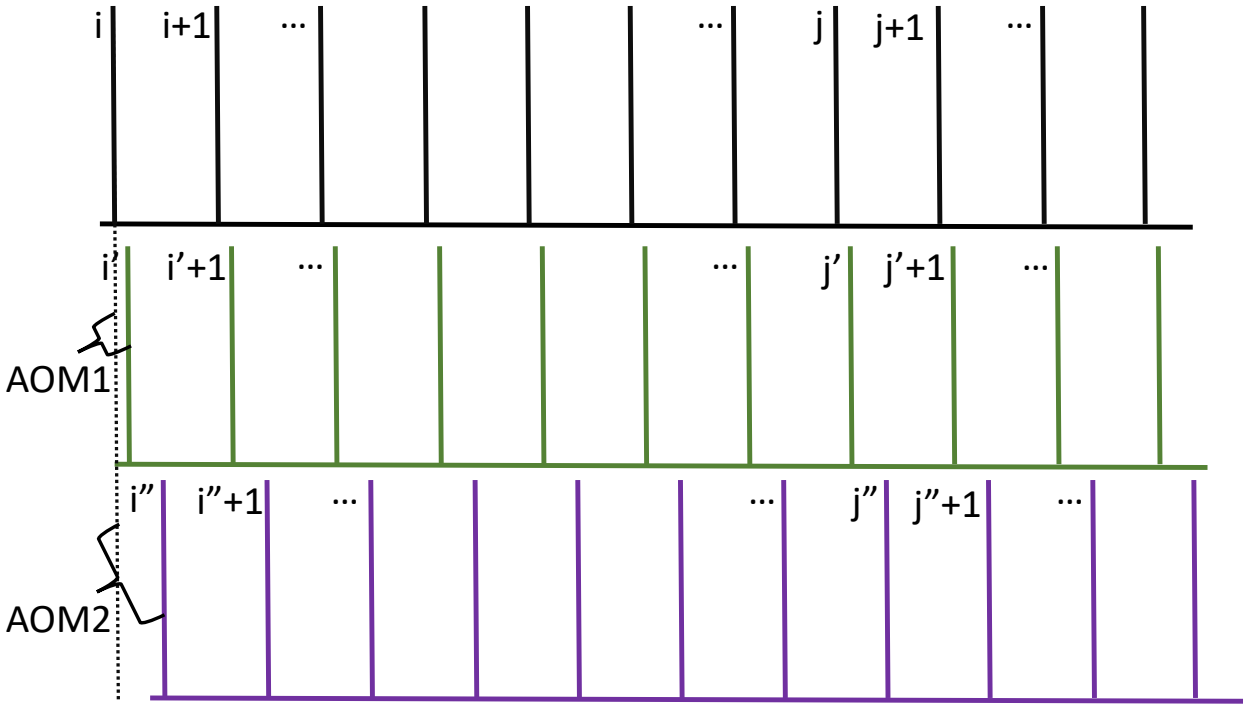

Figure 53: **Frequency combs from the 355nm pulsed laser**: Frequency combs are depicted where each vertical line represents a different frequency and the comb spacing is ν_{rep}. The black comb represents the frequency comb directly from the laser. That frequency comb is split into two beams and each beam is sent through an AOM. The green comb represents the comb frequencies shifted by AOM1 and the purple comb shifted by AOM2.

This derivation thus far considers two CW laser frequencies, but in practice, a frequency comb is used. The 355 Pulsed laser produces high intensity pulses of light that create a pulse-train in time. When Fourier transformed into the frequency domain, the pulse-train results in a frequency comb of CW frequencies that are centered around the 355nm carrier frequency. More details about frequency combs and how they are applied to trapped-ion systems are discussed elsewhere, (45) (11)

Figure 53 illustrated how the carrier frequency is produced in order to drive the transition

between the $|\downarrow\rangle$ and $|\uparrow\rangle$ states. The pulsed laser has a repetition rate, $\nu_{rep} = 81.4198$MHz, which is the frequency spacing between the comb-teeth. The black comb represents the frequency comb before being split up into two combs and frequency shifted by AOM1/2. The beam (frequency comb) is split up into two beams in order to have counter-propagating beams to drive Raman transitions[43]. In effect, the atom absorbes a photon at a frequency of one of the comb teeth from one comb and emits at a frequency of one of the comb teeth of the other comb.

AOM1 shifts the frequency of the comb teeth by $\nu_{AOM1} = 107.322$ MHz and AOM2 shifts the frequency of the comb teeth by $\nu_{AOM2} = 211.4936807$ MHz. The AOM frequencies are chosen such that the difference between the $i'^{\,th}$ and the $j"^{\,th}$ comb teeth is the carrier frequency, $\nu_{carrier} = 12.642819$ GHz. In this apparatus, both AOM1 and AOM2 are situated so that the $+1^{st}$ diffracted order is used. Therefore, the carrier frequency follows the relation

$$\nu_{carrier} = n\nu_{rep} + \nu_{AOM1} - \nu_{AOM2} \tag{28}$$

where n is an integer and represents the number of times the frequency ν_{rep} separates the comb teeth i' and $j"$ (once the AOM shifts are accounted for). In this apparatus $n = 154$; of course, there are many frequency comb pairs that are separated by n and contribute to driving the carrier transition.

When red and blue sidebands are needed to drive the MS interaction, one AOM (AOM2

[43]In Figure 53, the two combs that are frequency shifted are purposely not colored red and blue. When red and blue sidebands are applied to create the MS interaction, a 'red' and 'blue' tone are applied to one of the AOMs to create this effect. Here, the two combs are being positioned in frequency space in order to drive the carrier.

in this case) is driven with RF tones that are red and blue detuned from the carrier transition by the desired amount. When the atom absorbs and emits from the comb from AOM1 and the red and blue shifted combs from AOM2, the red and blue Raman beat-notes are created.

The comb-teeth frequencies are centered at ν_{355nm} which excites ions starting from the $^2S_{1/2}$ manifold, off-resonantly with the $^2P_{1/2}$ and $^2P_{3/2}$ states. This creates the Raman scheme described here.

B Collisions with gas in the vacuum and characterization of cryogenic vacuum

The background pressure requirements for ion trap experiments are demanding primarily for two reasons. First, the ions interact with the residual neutral molecule gas with the long range $\sim r^{-4}$ potential, which increases the collision rate compared to, for example, neutral-neutral collisions rates which are governed by Van-der-Waals $\sim r^{-6}$ potentials. Secondly, since the Paul trap is not static, the collisions with a bath of neutral particles can induce heating by displacing the ions diabatically with respect to typical rf timescales. This depends on the mass imbalance[44] and on the instantaneous rf phase at which the collision occurs (46; 47; 48). As a consequence of this instantaneous and random amplification of the ion motion, the ion crystal melts, rf heating takes place, and the ions are either ejected out of the trap or left in highly excited orbits where laser cooling is inefficient. The ion chain lifetime depends strongly on the Mathieu parameter $q \simeq 2\sqrt{2}\omega_{\mathrm{tr}}/\Omega_{\mathrm{rf}}$ of the trap in consideration. Once one ion is displaced by a collision, nonlinearity coming from the Coulomb repulsion will cause the ion's kinetic energy to grow at a rate that scales as a power law of q with an exponent greater than or equal to 4[45] (49). The q parameter sensitivity is also related to higher order terms in the rf trapping potential expansion beyond the first order quadrupolar contribution. These terms are associated with nonlinear resonances inside the stability region of a linear Paul trap (50; 51) that are likely to accelerate the ion loss once the crystal has melted.

In this cryogenic vacuum system, a catastrophic ion collision event has not been observed,

[44] Between the $^{171}Yb^{+}$ ion and the H_2 molecule in this case.

[45] This heating effect is counteracted by the effect of Doppler cooling.

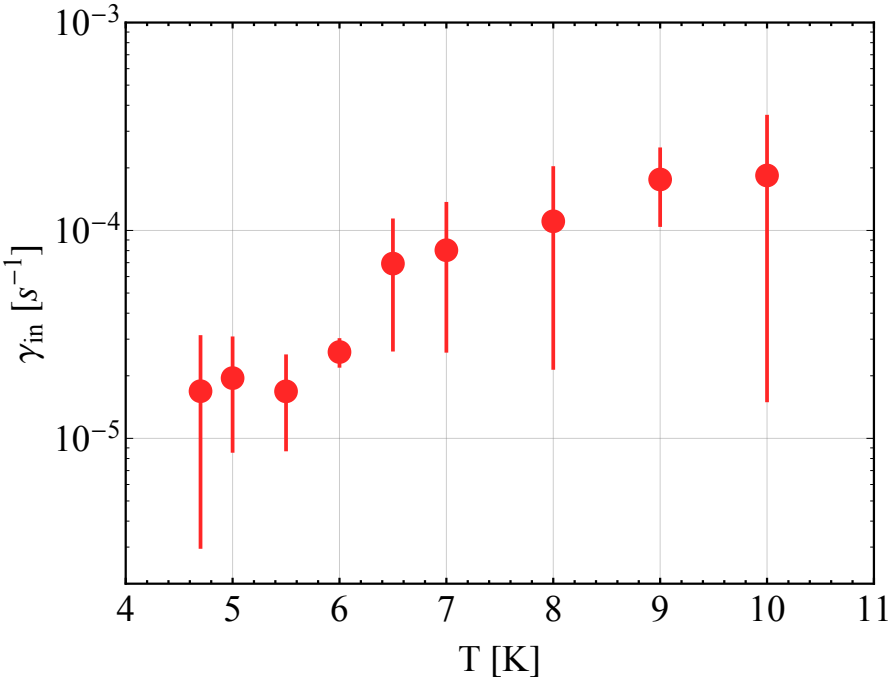

Figure 54: **Average dark ion rate as a function of temperature**: the data have been acquired with 33 ions for a time period varying from 12 hours to 3 hours. The reported inelastic rate is per ion, estimated by averaging the time intervals between dark events. The error bars are the time interval standard deviations of each data set. The size of the error bars is caused by the poor statistics, due to the rare occurrence of inelastic collision processes.

even for chains of more than 100 ions at $q = 0.35$. Any chain-loss events can be attributed to instability in the cooling laser. In general, the ion chain will stay trapped as long as the cooling laser is locked. In the room temperature UHV experiment, with the same q, the lifetime of a chain of about 50 ions is on average 5 minutes (52). The enhanced lifetime can be attributed to two factors: on one hand differential cryo-pumping reduces the residual gas density with respect to standard UHV systems, which reduces the overall collision rate. Secondly, even when a collision occurs, the average energy transfer $\langle \Delta E_{\mathrm{Yb}^+} \rangle$ is about 60 times lower than in a room temperature UHV experiment, and therefore the crystal melting is less likely to happen as the Doppler cooling laser can efficiently recapture and recrystalize the ions.

In a UHV apparatus (at room temperature), $\langle \Delta E_{\mathrm{Yb}^+} \rangle \simeq k_B \times 10$ K for H_2 molecules,

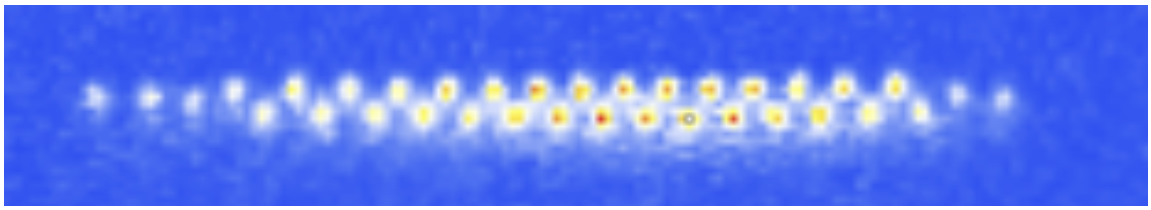

Figure 55: **Zig-Zag ion chain**: Zig-zag chain with $N = 35$ ions with $(\omega_x, \omega_y, \omega_z) = 2\pi \times (67, 613, 632)$ kHz.

which, according to numerical simulations, is not sufficient to displace the ions enough to melt the crystal. According to numerical simulations (See the next appendix), catastrophic collisions in a room temperature UHV system are most likely caused by rare collisions with heavier residual background gas species, (N_2, CO_2 and H_2O), that in a cryogenic system are completely frozen.

In order to quantify the background pressure in the vacuum system, a hot cathode ionization gauge should not be used as it can generate additional gas load. Moreover, the gauge in use measures the pressure of the room temperature vacuum region (see Fig. 8b), which is on the order of low 10^{-9} Torr when the apparatus is cold. Since both the 40 K and the 4 K cryogenic regions are not vacuum sealed, it is difficult to estimate the inner pressure relative to the pressure in the room temperature region by using differential cryo-pumping. For this reason, the ion crystal is used as a pressure gauge by measuring collision rates with the molecular hydrogen background gas as a function of the cryostat temperature (20).

The ion-neutral molecule interaction is described by a $\sim r^{-4}$ potential, stemming from the interaction between the charge e of the ion and the induced electric dipole moment of the

molecule with static polarizability α:

$$U(r) = -\frac{\alpha}{2}\frac{e^2}{4\pi\varepsilon_0 r^4} = -\frac{C_4}{r^4}. \tag{29}$$

One can safely assume the validity of the classical Langevin model (53) with no quantum corrections, since the average energy of the incoming H_2 molecule $\langle E_{H_2}\rangle$ is much larger than the p-wave centrifugal barrier associated with the potential (29), which can be approximated as $E_4 = \hbar^2/2\mu R_4^2 \simeq k_B \times 3$ mK, with $R_4 = (2\mu C_4/\hbar^2)^{1/2}$ and μ as the reduced mass (54).

In the Langevin model the collision rate γ is independent of the energy of the incoming particle and is directly proportional to the density n, or equivalently to the pressure P assuming the ideal gas law. This results in:

$$\gamma = n\, e\sqrt{\frac{\alpha_{H_2}\pi}{\mu\,\varepsilon_0}}, \quad n = \frac{P}{k_B T}. \tag{30}$$

In order to estimate the residual background pressure inside the cryostat, the rate at which dark ions are produced is measured. Indeed, whenever a collision occurs, there is a finite unknown probability P_{in} that two inelastic processes take place: (a) optically excited ions $^{171}\text{Yb}^{*+}$ in the $^2P_{1/2}$ or $^2D_{3/2}$ states, both populated by the Doppler cooling light at 369 nm, are subjected to collisional quenching that leads to population in the metastable $^2F_{7/2}$ state (55). (b) Molecule association: an optically excited ion has enough energy to chemically react with H_2, breaking its bond and forming an ytterbium hydride (YbH^+) molecule (42). In both cases the ions stop scattering Doppler cooling photons and appear as missing in

the ion chain. Therefore, a relative measurement of the pressure is obtained by recording the occurrence rate of dark ions, namely $\gamma_{\text{in}} = P_{\text{in}}\gamma$. The dark ion rate is measured as a function of the temperature of the cryostat (see Fig. 54) observing an increase by an order of magnitude, with a temperature increase of 5.5 K. By comparing the dark ion rate in the cryogenic vacuum system with the room temperature UHV system with a gauge-measured pressure of $1 \cdot 10^{-11}$ Torr and $\gamma_{\text{in}}^{(300\text{K})} = 2 \cdot 10^{-4}$ s^{-1} per ion, one can infer the residual background pressure as:

$$P_{4\text{K}} = P_{300\text{K}} \frac{\gamma_{\text{in}}^{(4\text{K})}}{\gamma_{\text{in}}^{(300\text{K})}} \frac{k_B T_{4\text{K}}}{k_B T_{300\text{K}}}. \tag{31}$$

With this method, the pressure is estimated to be $P_{4\text{K}} < 10^{-13}$ Torr.

In order to measure the pressure, the rate of reconfiguration events γ_{el} caused by elastic collisions is considered when N ions are in the zig-zag configuration (56), namely when $\omega_{y,z}/\omega_x < N/\sqrt{\log(N)}$, where $\omega_{y,z}$ are the two transverse frequencies and ω_x is the axial frequency (see Fig. 55). When this condition is met, there are two degenerate configurations separated by a small energy gap, which depends on the transverse mode splitting $\Delta\omega_{\text{tr}} = \omega_z - \omega_y$. When an elastic collision occurs, the ions have a finite probability to switch from the "zig" to the "zag" configuration, if the energy gained by the ions is enough to overcome the barrier. Therefore, the observable used is $\gamma_{\text{el}} = p_{\text{flip}}\gamma$, where p_{flip} is the probability of flipping the zig-zag chain, which is a function of the transverse mode splitting $\Delta\omega_{\text{tr}}$ and of the energy of the incoming particles. In order to calculate p_{flip}, a numerical simulation is performed of 31 ions in a Paul trap after a collision with a H_2 molecule with mean energy $\langle E_{H_2} \rangle = 3/2\, k_B T$

over 2×10^4 rf periods, the probability dependence on the temperature and on the energy barrier is calculated (for details, see the next appendix). The elastic rate $\gamma_{\rm el}$ has been measured at $\Delta\omega_{\rm tr} = 2\pi \times 2$ kHz at two different temperatures ($T = 4.7$ K and the $T = 7$ K). By inverting Eq. (30) and using the calculated $p_{\rm flip}$ values, the pressure has been measured to be $P = (1 \pm 1) \cdot 10^{-12}$ Torr and $P = (2 \pm 1) \cdot 10^{-12}$ Torr for $T = 4.7$ K and 7 K, respectively.

C Numerical simulation of elastic collisions

The following simulation was created by Y. Wu as described in (6).

Consider a trap with $\Omega_{\text{rf}} = 2\pi \times 24\,\text{MHz}$ and $\omega_x = 2\pi \times 67\,\text{kHz}$, and $(\omega_y + \omega_z)/2 = 2\pi \times 622.5\,\text{kHz}$. For $N = 31$ ions and transverse splitting up to $\Delta\omega_{\text{tr}}/2\pi = (\omega_z - \omega_y)/2\pi = 299\,\text{kHz}$, the equilibrium positions of the ions have a zig-zag shape in the $x - y$ plane. For example, Fig. 56 shows the equilibrium positions for $\Delta\omega_{\text{tr}} = 2\pi \times 1\,\text{kHz}$ (blue) and $\Delta\omega_{\text{tr}} = 2\pi \times 299\,\text{kHz}$ (orange).

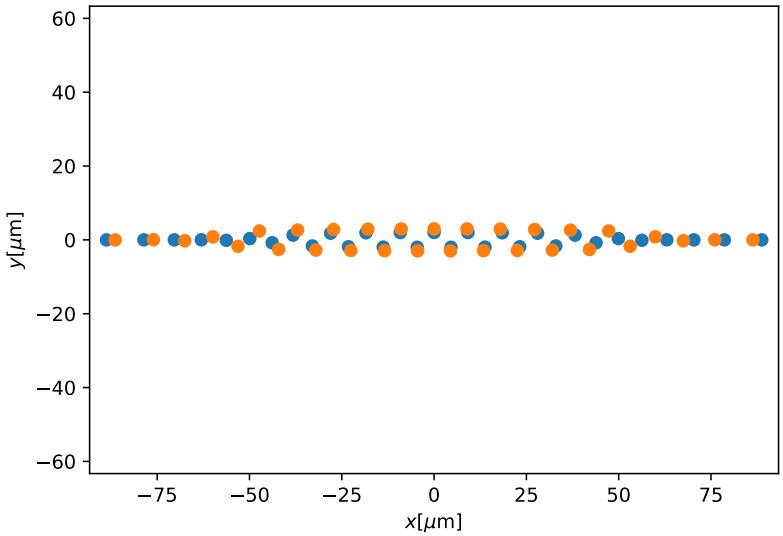

Figure 56: Equilibrium positions of ions (at the beginning of an rf cycle) for $\Delta\omega_{\text{tr}} = 2\pi \times 1\,\text{kHz}$ (blue) and $\Delta\omega_{\text{tr}} = 2\pi \times 299\,\text{kHz}$ (orange).

For a given $\Delta\omega_{\text{tr}}$, hence for a given set of trap parameters and equilibrium positions, one can simulate the probability for the zig-zag shape to flip after a collision with a H_2 molecule at temperature T. The velocity of H_2 follows a Maxwell-Boltzmann distribution and, the collision is in 1D along the incoming direction of the molecule. Numerically, it is found that after 2×10^4 rf periods, the ion chain will reach a local potential minimum (not necessarily the original one)

due to damping from the Doppler cooling beam. Then, the initial and the final configurations can be compared to see if the chain has flipped from a "zig" to a "zag" configuration. At low temperature such probability is very small and lots of samples are needed to measure it precisely. In order to count the number of flipping events, the initial and the final positions are sorted respectively according to their x coordinates, and then the squared distances between corresponding ions are added up. If the configuration has not flipped, the sum will be small (in this case $\lesssim 22\,\mu\mathrm{m}^2$); otherwise the sum will be much larger.

From the computational point of view, it must be noted that the trapped ion system is chaotic because of the nonlinear Coulomb interaction, thus any computational error will accumulate exponentially with the evolution time. To suppress the error, one may use very small step length and very high numerical precision, but the simulation will soon becomes computationally intractable. However, in the experiment there is always a Doppler cooling beam which scatters photons from the ions randomly. Therefore small errors in the simulation shall not change the qualitative behavior. The simulations use the Forest-Ruth method with 100 steps per rf period and *double* precision. p_{flip} was checked for convergence with steps increasing from 100 to 1000 per RF period.

First, the T dependence in the probability p_{flip} was studied by fixing $\Delta\omega_{\mathrm{tr}} = 2\pi \times 19\,\mathrm{kHz}$. The numerical results are shown in Fig. 57. As can be seen, for high temperature ($T \gtrsim 12\,\mathrm{K}$) the probability can be modelled as $p_{\mathrm{flip}} = 0.5\exp(-E/T)$; but at low temperature the probability is greater than the prediction. This suggests the existence of multiple paths and hence multiple energy barriers to flip the configuration.

Next, the $\Delta\omega_{\mathrm{tr}}$ dependence at $T = 4.7\,\mathrm{K}$ and $T = 7\,\mathrm{K}$ is shown in Fig. 58b. Because

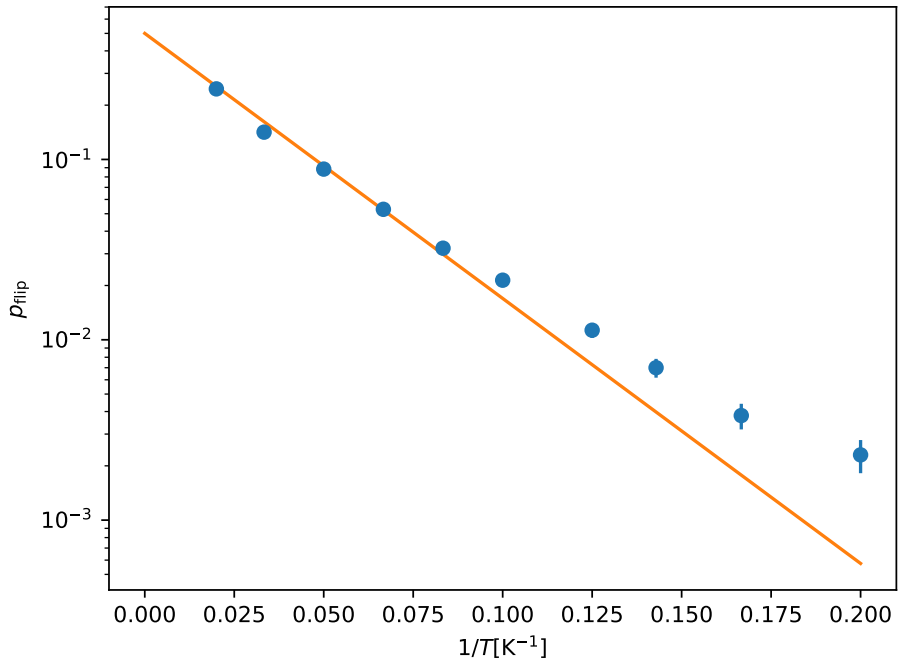

Figure 57: p_{flip} vs. T for $\Delta\omega_{\text{tr}} = 2\pi \times 19\,\text{kHz}$.

the probability p_{flip} is so low, 10^5 initial conditions were randomly sampled to estimate the probability, and this process was repeated 5 times to estimate the error bar. Note that p_{flip} does not decrease monotonically as $\Delta\omega_{\text{tr}}$ increases. This is because of the multiple modes inside the y-z plane, i.e. the previously mentioned multiple energy barriers. Also note that at large $\Delta\omega_{\text{tr}}$ it is possible to flip "half" the configuration: the ions will reach a local minimum of potential energy, but not necessarily the global minimum.

Fig. 58a shows the elastic rate measurements as a function of the barrier $\Delta\omega_{\text{tr}}$. As the barrier increases, there is a suppression in the reconfiguration rate but not of two orders of magnitude as predicted by the theory in Figure 58b. The discrepancy might be due to the difficulty in acquiring data for hours. Additionally, it is difficult to sample a low reconfiguration probability from collision induced flipping events when there is a possibility for flipping events

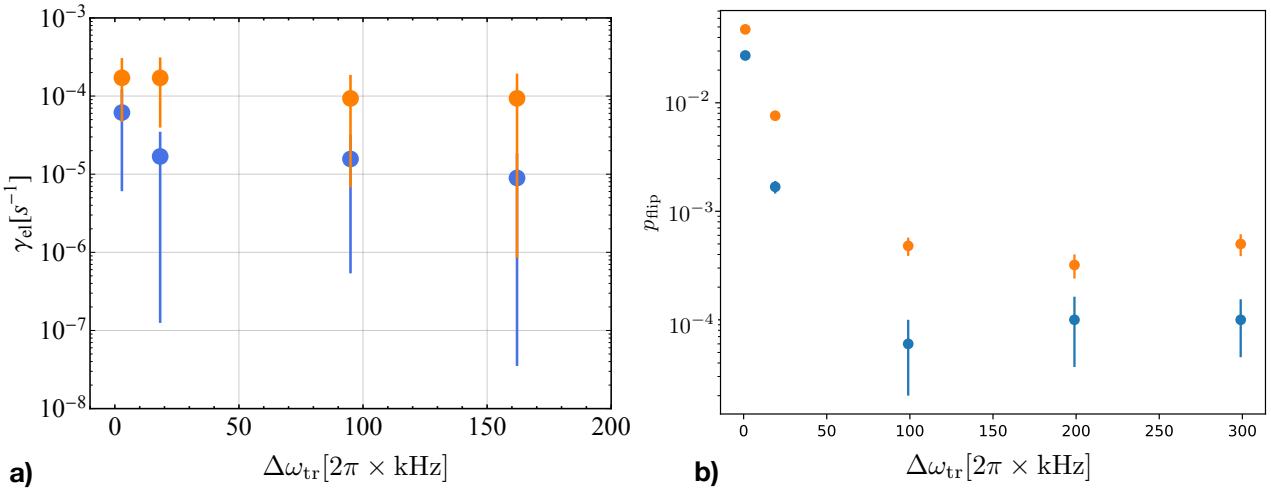

Figure 58: **a)** γ_{el} as a function of the barrier $\Delta\omega_{\rm tr} = \omega_z - \omega_y$. The blue (orange) points refer to $T = 4.5\,{\rm K}$ ($T = 7\,{\rm K}$), respectively. The data have been acquired with a number of ions varying from $N = 31$ to $N = 38$ for a time period varying up to 12 hours. The reported rate is per ion. **b)** Numerical results for $p_{\rm flip}$ vs. $\Delta\omega_{\rm tr}$ for $T = 4.7\,{\rm K}$ (blue) and $T = 7\,{\rm K}$ (orange).

that are not caused by collisions[46].

It was experimentally observed that the flipping rate increased with the number of dark ions, which are only sympathetically cooled by the bright ions. This leads to a higher chain temperature that can cause flipping events through thermal activation. Additionally, electric field noise (not included in the simulation) at frequencies of the order of the barrier could flip the zig zag chain. These two factors likely prevent one from resolving reconfiguration rates lower than 10^{-5} s^{-1}. For these reasons the measurement of $\gamma_{\rm el}$ at the lowest barrier value $\Delta\omega_{\rm tr}/(2\pi) = 2$ kHz is the most reliable estimate of the pressure.

[46]The other proposed mechanism for chain flipping is from noise in the trapping potential at the flipping barrier frequency, $\Delta\omega_{tr}$.

D Uniformly spaced ions

The segmented blade trap features 10 static electrodes which allow for the realization of axial anharmonic potentials. In particular, quartic axial potentials have been shown to offer several advantages in handling, cooling (57) and performing coherent operations (58) on large ion chains. Such potentials make it easier to avoid zig-zag sections forming at the center of the chain. At the same time, tailored anharmonicity in the axial potential allows one to minimize the ion spacing inhomogeneity induced by the Coulomb repulsion and enable control of the average spacing between the ions. In addition, a homogeneous spacing configuration prevents the ions in the center of the chain from becoming too close to each other. This reduces cross-talk in ion state detection and single ion manipulation with individual-ion addressing laser beams. Finally, the anharmonic potentials can be used to shape the normal mode structure (59; 60) and to minimize the inhomogeneity in the laser-induced spin-spin coupling (61) by shaping the transverse normal-mode structure.

The form of the quartic axial potential induced by the static electrodes can be written as:

$$V_{ax} = \sum_{i=1}^{N} \frac{\alpha_2}{2} x_i^2 + \frac{\alpha_4}{4} x_i^4, \tag{32}$$

where x_i is the position of the i-th ion and $\alpha_2 = m\omega_x^2$, with ω_x as the axial frequency and the ion atomic mass m. The axial equilibrium positions are determined by the balance between the electrostatic axial forces ($F_{ax} = -\partial_x V_{ax}$) and the inter-ion Coulomb repulsion:

$$0 = u_i + \beta u_i^3 - \sum_{j=1}^{i-1} (u_i - u_j)^{-2} + \sum_{j=i+1}^{N} (u_i - u_j)^{-2} \tag{33}$$

where $u_i = x_i/\ell$ is the i-th ion's position in adimensional units and $\ell = (q^2/4\pi\epsilon_0 m\omega_x^2)^{1/3}$ is the characteristic length of the axial potential. ϵ_0 is the vacuum permittivity and q is the electron charge. The quartic potential is characterized by the dimensionless ratio $\beta = \alpha_4\ell^2/\alpha_2$ (58),

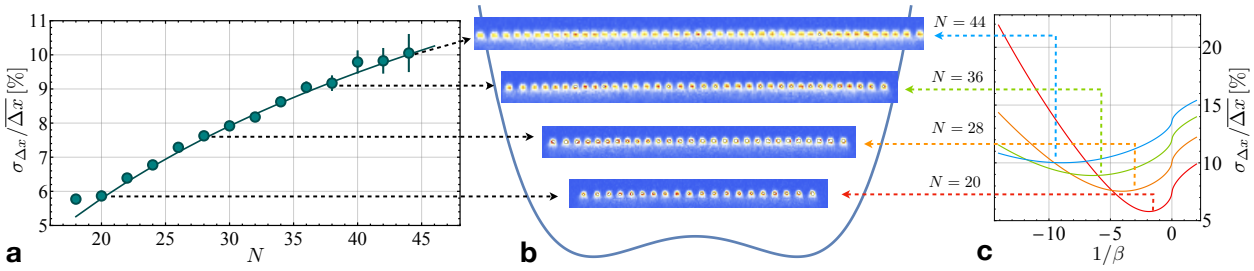

Figure 59: **Uniformly spaced ion chains**. a) The spacing variance to mean ratio $\Delta\sigma_x/\overline{\Delta x}$ as a function of the number of ions in the linear chain. Data points are taken in the optimized electrode configuration resulting in a minimal inhomogeneity, which corresponds to the theoretical prediction for a quartic potential. The spacing values have been chosen according to practical considerations concerning the available electrodes voltages and the camera area. b-c) Ion chain with optimized spacing inhomogeneity for $N = 20, 28, 36, 44$ ions. A not-to-scale plot of the quartic potential for N=44 is shown as a guide to the eye. The error bars have been calculated propagating the Gaussian fit errors on the ion centers. c) The spacing variance to mean ratio computed numerically for $N = 20, 28, 36, 44$ ions as a function of $1/\beta$, which characterizes the ratio between the quadratic and the quartic component.

which can be optimized to minimize the inhomogeneity of the ion chain. By solving equation (33), it is possible to find the optimal value $\beta^*(N)$ (see Fig. 59c) for a certain ion number N, that minimizes the ion inhomogeneity. β can be parameterized by the ratio $\sigma_{\Delta x}/\overline{\Delta x}$, where $\sigma_{\Delta x}$ and $\overline{\Delta x}$ are the ion spacing standard deviation and mean spacing, respectively. Once the optimal $\beta^*(N)$ is found, it is possible to fully determine the potential by choosing a desired average spacing $\overline{\Delta x}$, which depends on the absolute value of the harmonic frequency ω_x. A particular choice of the quadratic term α_2^* determines the characteristic length $\ell(\alpha_2^*)$ and corresponds to a certain equilibrium average spacing $\overline{\Delta x}^*$. Therefore, the quartic component is determined by the equation $\alpha_4 = \beta^*\alpha_2^*/\ell^2(\alpha_2^*)$. In Fig. 59a, it is shown how one can obtain

the minimum variance to mean spacing ratio (solid curves) by tuning the quartic potential, with N ranging from $N = 18$ to $N = 44$ ions in a linear configuration.

E Helical Resonator

A helical resonator (62) enables impedance matching between a radio-frequency source and the trap by acting as a step-up transformer. If the resonator were outside the vacuum, the parasitic capacitance and inductance of the 70 cm long coaxial rf transmission cable between the vacuum feedthrough and the ion trap would make the impedance matching between the tuned resonator and trap circuit (63) very difficult. This would limit the rf voltage that could be delivered to the trap without encountering resistive heating of the rf cables. Therefore, the apparatus is designed to hold the helical resonator in the 4 K region as close as possible to the blade trap.

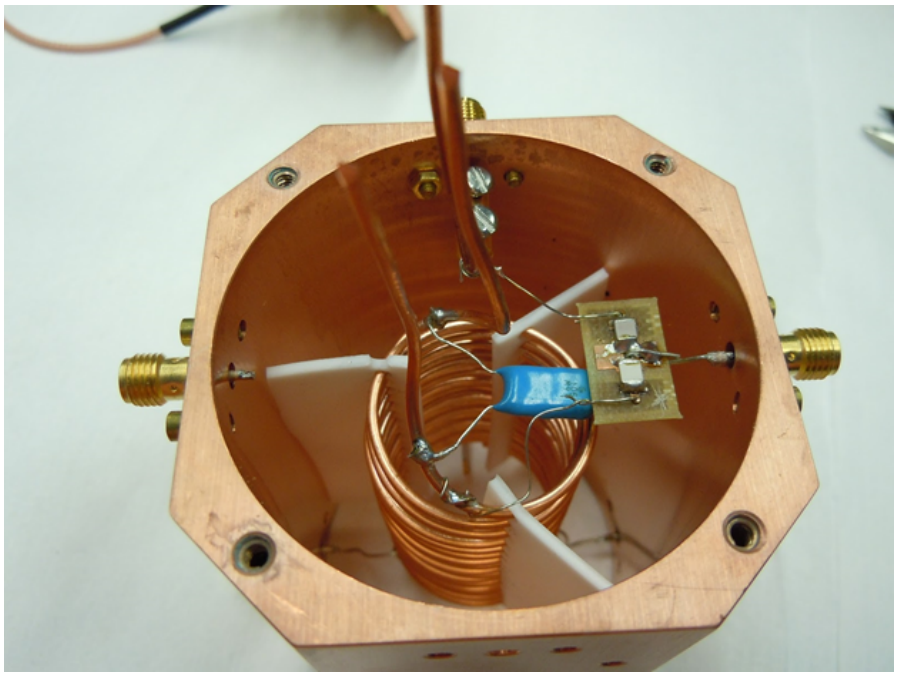

Figure 60: **Bifiler resonator**. Picture of the inside of the in-vacuum bifilar helical resonator. The end of the resonator pictured is closest to the trap. The blue capacitor connects the two coils so the applied RF on each coil is in phase with the other coil. The capacitors on the board create a capacitive divider so RF power can be picked off and used to stabilize the trap frequency. Each of the two coils can be individually biased using capacitors on the other side of the resonator (not visible here).

Inside the helical resonator (Fig. 60), there is a bifilar coil whose two components are each connected to one of the two rf blades. In this way, each blade can have an independent static potential offset. The two coils are held in place by teflon holders and they are shorted at rf with a 400 nF capacitor. The resonator is made of solid copper with a 2.3" inner radius, whereas the bifilar coil features a 1.5" radius and a 0.19" pitch. A capacitive 100:1 pick-off of the rf voltage was inserted inside the resonator to monitor and actively stabilize the transmitted voltage amplitude to the trap blades (64). The self-inductance $L_{\mathrm{res}} = 2\ \mu$H and self-capacitance $C_{\mathrm{res}} = 8$ pF have been measured with loading the resonator with different test-capacitors. In this case, the capacitor simulates the capacitance of an ion trap.

At room temperature the intrinsic ("unloaded") resonator quality factor is $Q = 1050$, where Q is defined as:

$$Q = \frac{2\,Q_{\mathrm{load}}}{1 - \sqrt{R}}, \tag{34}$$

where R is the reflected rf power due to impedance mismatch (see Fig. 61) and $Q_{\mathrm{load}} = \Omega_{\mathrm{rf}}/\mathrm{FWHM}$ is the loaded Q-factor, which also takes into account the impedance matching with the rf source. The resonator is inductively coupled with a small 0.5" diameter antenna-coil, whose position can be tuned to reach critical coupling. At 4 K, the resistance of the whole rf circuit is reduced and two effects take place: the Q value at critical coupling increases up to 3170 and the impedance matching condition changes (see Fig. 61). The 60% increase in the resonator quality factor is lower than what would be expected from a simple estimate based on the decrease of copper resistivity and skin depth at 4 K. This is likely explained by oxide layers on the copper surface or by the additional resistance contribution of solder connections in the resonator. In order to compensate the temperature induced resistance change, the

mutual inductance between the antenna and the bifilar coil is reduced by pulling out the antenna holder (see Fig. 8b) away from the optimal position at room temperature. During the cool-down, the drive frequency $\Omega_{\rm rf}/2\pi$ increases typically by 0.6%, which is explained by the reduction in resonator self-capacitance and self-inductance induced by thermal contraction of the copper.

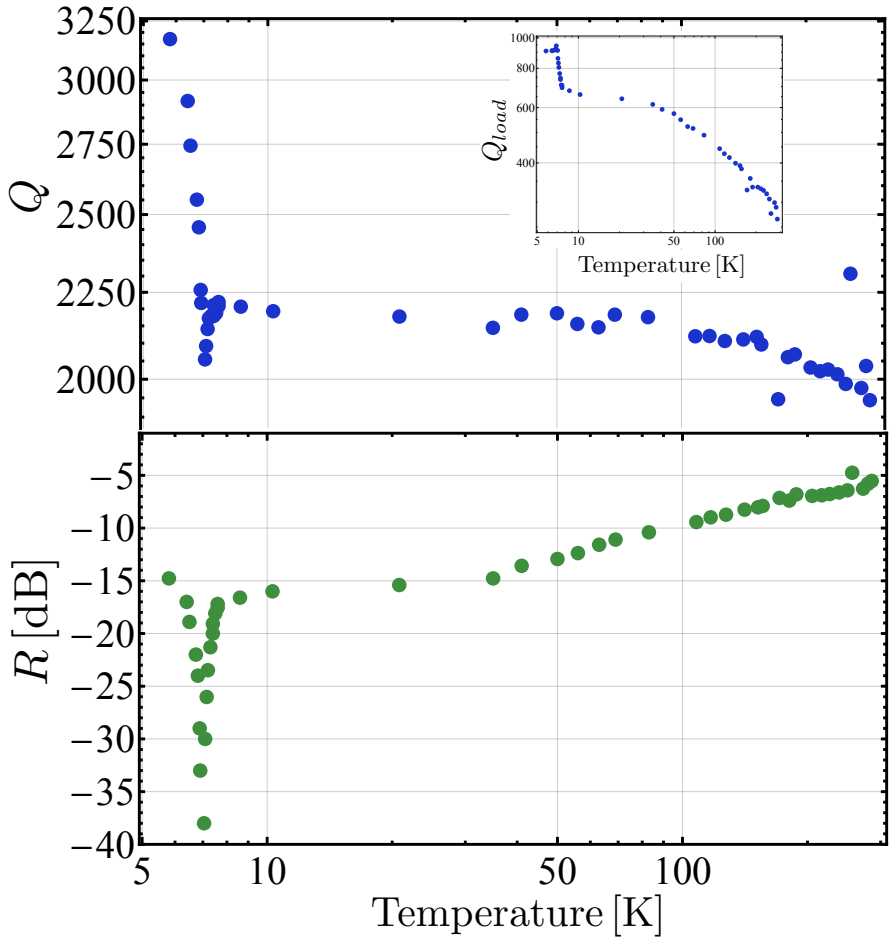

Figure 61: **Measurement of resonator Q-factor and rf reflected power as a function of the temperature.** The steep variation at low temperatures is due to the sharp decrease in the copper resistivity below 100 K (13), whose effect is delayed as the bifilar coil is in poor thermal contact with the copper can. The loaded quality factor $Q_{\rm load}$ (Inset, see text for details) increases from 210 up to 900 during the cool-down. All the measured Q values have an uncertainty of about 1%, given by the uncertainty on the vector analyzer reading.

Part VII

Bibliography

References

[1] Kiendl, T., Matquardt, F., *Many-Particle dephasing after a quench*, Phys. Rev. Lett. 118, 130601 (2017).

[2] Molmer, K., Sorensen, K., *Multiparticle entanglement of hot trapped ions*, Phys. Rev. Lett. 82, 1835-1838 (1999).

[3] Lee, A.C. *Engineering a Quantum Many-Body Hamiltonian with Trapped Ions*, PhD thesis, University of Maryland, College Park (2016).

[4] Lee, A.C. *Ytterbium Ion Qubit State Detection on an ICCD Camera*, Senior Honors thesis, University of Maryland, College Park (2012).

[5] Johnson, K.G. *Experiments with Trapped Ions and Ultrafast Laser Pulses*, PhD thesis, University of Maryland, College Park (2012).

[6] Pagano, G., et al. *Cryogenic trapped-ion system for large scale quantum simulation*, Quantum Science and Technology 4, 014004 (2019).

[7] Berkeland, D.J., et al. *Minimization of ion micromotion in a Paul trap*, Journal Of Applied Physics, (1998).

[8] James, D.F.V. *Quantum dynamics of cold trapped ions with application to quantum computation*, Applied Physics B, (1998).

[9] Sackett, C.A., et al. *Experimental entanglement of four particles*, Nature, (2000).

[10] Islam, K.R. *Quantum Simulation of Interacting Spin Models With Trapped Ions*, PhD thesis, University of Maryland, College Park (2012).

[11] Mizrahi, J.A. *Ultrafast Control of Spin and Motion in Trapped Ions*, PhD thesis, University of Maryland, College Park (2013).

[12] Senko, C.R. *Dynamics and Excited States of Quantum Many-Body Spin Chains with Trapped Ions*, PhD thesis, University of Maryland, College Park (2014).

[13] Ekin, J. *Experimental Techniques for Low-Temperature Measurements*, OUP Oxford, (2006).

[14] Lee, A., et al. *Engineering large Stark shifts for control of individule clock state qubits*, PRA, (2016).

[15] Berkeland, D.J., et al. *Minimization of ion micromotion in a Paul trap*, Journal of Applied Physics, (1998).

[16] Leibfried, D., et al. *Quantum dynamics of single trapped ions*, Reviews of Modern Physics, (2003).

[17] Wineland, D.J., et al. *Experimental Issues in Coherent Quantum-State Manipulation of Trapped Atomic Ions*, J. Res. Natl. Inst. Stand. Technol., (1998).

[18] Olmschenk, S., et al. *Manipulation and detection of a trapped Yb^+ hyperfine qubit*, Phys. Rev. A, (2007).

[19] Pagano, G., et al. *Quantum Approximate Optimization with a Trapped-Ion Quantum Simulator*, arXiv 1906.02700 (2019).

[20] Hankin, A.M., et al. *Systematic uncertainty due to background-gas collisions in trapped-ion optical clocks*, arXiv 1902.08701v2 (2019).

[21] This experiment is completed, but it is still being written.

[22] Steck Quantum Optics Notes

[23] Mehta, K.K., et al. *Integrated optical addressing of an ion qubit*, Nature Nanotechnology, (2016).

[24] Lee, A.C., et al. *Engineering large Stark shifts for control of individual clock state qubits*, Phys. Rev. A, (2016).

[25] Pagano, G., Beck, K.M., Foss-Feig, M., Grass, T. *New Directions in Many-body Physics and Quantum Computing enabled by EIT coolinfg*, Seed Funding Report, (2019).

[26] Semerikov, I.A., et al. *EIT Ground State Cooling Scheme of $^{171}Yb^+$ Based on the $^2S_{1/2} \rightarrow {}^2P_{1/2}$ Cooling Transition*, Journal of Russian Laser Research, (2018).

[27] Preskill, J. *Quantum Computing in the NISQ era and beyond*, Quantum 2, 79 (2018).

[28] Paul, W. *Electromagnetic traps for charged and neutral particles*, Rev. Mod. Phys., (1990).

[29] Monroe, C., et al. *Quantum Logic with a Few Trapped Ions*, American Institute of Physics, (1999).

[30] Turchette, Q.A., et al. *Deterministic Entanglement of Two Trapped Ions*, Phys. Rev. Lett., (1998).

[31] Bell, A.S., et al. *Laser cooling of trapped ytterbium ions using a four-level optical-excitation scheme*, Phys. Rev. A, (1991).

[32] Molmer, K., Sorensen, A. *Multiparticle entanglement of hot trapped ions*, Phys. Rev. Lett., (1999).

[33] Day, C. *Basics and Application of Cryopumps*, (2006).

[34] Dehment, H.G. *Radiofrequency spectroscopy of stored ions I: Storage*, Adv. At. Mol. Phys., (1967).

[35] Jurcevic, P., et al. *Direct Observation of Dynamical Quantum Phase Transitions in an Interacting Many-Body System*, Phys. Rev. Lett., (2017).

[36] Stick, D., et al. *Ion trap in a semiconductor chip*, Nature Physics, (2006).

[37] Botcherby, E.J., et al. *An optical technique for remote focusing in microscopy*, Optics Communications, (2007).

[38] Botcherby, E.J., et al. *Aberration-free optical refocusing in high numerical aperture microscopy*, Optics Letters, (2007).

[39] Fisk, P.T.H. *Trapped-ion and trapped-atom microwave frequency standards*, Rep. Prog. Phys., (1997).

[40] Islam, R. *Beat not stabilization of mode-locked lasers for quantum information processing*, Optical Letters, (2014).

[41] Berkeland, D.J., Boshier, M.G. *Destabilization of dark states and optical spectroscopy in Zeeman-degenerate atomic systems*, Phys. Rev. A, (2002).

[42] Sugiyama, K., Yoda, J. *Production of YbH^+ in excited states with H_2 gas*, Phys. Rev. A, (1997).

[43] Kim, K., et al. *Entanglement and Tunable Spin-Spin Couplings between Trapped Ions Using Multiple Transverse Modes*, Phys. Rev. Lett., (2009).

[44] Gabrielse, G., et al. *Precision Mass Spectroscopy of the Antiproton and Proton Using Simultaneously Trapped Particles*, Phys. Rev. Lett., (1999).

[45] Inlek, I.V., et al. *Quantum gates with phase stability over space and time*, Phys. Rev. A, (2014).

[46] Zipkes, C., et al. *Kinetics of a single trapped ion in an ultracold buffer gas*, New Journal of Physics, (2011).

[47] Cetina, M., Grier, A.T., Vuletic, V. *Micromotion-Induced Limit to Atom-Ion Sympathetic Cooling in Paul Traps*, Phys. Rev. Lett., (2012).

[48] Chen, K., Sullivan, S.T., Hudson, E.R. *Neutral Gas Sympathetic Cooling of an Ion in a Paul Trap*, Phys. Rev. Lett., (2014).

[49] Ryjkov, V.L., Zhao, X.Z., Schuessler, H.A. *Simulations of the rf heating rates in a linear quadrupole ion trap*, Phys. Rev. A, (2005).

[50] Alheit, R., et al. *Higher order non-linear resonances in a Paul trap*, International Journal of Mass Spectrometry and Ion Processes, (1996).

[51] Drakoudis, A., Sollner, M., Werth, G. *Instabilities of ion motion in a linear Paul trap*, International Journal of Mass Spectrometry, (2006).

[52] Zhang, J., et al. *Observation of a many-body dynamical phase transition with a 53-qubit quantum simulator*, Nature, (2017).

[53] Langevin, M. *Une formule fondamentale de theorie cinetique*, Annales de chimie et de physique, (1905).

[54] Jachymski, K., et al. *Quantum Theory of Reactive Collisions for* $1/r^n$ *Potentials*, Phys. Rev. Lett., (2013).

[55] Lehmitz, H., et al. *Population trapping in excited Yb ions*, Phys. Rev. Lett., (1989).

[56] Fishman, S., et al. *Structural phase transitions in low-dimensional ion crystals*, Phys. Rev. B, (2008).

[57] Lin, G.-D., Duan, L.-M. *Sympathetic cooling in a large ion crystal*, Quantum Information Processing, (2015).

[58] Lin, G.-D., et al. *Large-scale quantum computation in an anharmonic linear ion trap*, Europhysics Letters, (2009).

[59] Home, J.P., et al. *Normal modes of trapped ions in the presence of anharmonic trap potentials*, New Journal of Physics, (2011).

[60] Johanning, M. *Isospaced linear ion strings*, App. Phys. B, (2016).

[61] Porras, C., Cirac, J.I. *Effective Quantum Spin Systems with Trapped Ions*, Phys. Rev. Lett., (2004).

[62] Macalpine, W.W., Schildnecht, R.O. *Coaxial Resonators with Helical Inner Conductor*, Proceedings of the IRE, (1959).

[63] Siverns, J.D., et al. *On the application of radio frequency voltages to ion traps via helical resonators*, App. Phys. B., (2012).

[64] Johnson, K.G., et al. *Active stabilization of ion trap radiofrequency potentials*, Review of Scientific Instruments, (2016).

[65] Sakurai, J.J., Napolitano, J. *Modern Quantum Mechanics*, Second edition, Addison-Wesley, (2011).

[66] Franzen, A. *ComponentLibrary*, http://www.gwoptics.org/ComponentLibrary/, (2019).

[67] Koffel, T., et al. *Entanglement Entropy for the Long-Range Ising Chain in a Transverse Field*, Phys. Rev. Lett. 109, 267203 (2012).

[68] Sheskin, D.J. *Handbook of Parametric and Nonparametric Statistical Procedures*, Fourth Edition, IBSN:1584888148.

[69] This is a paper on many-body dephasing that I am working on with a team of theorists. I am leaving the full theoretical explanation to the paper.

[70] Rigol, M., Dunjko, V., Olshanii, M. *Thermalization and its mechanism for generic isolated quantum systems*, Nature (2008).

[71] Deutsch, J.M. *Quantum statistical mechanics in a closed system*, Phys. Rev. A (1991).

[72] Srednicki, M. *Chaos and quantum thermalization*, Phys. Rev. E (1994).

[73] Kim, K., et al. *Quantum simulation of frustrated Ising spins with trapped ions*, Nature (2010).